Ultra-Refractive Photonic Crystals,
Colloidal Opals,
and
Photonic Band Gaps in the THz-Range

Anton W. Öttl
Fakultät für Physik
Albert-Ludwigs-Universität, Freiburg

March 2. 2001

I would like
to dedicate this work
to

THE BEATLES

Contents

Photonische Kristalle stellen zur Zeit ein vielbeachtetes und lebendiges Forschungsgebiet in der Physik und ganz allgemein in den Naturwissenschaften dar. Dieses interdisziplinäre Forschungfeld wurde 1987 aus Ideen von Sajeev John [Joh87] und Eli Yablonovitch [Yab87], über Lokalisierung von Licht und gehemmte spontane Emission geboren. Grob gesagt entwickelten sie ein Konzept um die räumliche und zeitliche Ausbreitung von elektromagnetischen Feldern bewußt zu kontrollieren. Seit dieser Zeit wird den physikalischen Grundlagen der photonischen Kristalle, in Theorie und Experiment viel Aufmerksamkeit gewidmet. Diese Aufmerksamkeit beschränkt sich aber nicht nur auf die Physik sondern erstreckt sich über die Chemie und Biologie bis zu technologischen Anwendungen und sogar Kunst. Auf eine bestimmte Art und Weise revolutionierten photonische Kristalle sogar das Verständnis der Optik in der Physik.

Einen schönen Überblick über das Gebiet der photonischen Kristalle bietet das Buch von Joannopoulos [JMW95].

Prinzip Das Grundprinzip der photonischen Kristalle ist relativ einfach und intuitiv. Ein photonischer Kristall ist eine räumliche Struktur mit periodisch moduliertem Brechungsindex. Diese Periodizität muß in der Größenordnung der zu beeinflussenden Wellenlänge sein. In einer Dimension sind solche Strukturen altbekannt. Es handelt sich um dielektrische Spiegel, welche aus abwechselnden Schichten von unterschiedlichem Brechungsindex, mit einer Schichtdicke von einer Viertel Wellenlänge bestehen. Bei geeigneter Wahl der Brechungsindizes besitzen sie perfekte Reflexionseigenschaften bei dieser bestimmten Wellenlänge. Klassisch gesehen kann diese Eigenschaft der konstruktiven (in Reflexion) und destruktiven (in Transmission) Interferenz durch aufeinanderfolgende Schichten zugeschrieben werden. Im Bild der photonischen Kristalle ergibt sich für diesen Fall eine Bandlücke, welche die Lichtausbreitung in dieser Richtung verbietet. Ursache dafür ist die Periodizität im Brechungsindex, die in Analogie als periodisches quantenmechanisches Potential angesehen werden kann. Diese grundlegende Idee kann natürlich auf den 2- und 3-dimensionalen Raum ausgedehnt werden (siehe Grafik). Im 3-dimensionalen Fall spricht man von einer vollständigen photonischen Bandlücke, wenn die Lichtausbreitung in allen Raumrichtungen verboten ist.

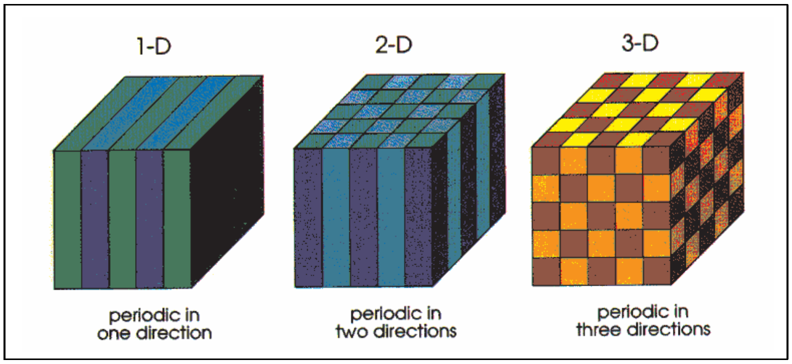

Figure 1: *Prinzip der photonischen Kristalle: periodische Strukturen in einer, zwei und drei Raumdimensionen [JMW95]*

Anwendungen Das zunehmende Interesse an photonischen Kristallen ist hauptsächlich der Güte und Vielfalt ihrer Anwendungen zuzuschreiben. Diese liegen besonders im florierenden Bereich optischer Telekommunikation und moderner Quantenoptik. Materialien mit photonischer Bandlücke bieten vollkommen neue, vielversprechende und überlegene Technologien im Vergleich zu herkömmlicher Optik. Zum Beispiel können photonische Kristalle als hochreflektierende Substrate in Antennensystemen Verluste reduzieren. Darüberhinaus könnten die perfekten Rexlexionseigenschaften in Verbindung mit deutlich erhöhter elektromagnetischer Modendichte dazu verwendet werden Laser mit geringem Schwellwert zu bauen. Neben der Anwendung als Filter oder Ummantelungsmaterialien, ist vor allem der Einsatz photonischer Kristalle zur Lichtleitung und Lichtumleitung in Strukturen mit räumlichen Dimensionen der Wellenlänge sehr interessant. Ein Ziel ist es integrierte photonische Schaltungen für zukünftige optische Computer zu bauen. Der Einbau künstlicher Defekte erlaubt es sogar Licht um sehr scharfe Ecken zu leiten [LCH$^+$98], ganz im Gegensatz zu konventionellen optischen Fasern, die auf dem Prinzip der Totalreflexion basieren. Dies eröffnet die Möglichkeit der Miniaturisierung zu optischen Schaltkreisen. Die Erwartungen auf diesen photonischen Schaltkreisen beruhen vor allem darauf in naher Zukunft elektronische Schaltkreise zu ersetzen. Vorteile sind das Fehlen der störenden Wärmeentwicklung und der Geschwindigkeitszuwachs aufgrund der kürzeren erzielbaren Pulslängen und größerer Bandbreite. Ähnliche Technologie ist bereits Bestandteil der optischen Nachrichtentechnik. Jüngste Ergebnisse zu einstellbaren photonischen Bandlücken könnten zur Realisierung von photonischen Transistoren führen [JB99]. Ein weiteres, lange ersehntes Ziel, die Erzeugung einer vollständigen 3-dimensionalen Bandlücke bei der für die optische Telekommunikation maßgeblichen Wellenlänge von 1.5 μm wurde kürzlich erreicht [BCG$^+$00].

Ebenso wurde durch die Entwicklung der photonischen Kristalle das Forschungsgebiet der Quantenoptik vorangetrieben. Hier sind hauptsächlich Defekte, welche Mikroresonatoren bilden und dadurch die elektromagnetische Modendichte verändern (von null in einer vollständigen Bandlücke, bis zu sehr großen Werten an den Rändern der Bandlücke) von vorrangigem Interesse. Außergewöhnliche Phänomene treten auf wenn Photonen auf einen Raum von der Grösse der Wellenlänge eingegrenzt werden. Bekannte quantenoptische Effekte, wie Photon-Atom-Wechselwirkungen in Hohlräumen, gehemmte spontane Emission und gebundene Photonen Zustände können mit Hilfe dieser Mikroresonatoren untersucht werden.

Herstellung Eine Vielfalt von photonischen Kristallen für die verschiedensten Wellenlängenbereiche kann bereits hergestellt werden. Die Fabrikation von photonischen Kristallen begann mit dem mechanischen Bohren von wohlgeordneten Löchern in Materialien für Experimente im Mikrowellenbereich. Ein berühmtes und typisches Beispiel hierfür stellt der Yablonovite-Kristall dar, der eine vollständige, 3-dimensionale Bandlücke aufwies. Diese Struktur wurde von E. Yablonovitch hergestellt [YGL91]. Die Strukturen mußten aber bedeutend kleiner gemacht werden, um infrarote und sichtbare Wellenlängen zu beeinflussen. Hochentwickelte Ätztechniken stellen heutzutage die besten Methoden zur Herstellung 2-dimensionaler Strukturen dar. Hingegen wurden die früher üblichen Lithographie-Methoden zu Herstellung von 3-dimensionalen sub-

Mikrometer Kristallen schon bald durch Selbstorganisationsmethoden, wie chemisch gewachsene kolloidale Kristalle [XGYL00] überholt. Außerdem versprechen holographische Methoden in der Lage zu sein, 2- und 3-dimensionale photonische Kristalle herzustellen [CSH$^+$00]. Grössere Strukturen wie sie zum Beispiel für den THz Frequenzbereich benötigt werden können sehr elegant mit sogenannten "Rapid-Prototyping" Techniken, wie "Laser assisted Chemical Vapor Deposition LCVD" [LS95] hergestellt werden.

Mutter Natur hat (natürlich) schon lange photonische Kristalle in Form von bunten Opalen, den schillernden Stacheln der 'sea-mouse' [PMM$^+$01], einem Meereswurm, und den farbigen Mustern auf Schmetterlingsflügeln [Gra98] entwickelt.

Überblick Der Begriff 'Kristall' stammt aus dem Bereich der Festkörperphysik und entspricht einer 3-dimensional periodischen Struktur. Zusätzlich bestehen weitgreifende Analogien zwischen dem Gebiet der Festkörperphysik und dem Gebiet der photonischen Kristalle. Deshalb leitet sich die Terminologie und viele theoretische Konzepte für photonische Kristalle aus der Festkörperphysik ab. Die Einführung dieser Begriffe und Strategien ist das Thema von Kapitel I dieser Arbeit sein. Außerdem wird in diesem Kapitel die zweite wichtige Grundlage photonischer Kristalle, die Elektrodynamik kurz zusammengefaßt. Kapitel II kombiniert diese zwei Aspekte und präsentiert theoretische Modelle, die das Verhalten von Photonen in diesen Kristallen beschreiben. Die Auswertung dieser Modelle wird mit Hilfe von Computerprogrammen, welche ebenfalls in diesem Kapitel beschrieben sind, numerisch ausgeführt. Danach werde ich repräsentative Ergebnisse dieser Methoden in Kapitel III zeigen und typische Merkmale photonischer Kristalle diskutieren. Dieses Kapitel beabsichtigt außerdem ein bestimmtes Verständnis und Gefühl für die Effekte in photonischen Kristallen zu vermitteln. In Kapiteln IV, V und VI, werden die Forschungen, die ich im Verlauf des vergangenen Jahres ausgeführt habe, gezeigt und diskutiert.

Der Ausgangspunkt für meine Forschungsaktivität auf dem Gebiet der photonischen Kristalle war ein 'Government of Canada Award', der mir im Jahr 2000 gewährt wurde. Ich bin Prof. Hanspeter Helm (Universität Freiburg) und Prof. Sajeev John (University of Toronto) sehr dankbar, daß sie es mir ermöglichten einen wesentlichen Teil dieser Diplomarbeit in Kanada, an der Universität von Toronto auszuführen. Von Januar bis Juni 2000 war ich an einem Projekt beschäftigt, das die kürzlich berichteten Ultrabrechungseigenschaften in photonischen Kristallen [KKT$^+$98] theoretisch analysierte. Ich habe sehr von der Unterstützung durch Ovidiu Toader profitiert, dessen Computerprogram ich verwenden konnte. Der Ablauf und die Ergebnisse dieser Forschungen werden in Kapitel IV berichtet und diskutiert. Seit meiner Rückkehr nach Freiburg konnte ich meine Kenntnisse auf dem Gebiet der photonischen Kristalle verfeinern und ausdehnen. In Kapitel V werde ich numerische Simulationen optischer Eigenschaften von kolloidalen Kristallen, wie sie von Matthias Soddemann in der Gruppe von Prof. Richtering, Kiel (ehemals Freiburg) hergestellt werden, präsentieren. Schließlich werde ich über experimentelle Ergebnisse von photonischen Kristallen im THz Frequenz Bereich berichten. Diese Experimente wurden im Rahmen der THz Pojekt Gruppe um Peter Uhd Jepsen in der Abteilung von Prof. Helm in Freiburg ausgeführt.

Ich bin begeistert Teil eines so faszinierenden und lebhaften Gebietes der Physik mit großem Anwendungspotential zu sein. Ich hoffe mit dieser Arbeit eine verständliche Einführung zum Themenkreis, und mit den konkreten Problemen die ich in dieser Arbeit behandle einen Beitrag zu den Forschungen auf dem Gebiet der photonische Kristalle leisten zu können

Photonic crystals are currently a very hot and vivid topic in physics and science in general. This interdisciplinary research field was born by ideas of Sajeev John [Joh87] and Eli Yablonovitch [Yab87] in 1987 about localization of light and inhibited spontaneous emission, respectively. Commonly speaking they discovered a way how to control light. Ever since then photonic crystals attract much interest throughout fundamental theoretical and experimental physics (optics, quantum optics), chemistry, biology as well as applied technology and arts. In a certain way they revolutionized the physic perception of optics.

A good overview of the field of photonic crystals is given in the book by Joannopoulos [JMW95].

Principle The basic principle of the photonic crystals is rather simple and intuitive. It solely requires a structure with periodically modulated refractive index. This periodicity however has to be on a length scale comparable to the wavelength in order for photonic crystal effects to appear. In one dimension such structures are well known. Dielectric mirrors, for instance consist of alternating layers of different dielectrics with a thickness of one quarter wavelength. They exhibit perfect reflection properties at this particular wavelength. Classically this property can be attributed to constructive (in reflection) and destructive (in transmission) interference from scattering by consecutive layers. In the photonic crystal picture a band gap, prohibiting the transmission of light, is formed by the periodicity in the refractive index which can be interpreted in analogy to a periodic quantum-mechanical potential. This fundamental idea can further be extended to 2- and 3-dimensional space. The latter case would inhibit light propagation in all spatial directions, thus creating a complete photonic band gap.

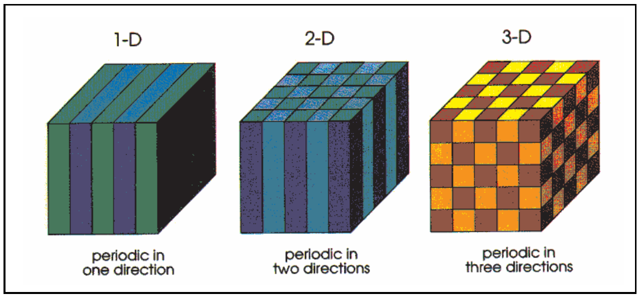

Figure 2: *Basic principle of photonic crystals: periodic structures in one, two and three dimensions [JMW95]*

Applications The excelling interest in photonic crystals mainly lies in their outstanding variety and quality of applications, especially in the booming area of optical telecommunications and modern quantum optics. Photonic band gap materials offer completely new, promising and superior techniques over conventional optics. They can be used, for instance as a high reflective ground of transmitters aiming the radiation towards the receiver, thereby avoiding losses. Their perfect reflection properties, along with increased electromagnetic mode density, can be incorporated to build lasers with near zero threshold. Besides the application as filters or cladding materials, their utility in guiding light in feature sizes on the order of the wavelength is highly interesting. A future goal is creating all photonic circuits, aimed towards optical computing. Artificial defects like lines can guide light even through very sharp turns [LCH$^+$98] in contrast to conventional optical fibers which are based on total internal reflection. This will eventually allow the miniaturization of optical chips. A prospect of such photonic chips is to take over the legacy of electronic chips but without any bothering thermal effects. Furthermore this would result in a gain of speed due to shorter pulse lengths achievable and increased band width. Similar technology is already in use in optical telecommunications. An initiator of modern information technology.

Recent results in tunable photonic band gaps [JB99] could lead towards photonic transistors, the 'holy grail' in photonics. Another long seeked goal, creating a full 3-dimensional band gap at the optical telecommunication wavelength of 1.5 μm, has just recently been achieved [BCG$^+$00].

By the same token photonic crystals boosted the research area of quantum optics. Here mainly defects, forming micro-cavities and distorting the photonic density of states, ranging from zero DOS in a complete photonic band gap to very large values at the band edges, are of interest. Unusual phenomena of photons confined to a volume comparable to their wavelength can be examined. This includes photon-atom interactions in cavities, like inhibited spontaneous emission, bound states or dressed atoms.

Fabrication A variety of photonic crystals for a diverse range of wavelengths can already be fabricated. The fabrication of photonic crystals started by mechanically drilling ordered holes in bulk materials for experiments in the microwave regime. A typical, famous example is the yablonovite crystal, which exhibited a complete 3-dimensional band gap, as manufactured by E. Yablonovitch [YGL91]. The structures however needed to be significantly smaller to reach infrared and visible wavelengths, so new fabrication techniques emerged. For 2-dimensional structures, different sophisticated etching techniques comprise the methods of choice nowadays. Whereas for the fabrication of sub-micron 3-dimensional crystals early layer-by-layer and micro-lithography methods were soon overtaken by self-organization techniques, like chemically grown colloidal crystals [XGYL00]. Furthermore holographic methods are also promising to fabricate both 2- and 3-dimensional photonic crystals [CSH$^+$00].

Mother nature has (of course) already invented photonic crystals, for example in the form of the colorful opals, the iridescent spines of the sea mouse [PMM$^+$01], a marine worm, and the colorful design on butterfly wings [Gra98]

Outline 'Crystals' are known as 3-dimensional periodic structure from solid state physics. Additional analogies link this area to the field photonic crystals. Therefore the terminology and the theoretical concepts are mostly taken over from solid state physics. Introducing these terms and strategies will be the topic of chapter I in this thesis. Also included in this chapter is a recapitulation of basic electrodynamics, the other theoretical basis of photonic crystal. Chapter II combines these two branches and presents theoretical techniques describing the behavior of photons in these crystals. The evaluation is performed numerically with computer programs which are also explained in this chapter. Subsequently I will show representative results of these methods and discuss typical features of photonic crystals in chapter III. This chapter is intended to develop a certain understanding and feeling for the effects of photonic crystals. In chapters IV, V and VI the research I conducted over the past year will be presented and discussed.

The starting point for my research activity in photonic crystals was given by a Government of Canada Award which I was granted for the year 2000. I am very grateful to Prof. Hanspeter Helm from the University of Freiburg and Prof. Sajeev John from the University of Toronto that I was allowed to carry out research work in Prof. John's group as part of this thesis. From January to June 2000 I was involved in a project theoretically investigating recently reported ultra-refractive effects [KKT$^+$98] in photonic crystals. I benefited from the support of Ovidiu Toader who developed a numerical computer program which I could employ. The progress and outcomes of this research are reported and discussed in chapter IV. Upon being back in Prof. Helm's group I could refine and extend my experience on photonic crystals. In chapter V numerical simulations for optical properties of colloidal crystals, as being prepared by Matthias Soddemann in the group of Prof. Richtering, Kiel (formerly Freiburg) are presented. Eventually I will report experimental findings for photonic crystals in the THz frequency regime. These experiments were carried out in the 'Thz project group' around Peter Uhd Jepsen in the research group of Prof. Helm in Freiburg.

Overall it is very exciting to be part of such a fascinating and vivid field with great potential applications. I hope to contribute with this thesis to the promotion of the research on photonic crystals. Furthermore I hope to provide a coherent introduction for readers new to this field.

Chapter 1

Theoretical Framework

This chapter will serve as a quick review on the classical fields of solid state physics and electrodynamics. The methods and definitions herein are fundamental to develop the concepts of photonic crystals and their optical properties.

1.1 Solid State Physics Fundamentals

One of the cornerstones in the theoretical treatment of photonic crystals is to be familiar with the basics in solid state physics. Therefore, we have to reproduce them first and start with introducing periodical geometrical arrangements in 2- and 3-dimensional space, crystal structures, reciprocal space and some basic theoretical methods, like the tight-binding model and the nearly-free electron approach, as well as common representation schemes of a band structure diagram and the density of states.

The treatment of the geometrical aspect of photonic crystals, i.e. the crystal structures is re-applicable from well established condensed matter physics on a different length scale. Furthermore there exists a fundamental analogy between photonic crystals and conventional crystals: waves in periodic potentials. The arrangement of the atomic potentials in a regular crystal affects the wave functions of electrons and causes the electronic bands to form. In the photonic case, on the other hand the scatterers with a different index of refraction take up the role of the atomic potentials for the photons. Combined with the periodicity they are the cause for the formation of photonic bands. As a consequence it is possible to treat the photonic and electronic case with similar approaches and (re-)use most of the ideas and methods of solid state physics.

An educational introduction, also covering advanced topics in solid state physics is given in the classical textbooks of Ashcroft and Mermin [AM76] and Kittel [Kit99]. Most of the figures in this chapter are taken from [AM76], except as noted otherwise.

1.1.1 Crystal Structures

The main characteristic of a crystal is of course its periodicity. A certain element or cell is repeated in all directions of space. In the simplest case this is a point, resulting in a *point lattice.* There are many different configuration of periodicities with respect to the axis spanning the space. In order to characterize those structures, each point lattice is described by a set of vectors ($[\boldsymbol{a_1}, \boldsymbol{a_2}, \boldsymbol{a_3}]$ for instance), which are usually the non reducible *primitive vectors.*

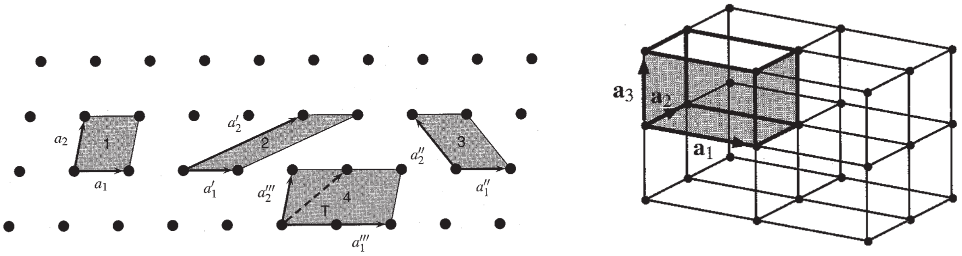

Figure 1.1: *point lattices, primitive vectors and primitive unit cells in 2- and 3-dimensional space [Kit99]*

They span a *primitive unit cell* with a volume $V = (\boldsymbol{a_1} \times \boldsymbol{a_2}) \cdot \boldsymbol{a_3}$. The primitive vectors provide the coordinate system, i.e. a grid in space which determines the periodicity by translations of the cell by multiples of $\boldsymbol{a}$. So each point of the lattice can be reached by a linear combination of these primitive vectors.

$$\boldsymbol{R} = n_1\boldsymbol{a_1} + n_2\boldsymbol{a_2} + n_3\boldsymbol{a_3} \tag{1.1}$$

If the cell contains more than one point or atom per cell, then more information, e.g. a second set of vectors, is required to describe the internal structure, which is called *basis* or *motif* (see Fig. 1.2). The basis and the point lattice make up the complete crystal structure.

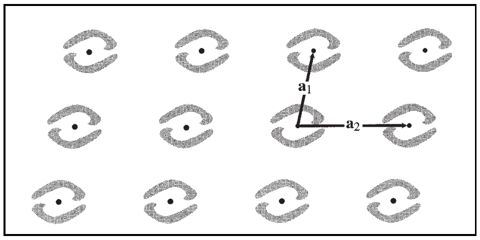

Figure 1.2: *A point lattice and a motif form a crystal [Kit99]*

The possible point lattice types can be classified according to lengths and angles of their primitive vectors. August Bravais showed in 1850 that there are only 14 possible configurations of point lattices in three dimensions and only 5 in two dimensions. These configurations are often referred to as *Bravais lattices.* For reasons of completeness and future references they are all listed here (see Fig. 1.3 and Fig. 1.4).

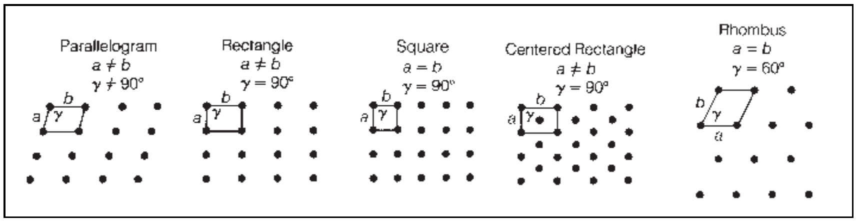

Figure 1.3: *The 5 2-dimensional Bravais lattice types . . .*

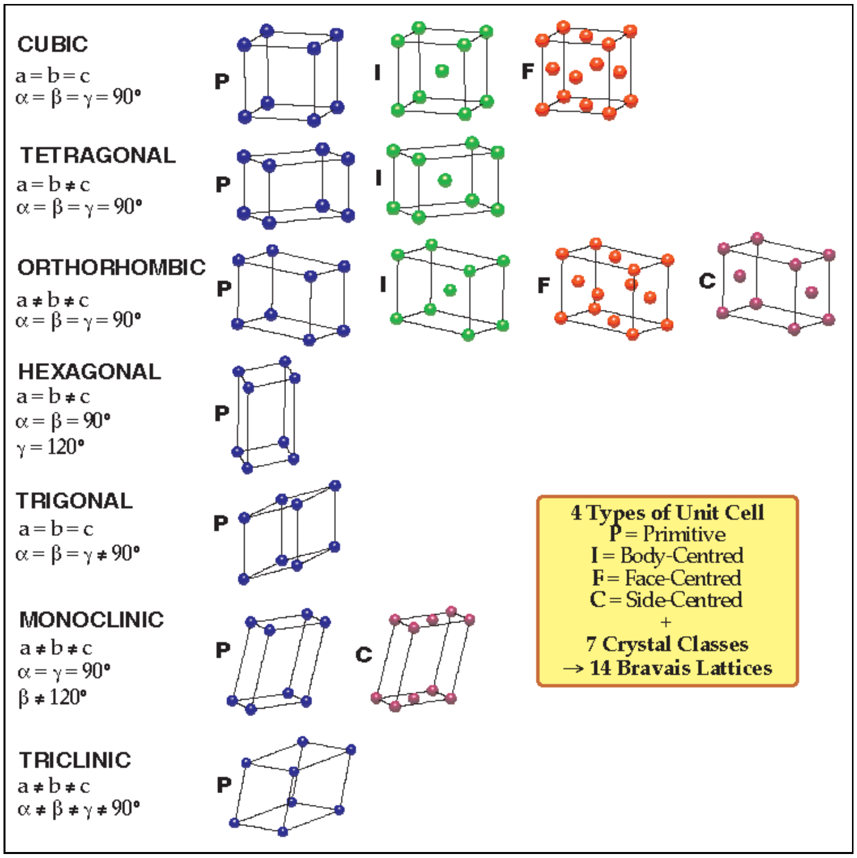

Figure 1.4: *. . . and the 14 3-dimensional Bravais lattice types*

A set of primitive vectors also allows the definition of lattice planes in the crystal, identified by the so-called *Miller indices.* This set of integers (triplett in 3 dimensions, dublet in 2 dimensions, e. g. {1,0,1}, {1,3}) refers to the multiples of primitive vectors required to express the normal on the lattice planes as a linear combination of them. The orientation of the planes becomes important in scattering experiments when waves are reflected at consecutive layers of lattice planes and interfere with each other. The conditions for that were elaborated by and named after *von Laue* and *Bragg.* A neat manifestation of lattice planes in everyday-live are the flights visible when driving by a field of regularly planted sunflowers for instance.

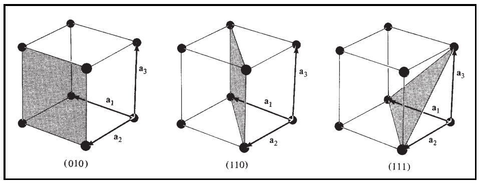

Figure 1.5: *Lattice planes and their corresponding Miller indices*

A different approach to classify the lattices is according to their *symmetry properties*. This crystallographic classification follows rules from mathematical group theory and uses various nomenclature systems. Generally the symmetry properties of the point lattice are stated in many (32) *point groups*. The overall symmetry combines the lattice symmetry with the symmetry of the basis and results in even more (230) *space groups*. Possible symmetry operations on the crystal, along with the intrinsic translational symmetries, are

- Rotations through multiples of $2\pi/n$ about symmetry axes
- Reflections at a mirror plane
- Inversions at the origin
- Rotation - Reflections
- Rotation - Inversions

Symmetry arguments can also play a role when defining a *unit cell*. There is no unique way of defining a unit cell (see Fig. 1.6) except the criterion that it has to contain the basis and the ability to completely tile the whole space with its geometrical shape. (That disqualifies for instance pentagons and septagons as unit cells in 2D).

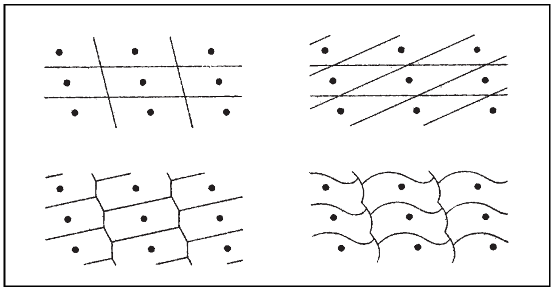

Figure 1.6: *Possible unit cells*

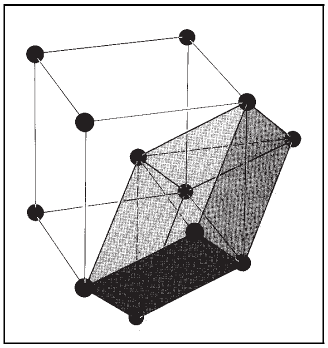

Figure 1.7: *bcc: conventional and primitive (grey) unit cell*

Since the primitive unit cell does not always resemble the full symmetry of the point lattice it is sometimes desirable to define larger unit cells. They are called conventional unit cells and mirror the complete symmetry of the crystal (see Fig. 1.7).

A widely used way to define a primitive unit cell with full symmetry properties is by virtue of the *Wigner-Seitz Cell.* [AM76]:*"The Wigner-Seitz Cell about a lattice point is the region of space that is closer to that point than to any other point".* It is independent from the choice of primitive vectors and naturally matches the tiling condition. It can be constructed (see Fig. 1.8)by virtually connecting the lattice point with all its nearest neighbors and bisecting the center of the connection with planes normal to them. The polyhedron formed by those planes and their intersections is the Wigner-Seitz Cell. In a 2D triangular lattice the Wigner-Seitz Cell is a hexagon, in a square lattice a square again. Three dimensional Wigner-Seitz Cells are shown in 1.11 on page 17.

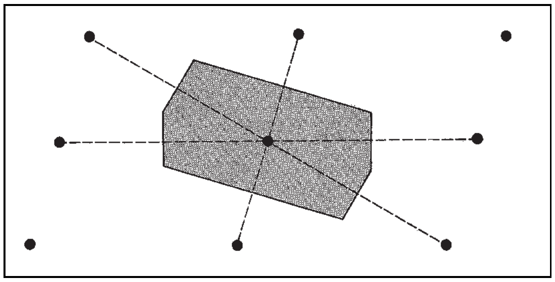

Figure 1.8: *On the construction of the Wigner-Seitz Cell*

1.1.2 Reciprocal Space

Any lattice has at least an intrinsic translational symmetry and exhibits periodicity. Therefore an approach with a Fourier series seems promising, when treating a crystal theoretically. It is always possible to express the space function, i.e. the position of the atomic potentials in real space as

$$U(\boldsymbol{r}) = \sum_{\boldsymbol{k}=0}^{\infty} U_{\boldsymbol{k}}\, e^{i\boldsymbol{k}\boldsymbol{r}}. \tag{1.2}$$

Due to the invariance of the space function by translating through a linear combination of basis vectors,

$$\sum_{\boldsymbol{k}=0}^{\infty} U_{\boldsymbol{k}}\, e^{i\boldsymbol{k}\boldsymbol{r}} = U(\boldsymbol{r}) = U(\boldsymbol{r}+\boldsymbol{R}) = \sum_{\boldsymbol{k}=0}^{\infty} U_{\boldsymbol{k}}\, e^{i\boldsymbol{k}\boldsymbol{r}}\, e^{i\boldsymbol{k}\boldsymbol{R}}, \tag{1.3}$$

the term $e^{i\boldsymbol{k}\boldsymbol{R}}$ has to vanish and consequently $\boldsymbol{k}\boldsymbol{R}$ must be a multiple of 2π. Since the $\boldsymbol{R}$'s form a discrete set of vectors in real space, i.e. the Bravais lattice, the $\boldsymbol{k}$'s satisfying this condition are also discrete in reciprocal space and form the reciprocal lattice. They shall be labeled $\boldsymbol{K}$ and can again be written as a linear combination of primitive vectors $\boldsymbol{g_i}$ in reciprocal, or k-space.

$$\boldsymbol{R} = n_1\boldsymbol{a_1} + n_2\boldsymbol{a_2} + n_3\boldsymbol{a_3} \tag{1.4}$$

$$\boldsymbol{K} = n_1\boldsymbol{g_1} + n_2\boldsymbol{g_2} + n_3\boldsymbol{g_3} \tag{1.5}$$

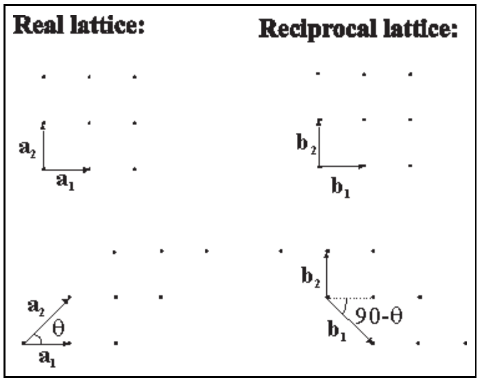

Figure 1.9: *Constructing the reciprocal lattice*

This leads to a condition for the primitive vectors $\boldsymbol{g_i}$ of the reciprocal lattice

$$\boldsymbol{g_i}\boldsymbol{a_j} = 2\pi\delta_{ij} \tag{1.6}$$

which simply states that they are perpendicular to the primitive vectors in real space and normalized to 2π. The $\boldsymbol{g_i}$'s can be calculated through

$$\boldsymbol{g_1} = 2\pi\frac{\boldsymbol{a_2}\times\boldsymbol{a_3}}{\boldsymbol{a_1}\cdot(\boldsymbol{a_2}\times\boldsymbol{a_3})} \tag{1.7}$$

and cyclic permutations.

1.1.3 The Brillouin Zone

An interesting and important fact is that the reciprocal lattice and the space lattice belong to the same point group, and consequently have equal symmetry properties. Therefore, the *Wigner-Seitz Cell* is the most common unit cell in the reciprocal lattice. Another reason is according to the *von Laue condition* $\boldsymbol{K} = \boldsymbol{k}' - \boldsymbol{k}$, which states the criterion for constructive interference is when incident and reflected wave vectors $\boldsymbol{k}, \boldsymbol{k}'$ of a scattered wave lie on the boundaries of the Wigner-Seitz Cell. The k-space Wigner-Seitz Cell is generally called *Brillouin-Zone.* Most important is the first Brillouin Zone, abbreviated *1.BZ*. Higher order Brillouin Zones can also be formed by employing not only the nearest neighbors but also the second, third, ... nearest neighbors to construct the Wigner-Seitz Cells.

For some important lattices the 1.BZs are shown in Fig. 1.10 and Fig. 1.11. The 1.BZ contains all relevant information about the crystal. In the case of a higher symmetry lattice, the 1.BZ can even further be reduced to the *Irreducible Brillouin Zone IBZ.* The rest of the 1.BZ can then be related to the IBZ by symmetry (see Fig. 1.10). High symmetry points of the BZ usually are named by capital letters according to conventions. The center of the 1.BZ is always referred to as the Γ-point. This corresponds to $\boldsymbol{k} = (0, 0, 0)$ and serves as the reference point when stating true directions, e.g. Γ-M, Γ-K or Γ-X. A complete reference to Brillouin Zones with their corresponding high symmetry points is given in the appendix A on page 115.

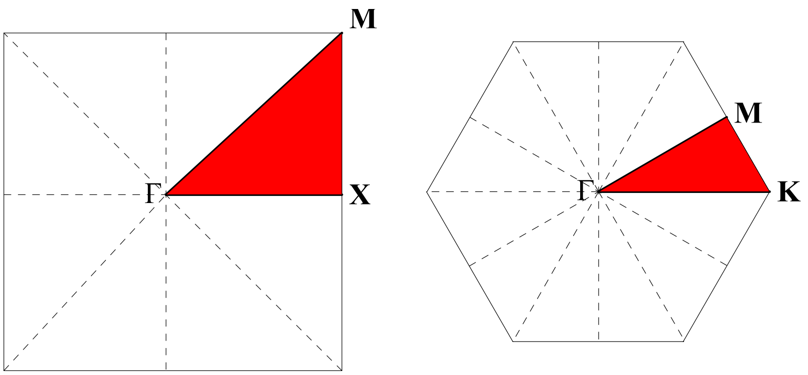

Figure 1.10: *1.BZ and IBZ for a square (left) and a triangular (right) 2-dimensional lattice*

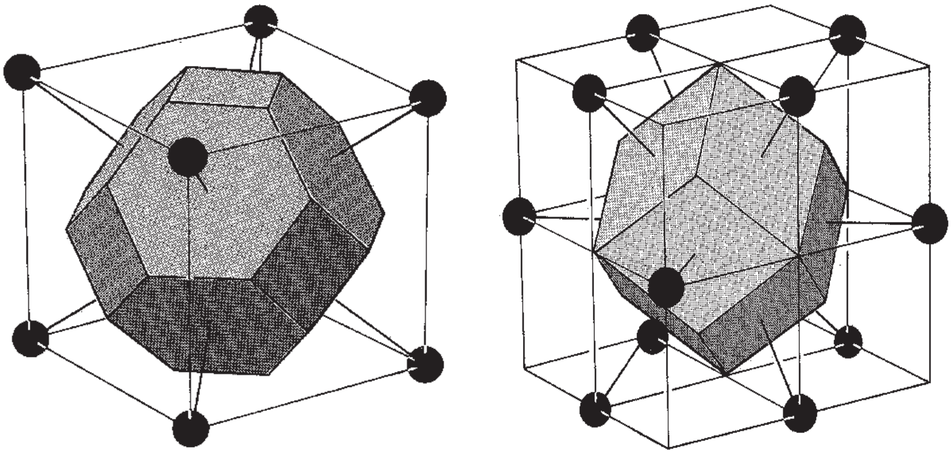

Figure 1.11: *1.BZ for a bcc (left) and a fcc lattice*

1.1.4 Bloch's Theorem

A fundamental aspect of solid state physics is solving the Schrödinger equation for electrons in a periodic atomic potential $U(\boldsymbol{r})$, which describes the crystal lattice.

$$H\,\Psi(\boldsymbol{r}) = \Big(-\frac{\hbar^2}{2m}\boldsymbol{\nabla}^2 + U(\boldsymbol{r})\Big)\,\Psi(\boldsymbol{r}) = E\,\Psi(\boldsymbol{r}) \tag{1.8}$$

In order to tackle this complex problem one needs approximations and well suited methods. An essential one is Bloch's theorem, which is based on the idealization of a perfect and infinite crystal. The perfect periodicity is accounted for by $U(\boldsymbol{r}) = U(\boldsymbol{r}+\boldsymbol{R})$ and the ideal, infinite crystal without boundaries can be simulated by imposing periodic boundary conditions, the so-called *Born - von Karman boundary conditions*. They can be expressed as

$$\Psi(\boldsymbol{r} + N_i\boldsymbol{a_i}) = \Psi(\boldsymbol{r}), \qquad i = 1,2,3 \tag{1.9}$$

where $N_i a_i = L_i$ represents the physical size of the crystal in the respective directions given by the primitive vectors $\boldsymbol{a}_i$.

Bloch's theorem expresses and is a consequence of the symmetry, i.e. the translational invariance of the lattice. In quantum mechanics (thinking in the Heisenberg picture) a fundamental theorem states the existence of a simultaneous set of eigenfunctions for two commuting operators. It is easy to proof (see for instance [AM76]) that the translation operator of the lattice $T_R = e^{i\boldsymbol{k}\boldsymbol{R}}$ and the Hamiltonian Eq. (1.8) commute. According to Bloch's theorem the mutual eigenstates of T_R and H can be written as

$$\Psi_{n\boldsymbol{k}}(\boldsymbol{r}) = u_{n\boldsymbol{k}}(\boldsymbol{r})\, e^{i\boldsymbol{k}\boldsymbol{r}} \tag{1.10}$$

where n is discrete and $\boldsymbol{k}$ restricted to the 1.BZ. Vitally $u(\boldsymbol{r})$ is a lattice periodic function satisfying the condition

$$u_{\boldsymbol{k}}(\boldsymbol{r}+\boldsymbol{R}) = u_{\boldsymbol{k}}(\boldsymbol{r}). \tag{1.11}$$

These solutions of our specific single electron Schrödinger equation, basically modulated plane waves, are usually referred to as Bloch modes, states, functions or waves. They form a complete, orthogonal set of functions. The index n is known as the *band index* and labels different eigenstates for a given $\boldsymbol{k}$. A convenient consequence is that the eigenvalues $E_n(\boldsymbol{k})$ in the Schrödinger equation

$$H\,\Psi_{n\boldsymbol{k}}(\boldsymbol{r}) = E_n(\boldsymbol{k})\,\Psi_{n\boldsymbol{k}}(\boldsymbol{r}) \tag{1.12}$$

are also periodic in k-space and therefore it is possible to reduce further discussions to the 1.BZ. Note, that although the k-space is discretized the $\boldsymbol{k}$'s can be assumed to be continuous, since their differences are infinitesimal in the order of

$$\Delta\boldsymbol{k} = \frac{2\pi}{V}, \tag{1.13}$$

where V is the actual macroscopic size of the crystal. This follows from the Born - von Karman boundary conditions in conjunction with Bloch's theorem. [AM76]

1.1.5 Electronic Band Structures

I will briefly present two common methods to approximate the solutions of the electronic Schrödinger equation and furthermore introduce the common representation scheme of a band structure diagram.

Tight Binding Model The tight binding model initially assumes a single, unperturbed potential with known eigenstates. This can be the effective potential for the valence electron for instance. Those atomic potentials are spatially located very close in a crystal and mutually influence each other. By gradually decreasing the distance or equivalently increasing their interaction the previously well defined states get distorted. They split up and broaden (see Fig. 1.12). Eventually, for very close potentials electronic bands form again. Mathematically this can be treated with the *Ritz Variational Principle*. It is also often referred to as the *Linear Combination of Atomic Orbitals (LCAO)* which is also a standard method to calculate Molecular Orbitals (MO).

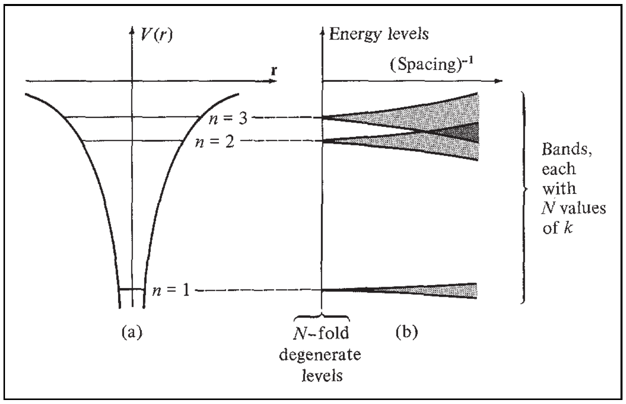

Figure 1.12: *Formation of bands for mutually influencing atomic potentials*

Nearly Free Electron Approach The nearly free electron approach is based on quantum mechanical perturbation theory. In the first step a negligibly weak potential *with* periodicity is assumed. Consequently the free dispersion curves emerge from the centers of every Brillouin zone and cross each other at their boundaries. In the case of a free electron the dispersion is a parabola

$$E(\boldsymbol{k}) = \frac{\hbar^2}{2m}\boldsymbol{k}^2 \tag{1.14}$$

(straight lines $\omega(\boldsymbol{k}) = c|\boldsymbol{k}|$ in the photonic case). In step two the strength of the potential is increased which lifts some of the degeneracies. By including more and more steps of quantum mechanical perturbation theory the real band structure can be approximated.

A common scheme to represent the (approximated) solutions of the Schrödinger equation for the electrons in the crystal is a *band structure diagram.* Hereby the eigenvalues $E_n(\boldsymbol{k})$ are plotted versus a continuous $\boldsymbol{k}$, which is usually restricted to the 1.BZ (*reduced-zone scheme*: see Fig. 1.13f). Further ways to represent the dispersion relations are in a *repeated-zone scheme* (e.g. Fig. 1.13g) or in an *extended-zone scheme* (Fig. 1.13e). For simplicity the eigenvalues are just plotted along lines of interest in the 1.BZ, which have high symmetries. In Fig. 1.14 a typical electronic band structure is shown. The different branches in the diagram are called (energy) bands. They are continuous in $\boldsymbol{k}$ and crossing or overlapping bands represent degeneracies. In some cases it is possible that there are no corresponding k-vectors for a specific energy value, which means that the energy has to change discontinuously. Such a forbidden energy region is called *band gap.* In electronic systems band gaps occur for instance between the valence- and the conduction band. The materials are then either insulators or semiconductors depending on the position of the Fermi level, which is the upper limit for electronic states.

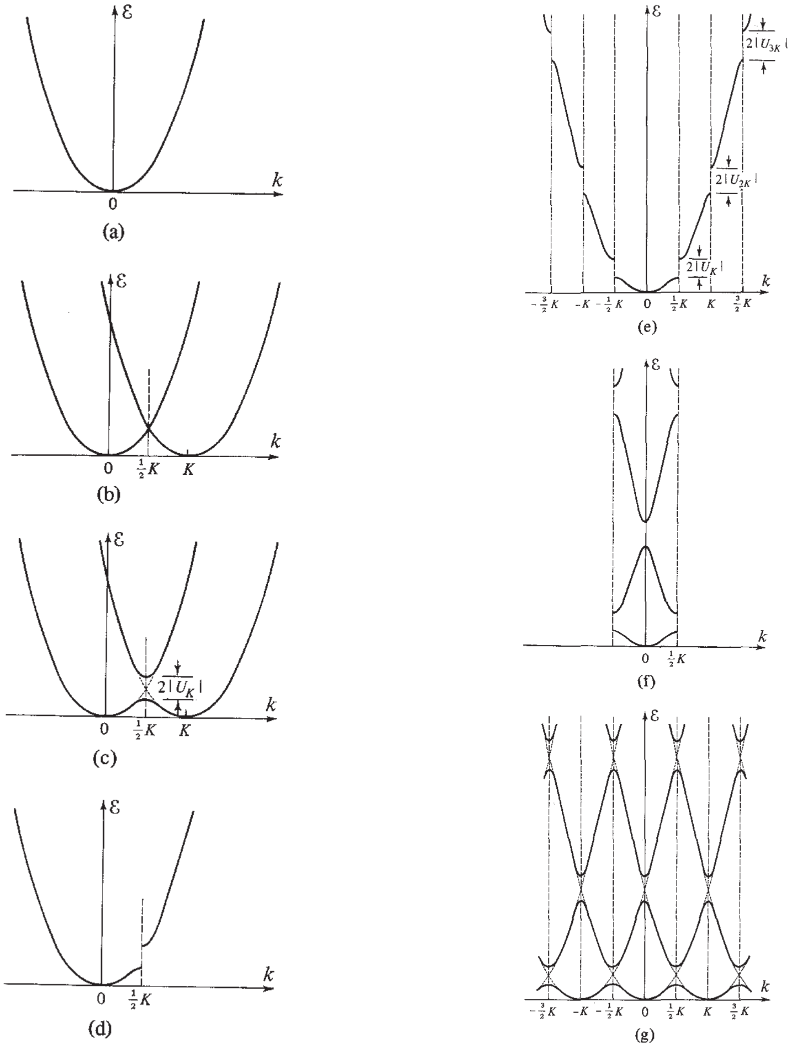

Figure 1.13: *Splitting of the bands in the Nearly-Free-Electron Approach (left) and different band structure representation schemes*

1.1.6 Density of States

Besides the band structure the *Density of States* (DOS) is an informative quantity. It is a measure for the allowed (electronic) states per differential energy interval. A sample DOS is shown in figure 1.15. Mathematically it can be defined as

$$\varrho(E) = 2\sum_n \int \frac{d\boldsymbol{k}}{(2\pi)^3}\, \delta(E - E_n(\boldsymbol{k})), \tag{1.15}$$

where n sums over the (relevant) bands and the integration is performed over any primitive unit cell. The validity of this definition can be seen when the total number

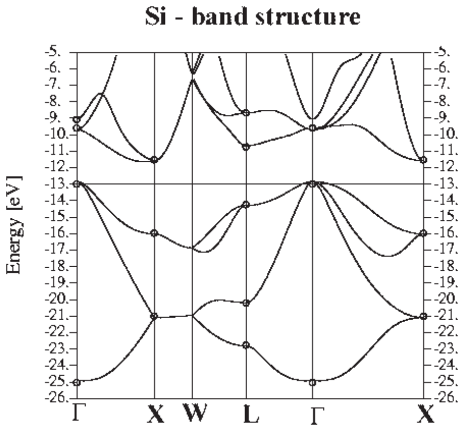

Figure 1.14: *Sample band structure diagram for Silicon (Si) in a diamond configuration*

of filled states is recovered:

$$N = \int_0^{E_{Fermi}} \varrho(E)\, dE \tag{1.16}$$

A sometimes more useful definition, relating the energy bands to the density of states, is simply derived by counting the allowed wave vectors in a certain energy range $E \leq E_n(\boldsymbol{k}) \leq E + dE$. In the infinitesimal limit of $\Delta\boldsymbol{k} \rightarrow d\boldsymbol{k}$ and $dE \rightarrow 0$ this can be formulated as an (energy-)surface $S_n(E)$ integral in k-space. In a next step the infinitesimal k-distance between $S_n(E)$ and $S_n(E + dE)$ can be reformulated with the gradient of the dispersion $\nabla E_n(\boldsymbol{k})$. This yields the explicit relation for the electronic DOS and the band structure:

$$\varrho(E) = 2\sum_n \int_{S_n(E)} \frac{dS}{(2\pi)^3} \frac{1}{|\nabla E_n(\boldsymbol{k})|}. \tag{1.17}$$

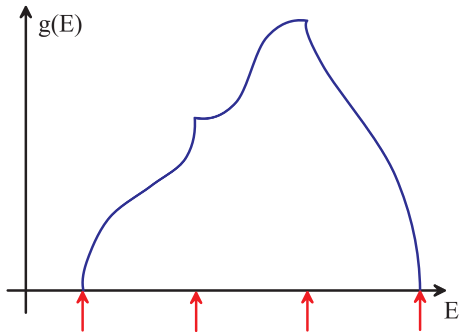

Figure 1.15: *Sample Density of States with characteristic van Hove singularities (marked by arrows)*

In case of a vanishing gradient the integrand diverges, but the singularities are integrable and result in so-called *van Hove singularities* in the DOS (see Fig. 1.15).

1.2 Electrodynamics Fundamentals

The second fundamental basis for any theoretical treatment of photonic crystals is of course electrodynamics. Generally all we need are Maxwell's equations.

$$\nabla \cdot \boldsymbol{D} = 4\pi\rho \tag{1.18}$$

$$\nabla \cdot \boldsymbol{B} = 0 \tag{1.19}$$

$$\nabla \times \boldsymbol{E} = -\frac{1}{c}\frac{\partial \boldsymbol{B}}{\partial t} \tag{1.20}$$

$$\nabla \times \boldsymbol{H} = \frac{4\pi}{c}\boldsymbol{j} + \frac{1}{c}\frac{\partial \boldsymbol{D}}{\partial t} \tag{1.21}$$

$\boldsymbol{E}$ and $\boldsymbol{H}$ are the macroscopic *electric* and *magnetic field* respectively, $\boldsymbol{D}$ and $\boldsymbol{B}$ represent the influence of matter and are called electric displacement and magnetic induction. Here it is recommended to use Maxwell's equations in their form for transparent, dielectric media. That is without any external charges ($\rho = 0$) and currents ($\boldsymbol{j} = \sigma\boldsymbol{E} = 0$).

In media the electric field and the displacement are related via the *dielectric constant* (or permittivity) ε. The magnetic field relates to the induction via the *magnetic permeability* μ. Both ε and μ are material constants and defined by the so-called material equations.

$$\boldsymbol{D} = \varepsilon\boldsymbol{E} \tag{1.22}$$

$$\boldsymbol{B} = \mu\boldsymbol{H} \tag{1.23}$$

These simple relations are only valid for homogeneous, isotropic and linear media. In the case of anisotropic media the dielectric constant as well as the magnetic permeability (but μ is generally very close to 1 for optical materials) is a 3x3 tensor which can also be position- and frequency-dependent to account for inhomogenities: $\varepsilon_{kl}(\boldsymbol{r}, \omega)$. If the medium is non-linear the relation between $\boldsymbol{D}$ and $\boldsymbol{E}$ has to include higher order coefficients ($\chi^{(1)}, \chi^{(2)}, etc$).

Maxwell's equations with $\boldsymbol{j} = 0$, $\rho = 0$ can be combined to yield the wave equations for $\boldsymbol{E}$ and $\boldsymbol{H}$.

$$\nabla^2\boldsymbol{E} - \frac{\varepsilon\mu}{c^2}\frac{\partial^2\boldsymbol{E}}{\partial t^2} = 0 \tag{1.24}$$

$$\nabla^2\boldsymbol{H} - \frac{\varepsilon\mu}{c^2}\frac{\partial^2\boldsymbol{H}}{\partial t^2} = 0 \tag{1.25}$$

These are standard equations of wave motion and suggest the existence of electromagnetic waves propagating with a phase-velocity of

$$v_{ph} = \frac{c}{\sqrt{\varepsilon\mu}} = \frac{c}{n} \tag{1.26}$$

where c is the speed of light. The deviation of v from c defines a new material property of optical density, the *refractive index* $n = \sqrt{\varepsilon\mu}$. This definition is only valid for lossless materials with real dielectric constant and magnetic permeability. For complex

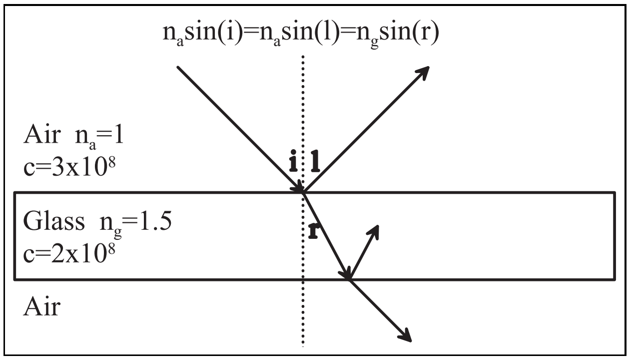

Figure 1.16: *Snell's law*

dielectric constants $\hat{\varepsilon}$ the definition $\hat{n}^2 = \hat{\varepsilon}\mu$ remains valid. Then the index of refraction n and the absorption coefficient α have to be calculated with the following relations

$$\begin{array}{lcl} \hat{n} = n(1 - i\kappa) & & n^2 = \frac{\mu}{2}\left(\sqrt{\varepsilon_r^2 + \varepsilon_i^2} + \varepsilon_r\right) \\ & \Longrightarrow & \\ \hat{\varepsilon} = \varepsilon_r + i\varepsilon_i & & \alpha^2 = \frac{2\mu\omega^2}{c^2}\left(\sqrt{\varepsilon_r^2 + \varepsilon_i^2} - \varepsilon_r\right), \end{array} \tag{1.27}$$

where $\varepsilon_i = \frac{4\pi\sigma}{\omega}$. As can be seen from this transformations the index of refraction is actually a foreign body in Maxwell's equations, but it governs macroscopic features like Snell's law for incident and refracted light:

$$n_i \sin\theta_i = n_r \sin\theta_r. \tag{1.28}$$

General solutions of the wave equations 1.24 and 1.25 are harmonic waves in space and time, usually expressed as :

$$\boldsymbol{E}(\boldsymbol{r}, t) = \boldsymbol{E}_0 \cdot e^{i(\boldsymbol{kr} - \omega t)} \tag{1.29}$$

$$\boldsymbol{H}(\boldsymbol{r}, t) = \boldsymbol{H}_0 \cdot e^{i(\boldsymbol{kr} - \omega t)} \tag{1.30}$$

The wave vector $\boldsymbol{k}$ denotes the direction of propagation and forms a triad with the $\boldsymbol{E}$ and $\boldsymbol{H}$ field since electromagnetic waves are transverse (in vacuum). The direction and mutual phase of the fields defines the polarization of the wave. The angular frequency ω is related to the frequency via $\omega = 2\pi\nu$ and the wave vector $\boldsymbol{k}$ to the wavelength through $\lambda = 2\pi/|\boldsymbol{k}|$. In vacuum, where ε and μ are unity, the linear *dispersion relation* $\omega = c|\boldsymbol{k}|$ holds. That is equivalent to $E = pc$ or $\lambda\nu = c$. In dielectric media this relation alters to

$$\frac{\omega}{|\boldsymbol{k}|} = v_{ph} = \frac{c}{n} \tag{1.31}$$

Unfortunately, harmonic and monochromatic waves are idealistic and in reality one always has to deal with a superposition of them, so-called wave packets. Wave-packets are characterized by a certain bandwidth $f(\omega)$ and therefore, per definition contain a range of neighboring frequencies. Quite generally this can be stated as:

$$\mathcal{F}(\boldsymbol{r},t) = \mathcal{F}_0 \int f(\omega)\, e^{-i[\omega t - \boldsymbol{k}_\omega \boldsymbol{r}]}\, d\omega \tag{1.32}$$

Since in dielectric media the dispersion relation $\omega\,(\boldsymbol{k})$ is not necessarily linear any more, the *group velocity* defines a measure for the propagation of the wave packet as a whole.

$$v_{gr} = \frac{\partial \omega}{\partial k} \qquad \text{i.e.} \qquad v_{gr} = \nabla_{\boldsymbol{k}}\, \omega(\boldsymbol{k}) \tag{1.33}$$

In contrast to the phase velocity the group velocity is always less than or equal to the speed of light. It represents the speed of the entire wave packet including the information and energy transmitted by it.

Chapter 2

Computational Techniques

After establishing the basis of solid state physics and electromagnetism, we are now interested in the behaviour of electromagnetic waves in a photonic crystal. In principle all the information is concealed in Maxwell's equations and we are left with solving them in a structure of a periodically modulated dielectric constant. There are different strategies to tackle this problem. Most of them revert to methods of solid state physics, but there are two main differences. On the one hand the vectorial character of light has to be taken into account, on the other hand, since photons are bosons the single particle problem delivers accurate results.

I will first introduce the most common one of these techniques, the Plane-Wave-Expansion method (PWEM) based on the formalism given by Ho, Chan and Soukoulis (*HCS method*) [HCS90].

A second important approach that I want to present in detail is the Transfer Matrix method by Pendry [PM92]. This formalism does not rely on approximate solid state methods but rather solves Maxwell's equations directly for a given configuration of a periodically modified dielectric constant.

Finally I will present and briefly discuss some other methodologies as well as their specific advantages and disadvantages along with applications.

2.1 Plane Wave Expansion Method

In the PWEM the solutions of a master equation, which is deduced from Maxwell's equations, are expanded in a set of plane waves by utilizing Bloch's theorem. In the issue of PRL **65** in (1990) three different approaches to construct a suitable master equation [HCS90, ZS90, LL90] were presented. The solution offered by Ho, Chan and Soukoulis is the most commonly used technique to calculate photonic band structures nowadays.

In order to simplify the basic problem, starting from Maxwell's equations the assumptions of a

1. linear
2. isotropic
3. frequency independent
4. lossless

material are made. This reduces the dielectric constant to an intrinsic position dependence $\varepsilon(\boldsymbol{r})$. The magnetic permeability μ is generally very close to unity and therefore set to 1. Under these assumptions Maxwell's equations read

$$\begin{aligned}
\nabla \cdot (\varepsilon(\boldsymbol{r})\, \boldsymbol{E}(\boldsymbol{r},t)) &= 0 &\quad (2.1)\\
\nabla \cdot \boldsymbol{H}(\boldsymbol{r},t) &= 0 &\quad (2.2)\\
\nabla \times \boldsymbol{E}(\boldsymbol{r},t) &= -\frac{1}{c}\frac{\partial \boldsymbol{H}(\boldsymbol{r},t)}{\partial t} &\quad (2.3)\\
\nabla \times \boldsymbol{H}(\boldsymbol{r},t) &= \frac{\varepsilon(\boldsymbol{r})}{c}\frac{\partial \boldsymbol{E}(\boldsymbol{r},t)}{\partial t} &\quad (2.4)
\end{aligned}$$

The time dependency can be separated by an common harmonic ansatz

$$\boldsymbol{H}(\boldsymbol{r},t) = \boldsymbol{H}(\boldsymbol{r})\, e^{i\omega t} \quad \text{and} \quad \boldsymbol{E}(\boldsymbol{r},t) = \boldsymbol{E}(\boldsymbol{r})\, e^{i\omega t}. \tag{2.5}$$

Inserting this harmonic ansatz into equations 2.1 & 2.2 leads to the simple, time-independent divergence equations 2.6 and through equations 2.3, 2.4 to the coupled curl equations relating the magnetic and electric fields 2.7.

$$\begin{aligned}
\nabla \cdot (\varepsilon(\boldsymbol{r})\boldsymbol{E}(\boldsymbol{r})) = 0 &\qquad \nabla \cdot \boldsymbol{H}(\boldsymbol{r}) = 0 &\quad (2.6)\\
\nabla \times \boldsymbol{E}(\boldsymbol{r}) = -\frac{i\omega}{c}\boldsymbol{H}(\boldsymbol{r}) &\qquad \nabla \times \boldsymbol{H}(\boldsymbol{r}) = \frac{i\omega}{c}\varepsilon(\boldsymbol{r})\,\boldsymbol{E}(\boldsymbol{r})\,. &\quad (2.7)
\end{aligned}$$

These relations can be de-coupled for either one of the fields. It proves superior to consider the magnetic field first, because this results in a hermitian differential operator [JMW95]. This is of great importance since it eases subsequent numerical methods. Eliminating $\boldsymbol{E}$ from Eq. (2.7) yields our *master equation*:

$$\boxed{\nabla \times \left(\frac{1}{\varepsilon(\boldsymbol{r})}\nabla \times \boldsymbol{H}(\boldsymbol{r})\right) = \left(\frac{\omega}{c}\right)^2 \boldsymbol{H}(\boldsymbol{r})} \tag{2.8}$$

To point out its character of an eigenvalue equation it can be written as

$$\Lambda \boldsymbol{H}(\boldsymbol{r}) = \varpi \boldsymbol{H}(\boldsymbol{r}) \tag{2.9}$$

with the hermitian operator Λ and the real, positive eigenvalues ϖ corresponding to $\left(\frac{\omega}{c}\right)$. In the progression of this work I will refer to the frequencies ω as being the eigenvalues. They can straightforwardly be recovered from ϖ and are the physical significant quantity.

Once the magnetic field is known, the electric field can subsequently always be recovered through

$$\boldsymbol{E}(\boldsymbol{r}) = \left(\frac{-ic}{\omega\varepsilon(\boldsymbol{r})}\right) \nabla \times \boldsymbol{H}(\boldsymbol{r})\,. \tag{2.10}$$

Therefore the remaining problem is solving our master wave equation 2.8. Basically all the information about the crystal is contained in the position dependent dielectric tensor $\varepsilon(\boldsymbol{r}) = \varepsilon(\boldsymbol{r}+\boldsymbol{R})$, where $\boldsymbol{R}$ is a lattice vector. Ideally it would be perfectly periodic without boundaries. Mathematically we are confronted with an eigenvalue problem for a differential operator on $\boldsymbol{H}$, which is hermitian. Therefore the eigenfunctions $\boldsymbol{H}(\boldsymbol{r})$ have real eigenvalues ω, they are orthogonal, and they can be obtained by a variational principle and have distinct symmetry properties. Primarily we have to deal with a set of 3 coupled differential equations with periodic coefficients in 2.8. The best approach to this problem is employing Bloch's theorem, called *Floquet theorem* in optics. So the ansatz is to expand the dielectric tensor and the magnetic field in a Fourier series on the reciprocal lattice $\boldsymbol{G}$

$$\begin{aligned} \varepsilon(\boldsymbol{r}) &= \sum_{\boldsymbol{G}} \varepsilon_{\boldsymbol{G}}\, e^{i\boldsymbol{G}\boldsymbol{r}} && (2.11) \\ \boldsymbol{H}_{\boldsymbol{k}}(\boldsymbol{r}) &= \sum_{\boldsymbol{G}} \sum_{\lambda=1}^{2} h_{\boldsymbol{G}}^{\lambda}\, e_{\boldsymbol{G}}^{\lambda}\, e^{i(\boldsymbol{k}+\boldsymbol{G})\boldsymbol{r}} && (2.12) \end{aligned}$$

where λ represents the two transverse polarizations of the wave vector $\boldsymbol{k}$ labeling the solutions. Inserting 2.11 & 2.12 into the master equation 2.8 leads to an infinite eigenvalue problem, for the eigenvalues $\omega_n(\boldsymbol{k})$ and the eigenfunctions $\boldsymbol{H}_{n\boldsymbol{k}}(\boldsymbol{r})$, i.e. its Fourier coefficients $h_{\boldsymbol{G}}^{\lambda}$.

$$\begin{aligned} \sum_{\boldsymbol{G}} \sum_{\lambda=1}^{2} M_{\boldsymbol{G}\boldsymbol{G}'}^{\lambda\lambda'}\, h_{\boldsymbol{G}'}^{\lambda'} &= \left(\frac{\omega}{c}\right)^2 h_{\boldsymbol{G}}^{\lambda} && (2.13) \\ \text{with} \quad M_{\boldsymbol{G}\boldsymbol{G}'}^{\lambda\lambda'} &= |\boldsymbol{k}+\boldsymbol{G}| \cdot \frac{\boldsymbol{e}_{\boldsymbol{G}}^{\lambda} \cdot \boldsymbol{e}_{\boldsymbol{G}'}^{\lambda'}}{\varepsilon_{\boldsymbol{G}-\boldsymbol{G}'}} \cdot |\boldsymbol{k}+\boldsymbol{G}'| && (2.14) \end{aligned}$$

This matrix eigenvalue problem can be solved by standard matrix-diagonalization methods if truncated by only retaining a finite number of reciprocal lattice vectors. The difficulty is obtaining the Fourier coefficients of the inverse dielectric tensor $\varepsilon(\boldsymbol{r})$ in Eq. (2.14). With the *HCS method* the position-dependent dielectric function is evaluated in the real space unit cell, Fourier transformed into reciprocal space and subsequently inverted. This method proves to converge significantly faster than the *direct method*, which first inverts $\varepsilon(\boldsymbol{r})$ and then applies the Fourier transform. Matrix sizes on the order of $\sim$ 750 plane waves are sufficient to obtain accuracies better than 1% for the 10 lowest bands [HCS90]. The intrinsic results of the PWEM are of course the dispersion relations $\omega_{n\lambda}(\boldsymbol{k})$ (eigenvalues) along with the spatial electromagnetic field distributions $\boldsymbol{H}_{\boldsymbol{k}n\lambda}(\boldsymbol{r}), \boldsymbol{E}_{\boldsymbol{k}n\lambda}(\boldsymbol{r})$ (eigenfunctions), as well as photonic density of states.

Alternative approaches to construct a master equation from Maxwell's equations are also possible, but were not as successful as the HCS method. For instance, the master equation proposed by Zhang and Satpathy [ZS90] is

$$\begin{gathered} -\nabla^2 \boldsymbol{D} = \left(\tfrac{\omega}{c}\right)^2 \boldsymbol{D} + \nabla \times \nabla \times [V(\boldsymbol{r})\boldsymbol{D}] \\ \text{with} \quad V(\boldsymbol{r}) = 1 - \tfrac{1}{\varepsilon(\boldsymbol{r})} \end{gathered} \tag{2.15}$$

the one Leung and Liu [LL90] suggested looks like

$$\nabla \times (\nabla \times \boldsymbol{E}) = \left(\frac{\omega}{c}\right)^2 \varepsilon(\boldsymbol{r})\, \boldsymbol{E}. \tag{2.16}$$

Both equations can also be solved with a Plane-Wave-Expansion method and yield the same results but lack good convergence properties due to less suitable differential operators. Römer [Roe00] suggested an improvement to Eq. (2.16) in order to regain a positive definite, symmetric operator:

$$\nabla \cdot (\nabla \cdot \boldsymbol{E}) \doteq \Lambda \boldsymbol{E} = \left(\frac{\omega}{c}\right)^2 \varepsilon(\boldsymbol{E}) \tag{2.17}$$

where quite generally $\varepsilon(\boldsymbol{E})$ is a position-dependent function of $\boldsymbol{E}$. In the linear case it assumes $\varepsilon(\boldsymbol{E})_i = \boldsymbol{D}_i = \varepsilon_{ij}\boldsymbol{E}_j$. Defining

$$\boldsymbol{F} = \varepsilon^{1/2}(\boldsymbol{E}) \quad \text{and} \quad K = \varepsilon^{-1/2}\, \Lambda\, \varepsilon^{-1/2} \tag{2.18}$$

yields the hermitian eigenvalue equation

$$K\boldsymbol{F} = \left(\frac{\omega}{c}\right)^2 \boldsymbol{F}. \tag{2.19}$$

Unfortunately it is shown in [JMW95] that the fields $\boldsymbol{F}$ are not transverse anymore. That makes this approach less suitable because the transverse character of $\boldsymbol{H}$ is of great utility for the numerical methods.

2.2 Transfer-Matrix Techniques

In contrast to PWEMs the Transfer-Matrix method does not necessarily assume an ideal crystal with perfect, boundless periodicity. It is rather an on-shell, finite element method and directly calculates the flow of the electromagnetic fields throughout a small, real structure. Therefore it does not rely on Fourier space and is thus better capable of incorporating disorders or defects. Additionally its intrinsic features allow the determination of transmission and reflection properties. This cannot be done with PWEMs due to the existence of uncoupled bands. *Uncoupled bands* are Bloch modes of distinct orthogonal symmetry to an incident plane wave. Thus they cannot support the propagation of a plane wave. The existence of those uncoupled bands was proven by Sakoda [Sak95] through group theoretical considerations. The original Transfer-Matrix method was presented by Pendry and MacKinnon in 1992 [PM92] as a further development of on-shell methods in low-energy electron diffraction theory. Later modifications and extensions are based on this, see for instance [ET95, ET96].

The Transfer-Matrix approach represents the electromagnetic fields on a discrete mesh of space points where Maxwell's equations are evaluated.

$$\nabla \times \boldsymbol{E} = -\frac{\partial \boldsymbol{B}}{\partial t} \quad \text{and} \quad \nabla \times \boldsymbol{H} = \frac{\partial \boldsymbol{D}}{\partial t} \tag{2.20}$$

As a first step, the structure has to be discretized in real space. The mesh points can be simply defined as

$$\boldsymbol{r} = n_1 a \cdot \boldsymbol{e}_x + n_2 b \cdot \boldsymbol{e}_y + n_3 c \cdot \boldsymbol{e}_z \quad n_i : \text{integers}, \tag{2.21}$$

where $\boldsymbol{e}_x, \boldsymbol{e}_y, \boldsymbol{e}_z$ usually span an orthogonal lattice. This is should not be mis-understood as the unit cell of the structure under study, which is subdivided by this mesh. An orthogonal mesh is the prime choice and could always be altered by coordinate transformation into a better adapted one [WP96].

Secondly, the equations 2.20 are transformed using the harmonic ansatz and are expressed in $(\omega, \boldsymbol{k})$ space:

$$i\boldsymbol{k} \times \boldsymbol{E} = +i\omega \boldsymbol{B} \quad \text{and} \quad i\boldsymbol{k} \times \boldsymbol{H} = -i\omega \boldsymbol{D} \tag{2.22}$$

where $\boldsymbol{k}$ can be approximated for small values of a, b, c by:

$$\boldsymbol{k}_x \approx \frac{1}{ia}[e^{ik_x a} - 1] \tag{2.23}$$

$$\boldsymbol{k}_y \approx \frac{1}{ib}[e^{ik_y b} - 1] \tag{2.24}$$

$$\boldsymbol{k}_z \approx \frac{1}{ic}[e^{ik_z c} - 1] \tag{2.25}$$

This can be inserted to equations 2.22 which are then Fourier transformed into real space. Now the fields $\boldsymbol{D}(\boldsymbol{r})$ and $\boldsymbol{B}(\boldsymbol{r})$ can be substituted by $\varepsilon(\boldsymbol{r})\boldsymbol{E}(\boldsymbol{r})$ and $\mu(\boldsymbol{r})\boldsymbol{H}(\boldsymbol{r})$, respectively. Eventually eliminating the components of the fields in propagation direction, e. g. E_z and H_z leads to determining equations for $\mathcal{F}(\boldsymbol{r} + c)$. Here $\mathcal{F}(\boldsymbol{r})$ is defined as 4-dimensional vector containing the x- and y-components of the fields $(E_x(\boldsymbol{r}), E_y(\boldsymbol{r}), H_x(\boldsymbol{r}), H_y(\boldsymbol{r}))$. With this notation a transfer matrix T can formally be defined as

$$\mathcal{F}(\boldsymbol{r} + c) = T_{rr'}\mathcal{F}(\boldsymbol{r'}) \tag{2.26}$$

with the $\boldsymbol{r'}$ points on a plane. This transfer matrix only depends on $\omega, \varepsilon(\boldsymbol{r}), \mu(\boldsymbol{r})$ and relates the fields in one layer of cells to the next layer in z-direction (see fig. 2.1). The actual matrix components are calculated in [Pen94].

As boundary conditions either the dielectric constant of the embedding material can be taken into account. Or, for periodic arrangements in any directions Bloch's theorem can be invoked.

$$\begin{aligned} \boldsymbol{E}(\boldsymbol{r} + \boldsymbol{R}) &= e^{i\boldsymbol{k}\boldsymbol{R}}\boldsymbol{E}(\boldsymbol{r}) \\ \boldsymbol{H}(\boldsymbol{r} + \boldsymbol{R}) &= e^{i\boldsymbol{k}\boldsymbol{R}}\boldsymbol{H}(\boldsymbol{r}) \end{aligned} \tag{2.27}$$

where R is a lattice vector as in definition 1.1 on page 12.

A consistency check of the results can always be done by virtue of a constant energy flow in form of the Poynting vector ($\boldsymbol{S} = \frac{c}{4\pi}[\boldsymbol{E} \times \boldsymbol{H}]$) through the layers.

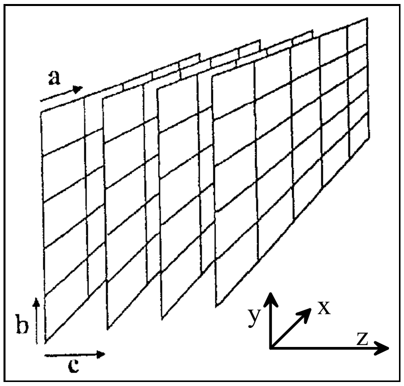

Figure 2.1: *A mesh for the Transfer-Matrix method, which expresses the fields in a given plane in terms of fields in the previous plane*[Pen94]

When trying to find the transmission and reflection coefficients for the whole structure, first of all the coefficients for a single slice, i. e. layer of cells have to be calculated. In order to achieve this, the known transfer matrix T is unitarily transformed into a free wave basis $\hat{T} = STS^{-1}$. This results in a form where the quadrants of $\hat{T}$ can easily be related to the reflection and transmission coefficients for this particular slice. The total transmission and reflection for a slab of a material consisting of several slices could then ideally be obtained by determining the total T-matrix through

$$T(L) = \prod_{z=1}^{L/z} T(z) \tag{2.28}$$

and re-applying the above explained procedure. Unfortunately this elegant prescription for simply adding together slices can suffer from fatal numerical instabilities [Pen94]. To avoid this problem multiple scattering formulae have to be used iteratively to add a new layer. This increases the computational load but leads to more stable results.

In order to identify the wave vectors $\boldsymbol{k}$, the presumably known eigenvalues of the transfer matrix for a period system have to be compared to the term e^{ikZ} from Bloch's theorem:

$$T(Z)\mathcal{F}(z) = \mathcal{F}(z+Z) = e^{ikZ}\mathcal{F}(z) \tag{2.29}$$

Through this step the dispersion relation, albeit in a form of $\boldsymbol{k}(\omega)$ as opposed to the conventional $\omega(\boldsymbol{k})$, can be obtained.

2.3 Various Other Methods

Besides the Plane-Wave-Expansion and Transfer-Matrix method there are other approaches to treat electromagnetic waves in periodic dielectrics. I just briefly want to address them here. A recent review on this topic can be found in the article of Berger [Ber99].

Scalar Wave Early approaches neglected the vectorial character of the electromagnetic field and performed scalar computations. Nevertheless the calculations were able to explain some experimentally verified results, but many features could not be accounted for. In fact when dealing with a 2-dimensional crystal the scalar wave approach can be exact. In this case it is possible to de-couple the two polarization states and treat them independently.

Nearly-Free Photon Approach A straightforward but very heuristic argument is the nearly-free photon approach. It is equivalent to its counterpart in solid state physics, with the exception that the free dispersion curves in the photonic case are linear $\omega = c|\boldsymbol{k}|$ as opposed to a quadratic energy-momentum relation $E = \frac{\hbar^2}{2m}k^2$.

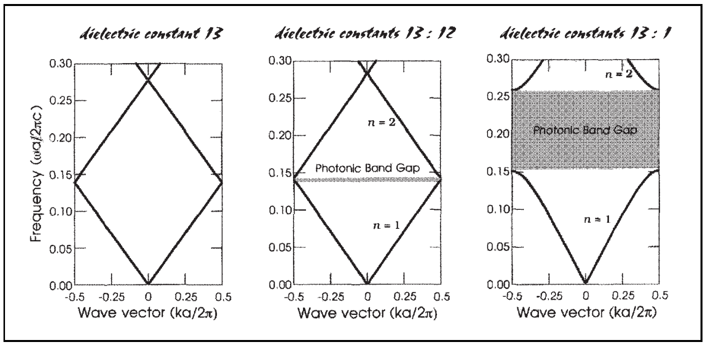

Figure 2.2: *Evolution of a photonic band gap by gradually increasing the dielectric contrast for a 1D Bragg stack.*[JMW95]

Considering a crystal with negligible difference in the index of refraction but periodicity nevertheless, the photon dispersion curves are still linear as in free space. But due to the periodicity in the crystal the dispersion curves emerge from the centers of every Brillouin zone and cross each other at its boundaries. Subsequently, by gradually increasing the refractive index ratio, i.e. applying perturbation theory the degeneracies at the boundaries of the Brillouin Zone are lifted and the dispersion curves repel each other. In this fashion distinct bands and band gaps develop. Although this method follows rather heuristic arguments, it reflects some basic features of the photonic bands. For example it reflects the influence of the geometrical shape of the Brillouin Zone, which results in different slopes for different directions and therefore in anisotropies for higher bands (see fig. 3.10 on page 46).

Diffraction Grating And Scattering Method Diffraction Grating methods model a 2-dimensional photonic crystal as a stack of N grids. The effect of a single grating on the field is transferred to the next layer iteratively. In that sense this approach is related to the Transfer-Matrix method. Scattering methods are also purely electromagnetic and describe the photonic crystal as a simple set of *Bragg-scatterers* [Rus86, Yeh79]. They can be superior to other methods when very weak scattering is considered. Forbidden bands are the consequence of negative interference between multiple scattered waves, matching the Bragg conditions.

Tight-Binding Model Another already mentioned famous method in solid state physics, besides the Nearly-Free Electron approach, is the Tight-Binding model. By far not as popular in photonics, it is nevertheless very interesting to discuss. The method is most useful for geometrical objects with well known eigenmodes, for instance dielectric spheres. Their eigenmodes are vector spherical waves, the so-called Mie resonances. A very thorough treatment of this case was done by Ohtaka [OT96a, OT96b, OT96c, OUT96]. In a mathematical way the set of eigenvalues in the bulk crystal (i.e. the bands) are calculated through an expansion with spherical waves. They are, in contrast to plane waves well suited for the problem and also form a complete and orthogonal set of functions.

The convergence properties and therefore the computational load of this method are very good compared to other methods. This is due to the geometrically adapted set of functions used for the expansion. Another advantage of this method is the interpretation of flat bands, i.e. slow photons (also called *heavy photons*) as propagating Bloch waves. The group velocity of those flat dispersion curves can be in the order of $c/100$. A way to look at this in the Tight-Binding picture is that spherical waves of single spheres couple to neighboring spheres through some energy leaking. This mixing effect leads to a well-defined mode propagation from sphere to sphere. So the light comes crawling along, spends some time in every sphere (localized modes of Mie resonances already have a finite lifetime in an isolated sphere) and then hopps on to the next sphere. Although this method employing vector spherical waves as basis functions shows some advantages, it is not very widespread. Mostly because of its limitations to spherical/ellipical objects, which just recently got more attention in the work on opals and inverted opals [BCG$^+$00].

Rayleigh-Ritz Approach Again this is a technique where the computation of the photonic bands is based on a decomposition of the fields into a complete and orthogonal set of well adjusted functions [FG97, FGV98]. These functions preferably possess the same symmetry as the crystal with discontinuities associated to the position dependent dielectric constant $\varepsilon(\boldsymbol{r})$ and therefore have great advantages in convergence, avoiding the Gibbs phenomenon (sharp peaks at the corners of a Fourier transformed rectangular function). Unfortunately one needs a new set of functions for any variation of the geometry.

Finite Difference Time Domain Technique It is a somewhat similar approach to the Transfer-Matrix method. As its name already implies, Finite Difference Time Domain techniques are also based on finite elements methods, but discretizes the fields in time [RJ96]. It allows to map the temporal evolution of light pulse propagation and is therefore particularly efficient for calculating cavity quality factors and emission rates.

In summary the different theoretical methods to treat photonic crystals usually revert to well established solid state physics methods. The approaches are numerous and increasing. See for instance Vol.8 No.3 (Jan.29, 2001) of Optics Express `[http://www.opticsexpress.org/]`.

2.4 Computer Programs

In order to make use of the ideas presented above and draw quantitative conclusions, the aid of computers is inevitable. Therefore the methods have to be implemented in source code. This again allows many degrees of freedom owing to different algorithms and programming languages. Some of this software is already freely available. For instance the MIT Photonic Bands Package `[http://ab-initio.mit.edu/mpb/]` from Stephen Johnson at the MIT in the Joannopoulos group.

For the calculations and simulations in this work, I was allowed to use the programs developed by Ovidiu Toader at the University of Toronto in the group of Prof. Sajeev John and by Prof. John Pendry at the Imperial College of Science, London. I learnt how to operate and modify these codes for my needs and want to give a very quick overview of them.

2.4.1 by Ovidiu Toader

The program Ovidiu Toader created is based on the Plane-Wave-Expansion method and implemented in modular C++ code. It runs under Linux and uses standard mathematical packages, e.g. for Fast Fourier Transforms (FFT) and Linear Algebra. CVS (Concurrent Versions System) keeps track of the source code files `[http://www.CVShome.org]`. For instance it lets only compile new or modified ones. The compilation is executed by a 'homemade' Python command: `pmake`. Python `[http://www.python.org]` is a script language comparable to Perl. The basic file structure of the complete program looks like:

```
/home/oettl/PBG:                     /home/oettl/PBG/src:

 * CVS/                               * Anton/
 * doc/                               * BandStructure/
 * etc/                               * CVS/
 * include/                           * Config/
 * lib/                               * CoordinateSystem/
 * mk/                                * Crystal/
 * python/                            * DOS/
 * src/                               * Dielectric/
                                      * EMField/
                                      * NL/
                                      * PlaneWaves/
                                      * PointGroup/
                                      * Shape/
                                      * TempBandstructure/
                                      * Visualization/
                                      * mkf
                                      * readme
```

In `/PBG/doc/` the documentation of the source code files, located in `/PBG/src/` can be viewed in HTML format. The `/PBG/src/` directory, containing the single classes is subdivided in thematic, self-explaining directories `Crystal/` for instance contains 2- and 3-dimensional point lattices and `Shape/` different geometrical as a basis to generate desired crystal structures. New classes or modules can easily be added any time by just creating them, putting them in the relevant directory and compiling with `pmake` and `pmake install` subsequently in `/PBG/src/`.

In the `main` program those classes are simply assembled as building blocks to calculate the dispersion relations $\omega_n(\boldsymbol{k})$ in a band structure diagram, the photonic density of states DOS, the spatial electromagnetic field distribution or the real space shape of the crystal structure. For a sample `main` program see appendix B on page 125. It is compiled to an executable file through the `pmake` command and the `mkf`-script.

2.4.2 by John Pendry

The above explained Transfer-Matrix method was implemented originally by J. Pendry, P. M. Bell, A. J. Ward and L. M. Moreno in Fortran code. This code along with documentation and permission to use was kindly provided by Prof. John Pendry [`http://www.sst.ph.ic.ac.uk/photonics/`].

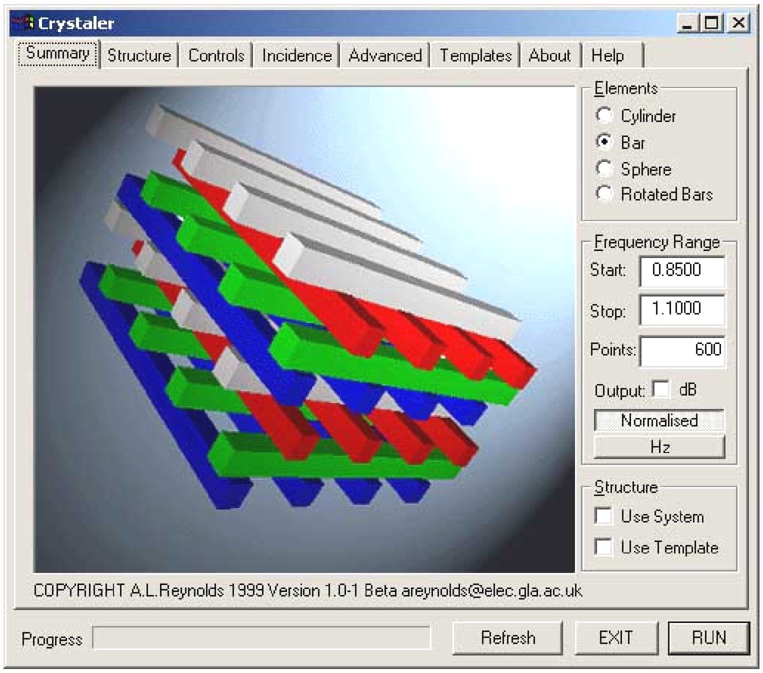

Elements
○ Cylinder
● Bar
○ Sphere
○ Rotated Bars

Frequency Range
Start: 0.8500
Stop: 1.1000
Points: 600
Output: ☐ dB
Normalised
Hz

Structure
☐ Use System
☐ Use Template

COPYRIGHT A.L.Reynolds 1999 Version 1.0-1 Beta areynolds@elec.gla.ac.uk

Progress

Figure 2.3: *Graphical user interface of the Translight program by A. Reynolds and vrml representation of a Lincoln-log structure*

Besides that, Andrew Reynolds at the University of Glasgow programmed a software with graphical user interface GUI on top of the initial code. It is called *Translight* and runs under Windows. It is freely available at [`http://www.elec.gla.ac.uk/~areynolds/Software/SoftwareMain.htm`] and offers convenient interaction with the program. Although the interaction through control and template files would be recommended due to higher transparency. It includes some pre-defined structures which can serve as case studies and examples to program templates for custom built structures. A desired structure can be implemented by repeating cells or blocks of cells through space. This cell can simply be the unit cell of a lattice. With more cells, more complex structures (with defects) can be generated. The geometry of the cells and the mesh on it has to be programmed in a template file. Unfortunately one is limited to elements consisting of bars, rods or spheres. Eventually the crystal structure can be output and viewed in Virtual Reality VRML. The final transmission and reflection curves are output on a frequency scale adjustable in range and accuracy.

Chapter 3

Discussion Of General Features

After establishing the theoretical framework and computational techniques we can now move on to look at some representative results and interpret their features with regard to specific designs and optimization of photonic crystals. Although 3-dimensional photonic crystals are of great importance, all relevant features are already present in the 2-dimensional case. Hence I will mostly deal with 2-dimensional examples here, because they have simpler structures and are easier to imagine and visualize.

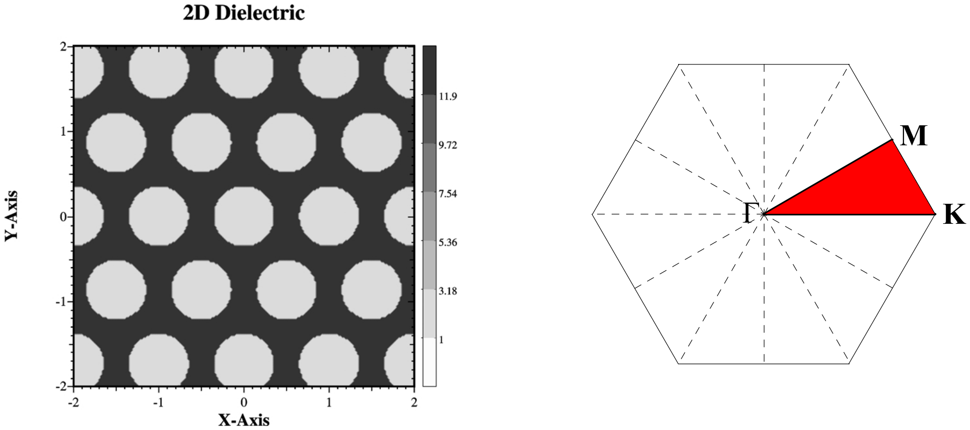

Figure 3.1: *Sample photonic crystal: Si (n=3.45) with air columns of* $r/a =$ 0.35 *in hexagonal lattice, and its corresponding 1.Brillouin Zone*

Let us consider a sample system. It consists of air columns in a backbone of Silicon. The refractive index of Si in the infrared is 3.45 ($\rightarrow \varepsilon = 11.9$). The columns extend in the z-direction and are arranged in an ordered triangular lattice in the xy-plane with a ratio of radius to lattice constant r/a of 0.35. A top-view of the structure along with its corresponding 1.BZ is shown in Fig. 3.1.

3.1 Photonic Band Structures

In analogy to solid state physics (see page 18) the common way to represent the dispersion relations is in band structure diagrams. Here $\omega_n(\boldsymbol{k})$ is plotted versus a continuous $\boldsymbol{k}$ along lines of high symmetry ($\Gamma - K$, $\Gamma - M$ and the connection of $M - K$, which does not correspond to an actual direction) in the 1.BZ, where n labels the bands. The energy axis is normalized ($y = \frac{\omega a}{2\pi c} = \frac{a}{\lambda}$) by the lattice constant a in order to take advantage of the scalability of Maxwell's equations. That is because no intrinsic length scale is given by them. So the results can be applied to the complete range of electromagnetic radiation provided an appropriate structure with the same dielectric contrast.

As a representative example the band structure of our sample system is shown in Fig. 3.2. It was generated with the PWEM program. The parameters were: Triangular lattice, disc motif $r/a = 0.35$, $\varepsilon_{backbone} = 11.9$, $\varepsilon_1 = 1$, H-polarization (TE).

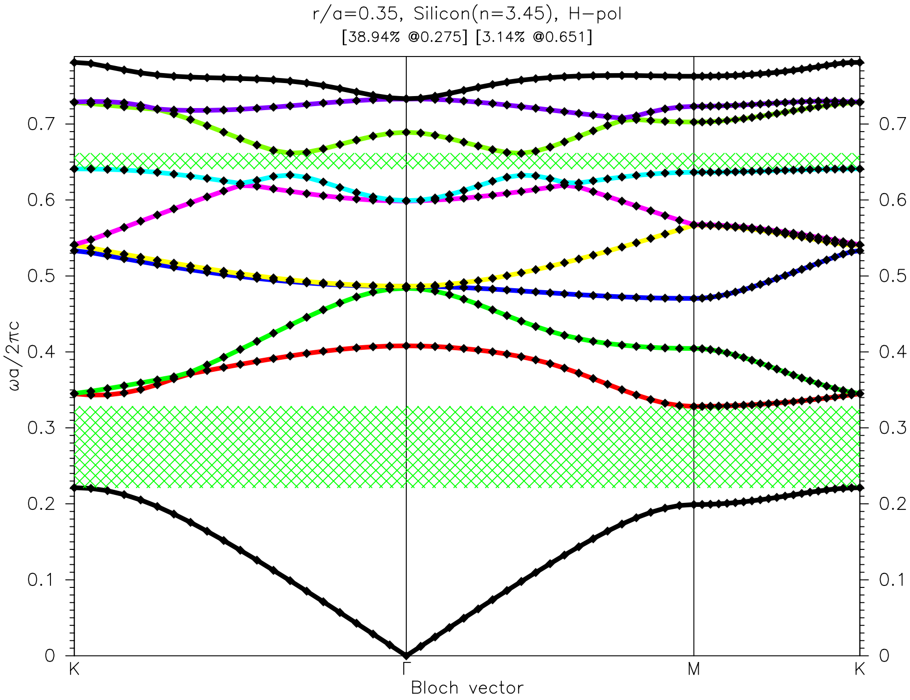

Figure 3.2: *Calculated band structure diagram of the sample crystal*

Generally, coming from the low frequency regime the dispersion curves, i.e. the first band starts, out linear from the center of the 1.BZ. Obviously the wavelengths are too long in this domain to probe the periodicity of the different dielectrics in the crystal. Propagating light then only experiences an averaged refractive index. In this linear regime the effective index of refraction is simply inverse proportional to the slope.

$$n_{eff} = \frac{k}{\omega_1(\boldsymbol{k})}c \tag{3.1}$$

More generally the slope of the band is related to the group velocity

$$v_{gr} = \nabla_{\boldsymbol{k}}\, \omega(\boldsymbol{k}). \tag{3.2}$$

Consequently, when going to higher frequencies the speed of light in the crystal can be drastically reduced. This is particularly true for bands bending towards a gap. Slow light near the band edge has already been observed experimentally [IVSL99].

The most prominent feature in the diagram 3.2 is of course the *band gap*. It is a region where two consecutive bands are so far apart in energy, that light in a certain wavelength range cannot couple to any band for any given direction, i.e. k-vector in the crystal. For these wavelengths the crystal is perfectly reflecting. No light is transmitted.

The band gap is generally characterized by the relative quantity of the *gap-midgap ratio* $\frac{\Delta\omega\omega_0}{\times}100$. The present example exhibits a gap of $\sim 40\%$ for the lowest band gap and $\sim 3\%$ for the second complete gap.

It is remarkable that light propagation in the gap is forbidden, although the materials constituting the crystal are transparent. This astonishing effect offers fantastic possibilities in optics such as the trapping of light and gives rise to new phenomena. The formation of band gaps strongly depends on the configuration of the crystal and is subject to discussion in section 3.5 on page 44.

If a gap does not extend throughout the complete BZ, but only exists for a particular direction then it is referred to as a *pseudo gap* or *stop band.*

Still going to higher frequencies past the band gap(s), the bands tend to flatten out. Although that would suggest that light propagation would slow down there, it is not at all clear what happens at frequencies corresponding to higher bands. Their combined effects get far too complicated to analyze and less interpretable. Additionally the convergence and therefore the accuracy of the numerical simulations is getting worse for higher band indices. Because the bands not only flatten out but also tend to be closer together, they eventually become indistinguishable and one reaches the classical geometrical optics domain for higher frequencies. However a clear limit cannot be stated.

3.2 Spatial Field Distribution

The electromagnetic fields $\boldsymbol{H}_{\boldsymbol{k}}(\boldsymbol{r})$ are the corresponding eigenfunctions in the master equation Eq. (2.8) to the eigenvalues $\omega_n(\boldsymbol{k})$, which are arranged in the band structure diagram. Since the differential operator in the master equation Eq. (2.8) can be shown to be hermitian, its eigenvalues are real and its eigenfunctions are harmonic modes. This implies that any two non-degenerate eigenfunctions are mutually orthogonal and own a distinct symmetry. Furthermore an electromagnetic variational principle holds, stating that the modes can minimize their electromagnetic energy by concentrating their displacement field $\boldsymbol{D}(\boldsymbol{r})$ in the high-ε regions [JMW95]. In analogy to quantum mechanics high-ε domains correspond to deeper energy potentials.

The phenomenon of 'repelling' bands can be illustrated by considering the spatial field distributions. Three factors play a role:

1. The electromagnetic modes, i.e. bands tend to concentrate their energy in the high-ε regions.
2. Modes have to be mutually orthogonal in space.
3. The fields have to be continuous across the interfaces of different dielectrics.

Therefore higher bands have to penetrate low index domains in order to stay orthogonal and continuous. Consequently two consecutive bands exhibit a distinct discontinuity ('jump') in energy if the electromagnetic power of their modes is mainly localized in regions with different dielectric constants. One often refers to *dielectric bands* (below the gap) and *air bands* (above the gap).

As an illustration, the displacement field for the first two bands at the K and M point is depicted in Fig. 3.3. The 1.band (dielectric band) has minimal energy by

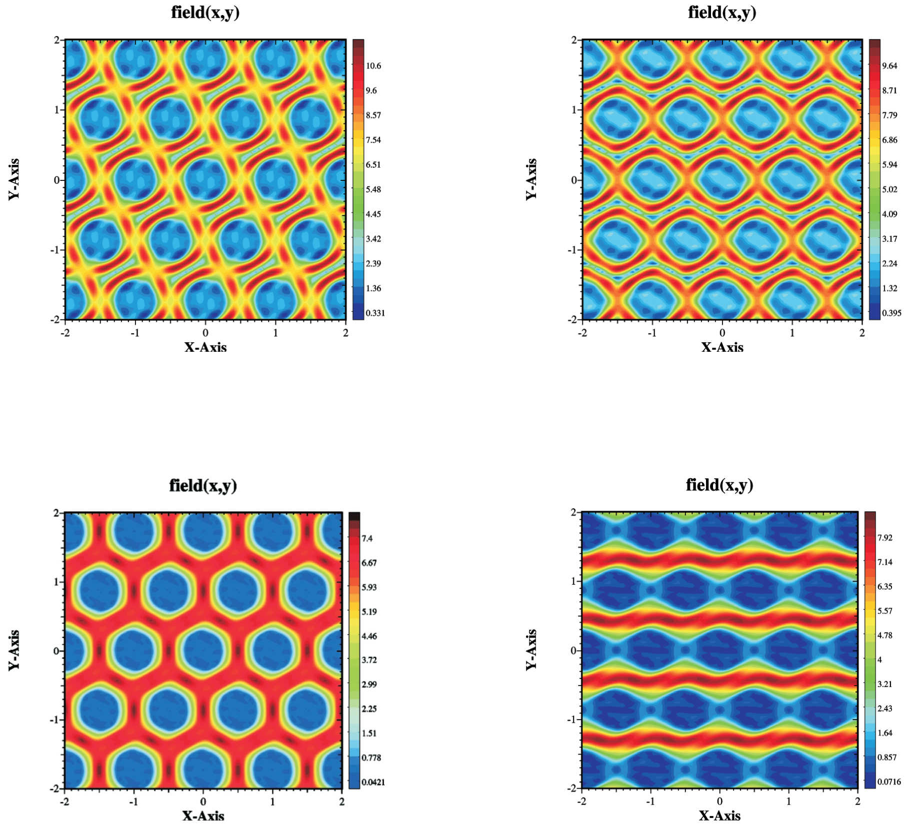

Figure 3.3: *Displacement field* $\mathbf{D}$ *in the* 1^{st} *(bottom) and* 2^{nd} *band (top) at the* K*-(left) and* M*-point (right). The corresponding normalized frequencies* $(\frac{\omega a}{2\pi c})$ *at the* K*-point are 0.22 and 0.345, at the* M*-point 0.2 and 0.33 respectively. Field distributions at the* K*-point for the* 2^{nd} *and* 3^{rd} *band are identical since the are degenerate.*

optimally concentrating the field in the high index material. The 2.band (air band) possesses a $\boldsymbol{D}$ field node in the high index backbone and therefore carries more energy.

3.3 Density of States

Once the dispersion relations $\omega_n(\boldsymbol{k})$ are known the photonic Density of States DOS can be calculated in the same manner as the electronic DOS (see 1.15-1.17 on page 20).

$$N(\omega) = \sum_n \int_{1.BZ} d^3k\, \delta(\omega - \omega_n(\boldsymbol{k})) \tag{3.3}$$

Alternatively, to better reveal the relationship to the dispersion curves or its slope:

$$N(\omega) = \sum_n \int_{S_n(\omega)} \frac{dS}{(2\pi)^3} \frac{1}{|\nabla\omega_n(\boldsymbol{k})|} \tag{3.4}$$

To evaluate the integral numerically it is necessary to discretize the first, i.e. the irreducible Brillouin Zone (IBZ) uniformly [JB99].

For the sample system the DOS was calculated and plotted on a normalized frequency scale again (see Fig. 3.4). The DOS is a measure for the number of allowed states in a certain differential energy interval and so a valuable tool to identify complete band gaps. Regions of zero DOS, where no allowed states exist are full band gaps throughout the BZ. Peaks in the DOS curve represent van Hove singularities and correspond to a vanishing gradient of the dispersion. DOS considerations are of particular interest in quantum optical calculations [BVJS00].

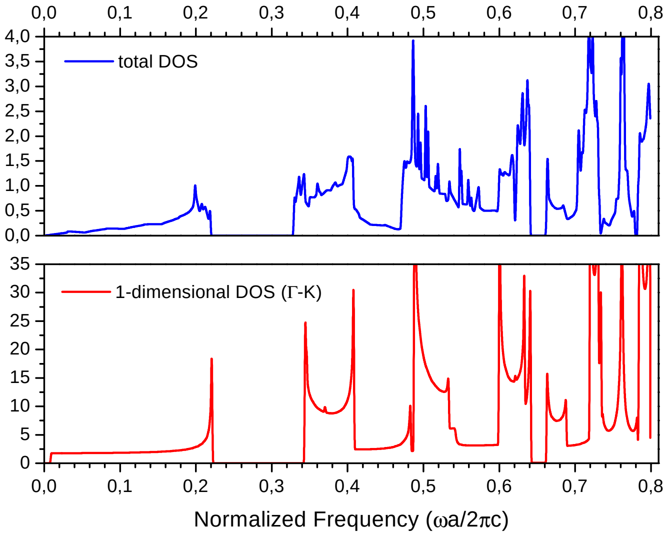

Figure 3.4: *Calculated total 2-dimensional photonic Density of States (top) and 1-dimensional DOS in $\Gamma - K$ direction*

An entirely linear $\omega_n(\boldsymbol{k})$ (free space, i.e. vacuum) would result in a photonic DOS curve proportional to ω^2 as opposed to a $E^{3/2}$ ∼curve for free electrons. That is because the shape of the DOS depends exclusively on the dispersion curve and the dimension of the integral. This is also demonstrated through a 1-dimensional DOS by integrating only over a specific crystal axis. In this case a constant DOS would result for a homogeneous system. Since our sample system is far from homogeneous, clear gaps arise. The 1-dimensional DOS was calculated in $\Gamma - K$ direction. In this fashion, identification of pseudo gaps is also possible. Nevertheless the 1-dimensional DOS ought not to be confused with a transmission curve (compare with Fig. 3.5).

The photonic DOS is also a measure for the quality of coupling between energetic systems, like excited atoms or radiating dipoles [BVJS00] and the electromagnetic vacuum modes. An extension to the total DOS would be a local DOS

$$N_{\text{local}}(\omega, \boldsymbol{r}) = \sum_n \int_{1.BZ} d^3k \, |\boldsymbol{E}_{n,\boldsymbol{k}}(\boldsymbol{r})|^2 \, \delta(\omega - \omega_{n\boldsymbol{k}}), \tag{3.5}$$

which expresses local coupling of an imaginary atom inside a photonic crystal with the Bloch modes. Consequently their spatial intensity distribution has to be taken into account.

3.4 Transmission and Reflection

Band structure diagrams and DOS deliver a lot of information and give deep insight to the optical properties of the crystal. Nevertheless it is often desirable to characterize transmission and reflection properties, especially when interpreting experimental results. Only phase-sensitive experiments like Terahertz Time Domain Spectroscopy THz-TDS [WLH98] or coherent microwave spectroscopy [RAM$^+$93] can directly probe the dispersion relations.

With the Transfer-Matrix method program (see section 2.4.2) we are able to calculate actual transmission (T) and reflection (R) coefficients for specific wavelengths. The results for the system under study ($\Gamma - K$ direction) are shown in Fig. 3.5. Transmission and reflection curves are plotted on a normalized frequency scale again. The accuracy for higher frequencies ($\frac{\omega a}{2\pi c} \gtrsim 1$) is doubtful as with the other methods.

Please notice that transmission and reflection curve do not necessarily have to be complementary as in this case. In metallic systems (metallo-dielectric photonic crystals) for instance absorption plays a major role and $R + T < 1$.

Furthermore the computer program permits to follow the evolution of the curves for an arbitrary number of unit cell layers of a crystal. This is particularly useful when the number of layers is known exactly. In Fig. 3.6 the transmission spectra for 1, 2, 4 and 8 layers of our sample structure are plotted on a logarithmic scale. One layer consists of two rows of cylinders. Please notice that the number of layers coincides with the number of oscillations below the gap. This effect corresponds to Fabry-Perot fringes as eminent in 1-dimensional systems, like Bragg stacks or dielectric mirrors.

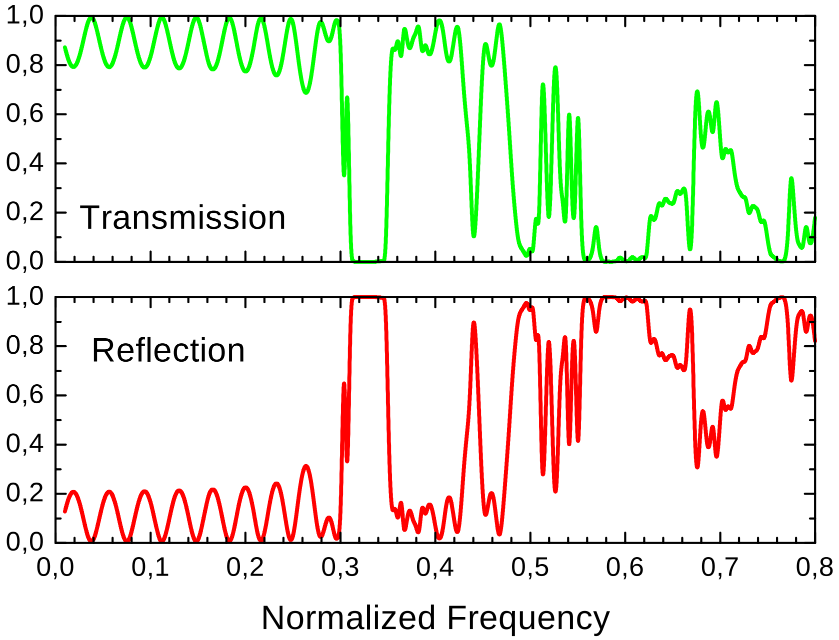

Figure 3.5: *Transmission and reflection spectra in $\Gamma - K$ direction for the sample crystal*

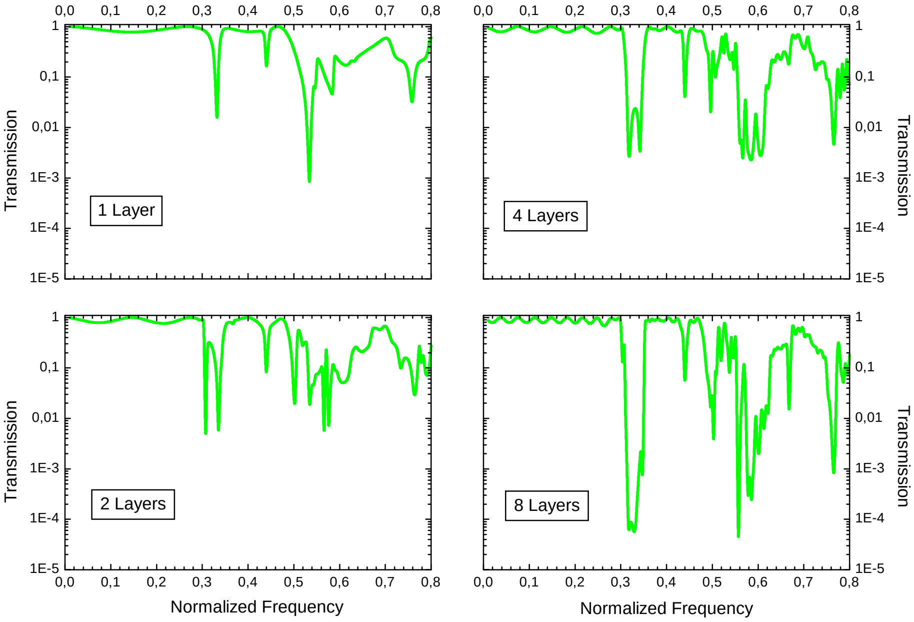

Figure 3.6: *Evolution of the gaps with increasing number of layers*

3.5 Design and Optimization Criteria

Some of the main interest in the field of photonic crystals surely focuses on the possibility to create Photonic Band Gap PBG materials. But not necessarily every photonic crystal exhibits a complete gap. So it is advisable to look at the range of parameters free to modify in order to design photonic crystals. Furthermore it will be helpful to develop a certain feeling for the implications of those variables when optimizing a band gap. A glimpse on existing state of the art designs and unconventional photonic crystals will conclude this section.

3.5.1 Polarizations

Whenever there is a distinct special axis in the crystal, as in our 2-dimensional crystal the z-axis for instance, it is possible to de-couple the electromagnetic fields. Based on this axis they can be labeled *transverse magnetic TM*, or sometimes referred to as *E-polarization*, and *transverse electric TE (H-polarization)*. Consequently, in the quest for a complete gap, overlapping band gaps for both polarization states have to be achieved.

As a rule of thumb, it turns out that TE band gaps are favored in a lattice with connected high index backbone, e.g. columns in a dielectric. TM gaps on the other hand, prefer lattices with isolated high index regions, e.g. ordered dielectric rods. Recalling the discussion about spatial electromagnetic field distribution, especially the formation of air and dielectric bands in section 3.2 on page 40 sheds light on this phenomenon. It can be attributed to the fact that only for one polarization at a time it is possible to localize its electromagnetic energy of consecutive modes in the preferred high-ε regions. Whereas the 'air band' of the other polarization state has to penetrate (continuity of the fields) low-ε domains, which results in increased energy.

3.5.2 Dielectric Contrast

A straightforward parameter to consider is the index of refraction. In order to increase a band gap it is of foremost importance to maximize the ratio of the refractive indices $\varepsilon_{high}/\varepsilon_{low}$.

This can only be achieved by selecting proper materials. The dependence of the gap size on this *dielectric contrast* is strictly monotonous, even up to extremely high dielectric constants (like $\varepsilon = 300$ for Rutil in the microwave regime). Recalling the dielectric constant as the analogon to the quantum mechanical potential enlightens this fact. Larger dielectric contrasts are equivalent to deeper potentials which result in stronger splitting of the bands in the Nearly Free Electron or Photon picture (see section 1.1.5 and 2.3 on page 19 and 31 respectively). From a different point of view larger discontinuities of refractive index result in stronger scattering of light at the respective interfaces. This is also the reason why discontinuities in dielectric constant, i.e. jumps are preferable over smoothly varying index functions, for instance sinusoidal ones.

Moreover when increasing the index contrast not only does the size of the gap increase but also its position shifts towards lower frequencies (see Fig. 3.13). Because

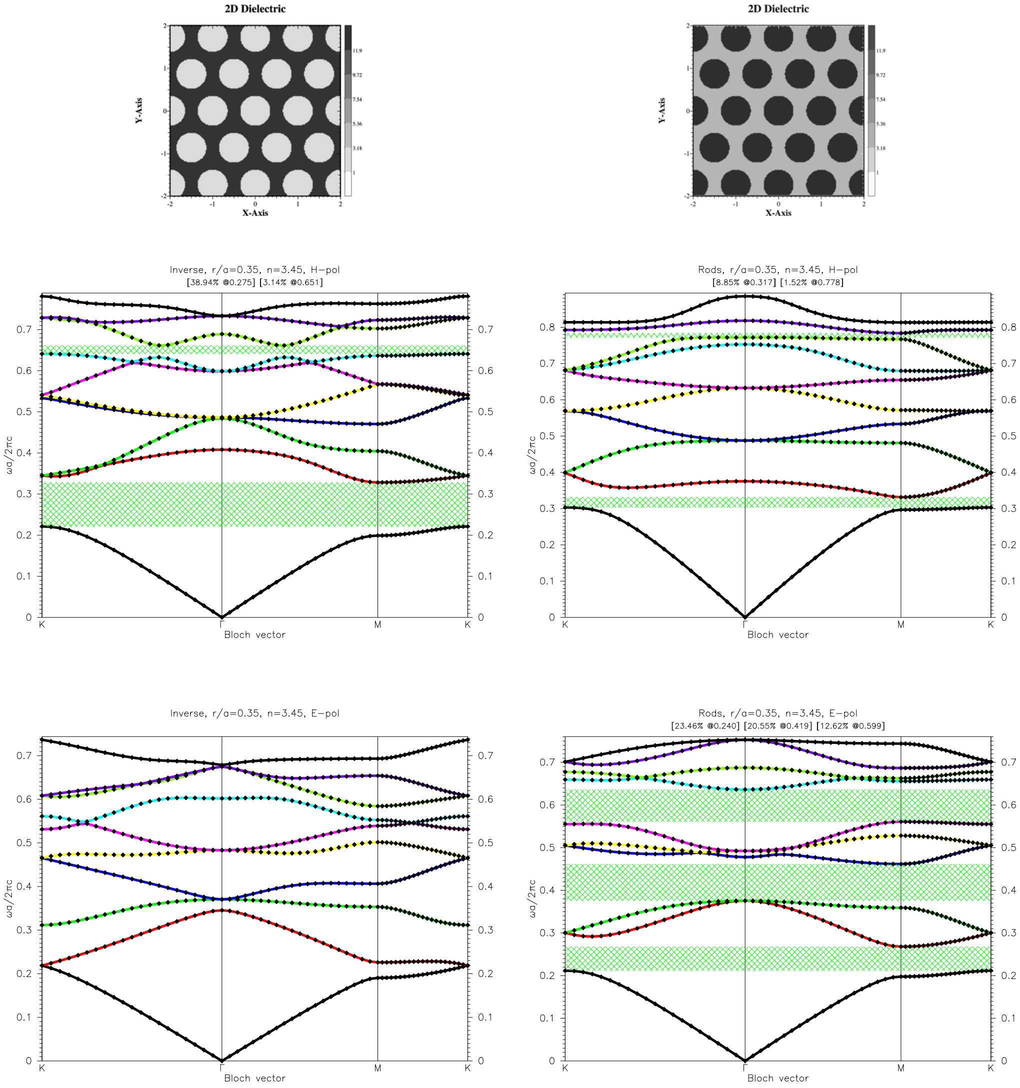

Figure 3.7: *Air columns in high index (n=3.45) backbone (left) and ordered high index rods in air (right): TE (H-polarization) (center) vs. TM (E-polarization) (bottom)*

higher dielectric constants mean higher effective index flattening the bands (see Rutil in Fig. 3.8). This can be seen in the long wavelength limit (1^{st} band):

$$\frac{|\boldsymbol{k}|}{\omega_1(\boldsymbol{k})} = \frac{c}{n_{eff}} \tag{3.6}$$

Usually a threshold for the minimum dielectric contrast required to open up a complete gap is stated for a given crystal structure. (e.g. $\varepsilon_{th} = \varepsilon_{high}/\varepsilon_{low} \geq 1.9$ for our sample crystal)

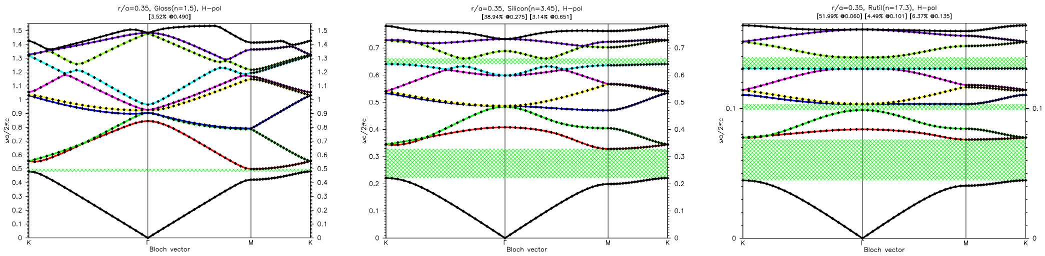

Figure 3.8: *The evolution of the band gap with increasing dielectric constant: On the left Glass* ($\varepsilon = 2.25$)*, in the center Silicon* ($\varepsilon = 11.9$) *and on the right Rutil* ($\varepsilon = 300$). The lattice is the same as discussed above

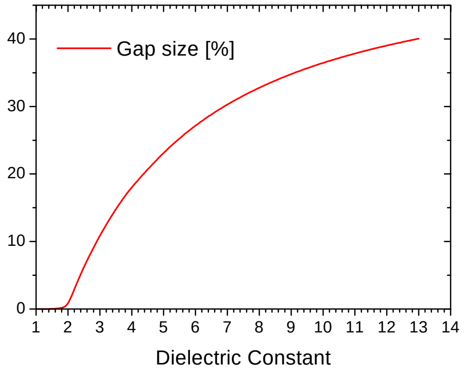

Figure 3.9: *The dependence of the gap size* ($\frac{\Delta\omega\omega_0}{\times}100$) *on the variation of dielectric constant for the sample crystal (with air filling)*

3.5.3 Crystal Structure

Contrary to the dielectric contrast the crystal structure is a more complex parameter to analyze.

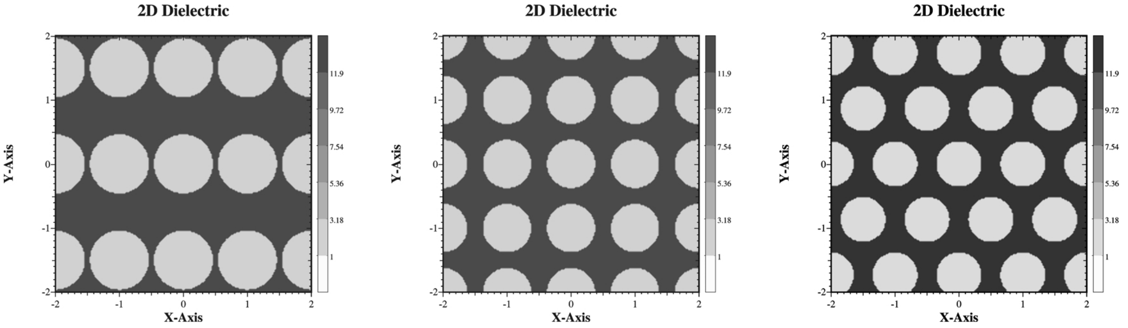

Figure 3.10: *Comparison of different lattices (equal filling fraction, same dielectric contrast and polarization): On the left a rectangular lattice, a square in the center and a triangular lattice (sample system) on the right*

First of all the underlying point lattice offers some degree of freedom. A point lattice with a most sphere-like (3D) or disc-like (2D) 1.BZ has the best chance to exhibit a complete gap throughout the BZ. The reason for this is that the lengths of different high symmetry axes in the BZ are approximately the same. Then, thinking in a Nearly Free Photon picture again, the energy differences of one band at the different respective edges of the BZ are less pronounced. Consequently it is easier to create a band gap by lifting the degeneracies through perturbations, i.e. increasing the dielectric contrast.

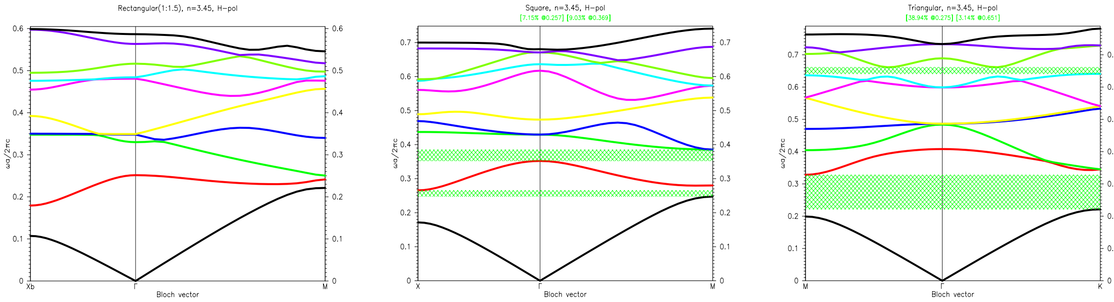

Figure 3.11: *The band structures for the different lattices in Fig. 3.10: Rectangular lattice (left), Square lattice (center) and Triangular lattice (right)*

Nevertheless some of the degeneracies cannot be lifted since they are symmetry induced (e.g. the W-point in fcc lattice [LL90]). In this case the proper choice of the basis element (motif) can reduce or break the overall symmetry of the crystal structure. Frequently employed geometric shapes like spheres or discs could be replaced by motifs with less symmetry to break the overall symmetry. A typical example is the diamond configuration where two spheres serve as the motif in an fcc lattice type. One sphere is located at (0,0,0) the other displaced by $\frac{1}{4}(\boldsymbol{a}_1 + \boldsymbol{a}_2 + \boldsymbol{a}_3)$ in the unit cell. This configuration exhibits the largest complete 3-dimensional band gaps.

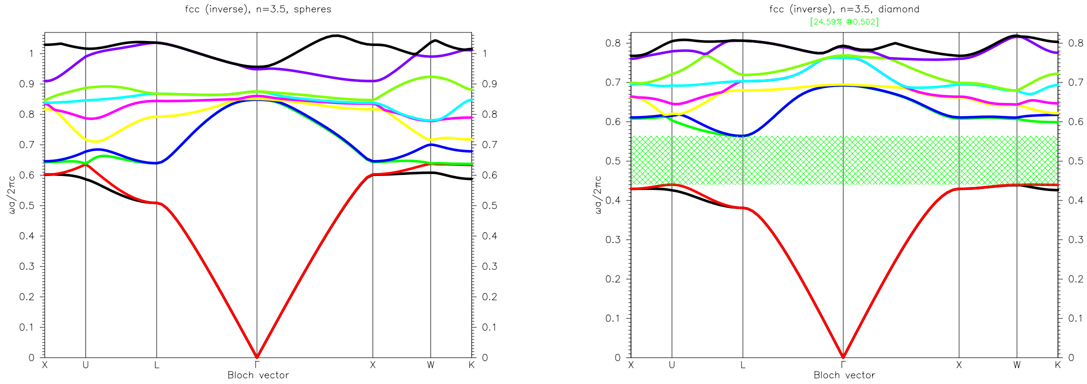

Figure 3.12: *An fcc lattice consisting of 1 sphere (left) and two separated spheres (right) as a motif. The latter is a diamond configuration.*

3.5.4 Filling Fraction

The *filling fraction* of the crystal is a most important parameter which has to be optimized carefully. Usually this has to be done numerically for every single configuration. The dependence of the gap-size on the filling fraction is generally a bell-shaped curve with a distinct maximum. Sometimes this dependence is expressed in terms of the quantity r/a, where r is a parameter characterizing the motif (e.g. the radius for cylinders or spheres) and a the lattice constant. Of course the relationship between r/a and the filling fraction is different for every point lattice but easy to calculate through geometrical considerations (e.g. for a square lattice $f = (\frac{r}{a})^2\pi$ or for a triangular lattice $f = \frac{2}{\sqrt{3}}(\frac{r}{a})^2\pi$).

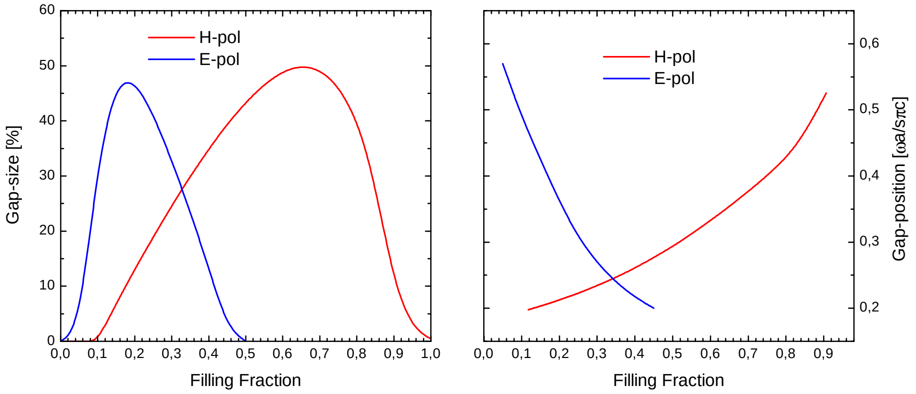

Figure 3.13: *The relative size of the band gap in our sample crystal depending on the filling fraction with air (left). The position of the gap with varying filling fraction (right)*

The dependence of the band gap in our sample system on the filling fraction is plotted in Fig. 3.13. This diagram reveals that a maximal band gap of 50% could be obtained at an air filling fraction of $f \approx 0.66$. This corresponds to $r/a \approx 0.43$ in our configuration.

It is clear that in the limits of very low and very high filling factors the band gap vanishes since the structure approaches homogeneity. The asymmetric shape of the curve can be attributed to the fact that the air columns touch at $r/a = 0.5$ ($\leftrightarrow f \approx 0.9$) and yield isolated domains of high index material. This is a configuration which does not favor TE gaps (see subsection 3.5.1). Furthermore the position of the band gap shifts with varying filling factors since that changes the effective index.

Fig. 3.14 illustrates how the optimal filling fraction shifts with increasing dielectric contrast. This means that crystals consisting of materials with very high refractive index should actually consist mostly of air.

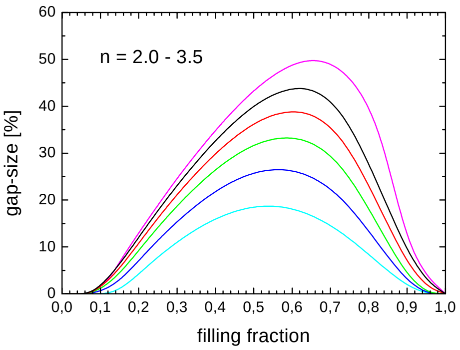

Figure 3.14: *Dependence of the optimal filling ratio on the dielectric contrast. Curves calculated for the sample crystal.*

3.5.5 State of the Art

With this kind of knowledge it is possible to design photonic crystals in 2- and 3-dimensional space with optimized band gaps or other desired features. Limitations of course apply to fabrication techniques and material properties.

State of the art 3-dimensional crystals are inverted opals. They consist of air spheres in a backbone of Silicon (Si: n=3.45), arranged in a diamond lattice. With such sophisticated crystals the first complete band-gap at optical telecommunication wavelength (1.5 μm) was achieved [BCG$^+$00].

Additional material properties can be exploited to further manipulate and extend the features of photonic crystals. For instance *active media* can be incorporated in the dielectrics to study emission and lasing properties [BVJS00]. *Conductive materials* are used to create *metallo-dielectric* photonic crystals [FVJ96]. Another highly interesting idea is the infiltration of photonic crystals with *liquid crystals*. Liquid crystals have mnematic properties and are sensitive to external electric or magnetic fields. They align themselves in the presence of those fields and thereby change their optical properties, i.e. refractive index in certain directions. With such a combination of liquid and photonic crystals it is in principle possible to build *tunable photonic band gaps* [BJ99] [Yab99].

Chapter 4

Ultra-Refractive Effects in Photonic Crystals

The previous chapters serve as an introductory basis and overview of the field of photonic crystals. I now want to present the work I conducted while spending 6 month in the research group of Prof. Sajeev John at the University of Toronto, Canada from January 2000 to June 2000. This invaluable research study was made possible through and funded by a Government of Canada Award.

My research topic in Canada was *"What happens at non-normal incidence of non-monochromatic light on a photonic crystal ?"*. It turns out that new phenomena unprecedented in conventional optics arise in this case.These phenomena are often referred to as *the superprism effect* or more generally *ultra-refractive effects*.

In this chapter I will briefly outline the evolution of this specific field and introduce a straightforward theoretical numerical approach. I will apply this approach, in conjunction with our PWEM program presented in section 2.1, to review existing work. Finally refraction properties of relevant photonic crystals in designated experiments are predicted with these methods.

4.1 Introductory Theory

In classical optics we are familiar with the effects of coupling light into a homogeneous, isotropic dielectric (e.g. with $n = 2$). The angular dependence of refraction is stated by *Snell's law* Eq. (1.28) and can be interpreted with *Fermat's principle.* Furthermore dispersion of light results if the material has a wavelength-dependent index of refraction $n(\omega)$. In case of an anisotropic material (e.g. birefringent crystal) the relations can also be relatively easily be stated [BW75].

The key question is how these laws apply to photonic crystals. There have been several approaches to this problem, basically distinguished as a phase-velocity picture and a group-velocity approach. I will first present the more intuitive phase-velocity picture. Then I will discuss some field plots generated by diffraction grating methods which do not rely on either picture. Finally the more general group-velocity approach will be described along with a procedure how to implement it. The latter strategy was employed in my own calculations.

4.1.1 Phase Velocity Approach

The people who came up with the phase-velocity approach (Dowling and Bowden [DB94]) were motivated by discussions on the merit of ultra-high refractive indices with regard to lasing without inversion, resolving power of optical microscopes and laser acceleration of electrons. In fact the resolving power only depends on the ratio of n_0/n and therefore the authors strove to find ultra-low indices in order to increase this ratio.

They initially assume a 1-dimensional system. The dispersion relations $\omega(k)$, or $k(\omega)$ can be calculated analytically in this case. They are shown in Fig. 4.1.

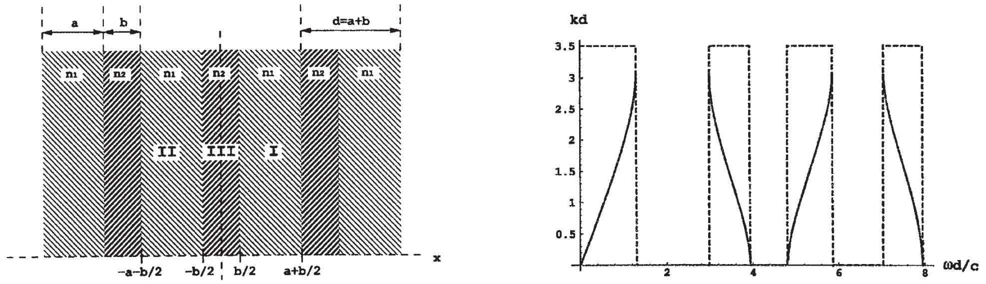

Figure 4.1: *Dispersion relations $k(\omega)$ (right) for a 1-dimensional model system (left). The lattice constant here is given by d [DB94].*

Since the index of refraction n is given by $n = \frac{c}{v_{phase}}$ and the phase velocity simply by $v_{phase} = \frac{\omega}{k}$, the actual refractive index can be obtained through $n(\omega) = \frac{kc}{\omega}$. It is plotted in Fig. 4.2 and shows anomalous behaviour. For instance it drops below 1 in the higher bands and even tends to zero at the band edges. This situation corresponds to a phase velocity $\rightarrow \infty$ (!).

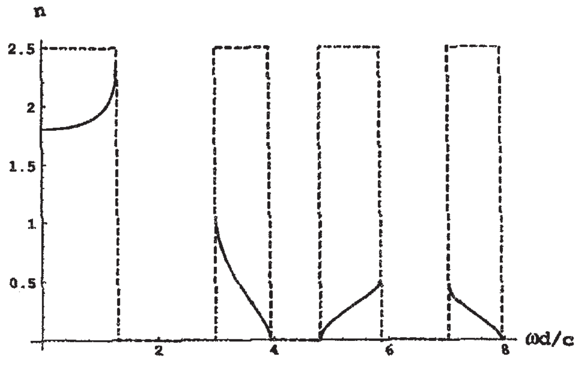

Figure 4.2: *Extracted effective index of refraction [DB94]*

In my opinion the idea of an effective index defined by the phase velocity can only properly be applied in the long wavelength limit (1^{st} band), because the physical behaviour of the light is governed by the group velocity. An extension of this 1-dimensional model to 2- and 3-dimensional space requires more complex reflections on the propagation direction of light. This can be better accounted for in the group velocity picture.

Furthermore this picture raises the question if superluminous phenomena are present in such a system. It has already been confirmed experimentally (with autocorrelation techniques) that indeed the phase velocity is increased dramatically way beyond the speed of light. This implies that light is basically tunneling through this barrier. But on the other hand this poses no violation to Einstein's theory of relativity. Because first of all only a marginal amount of light is transmitted, since this all happens very close to the band gap. Secondly these effects are only possible in an extremely narrow wavelength range. This inhibits the transmission of information, because such necessarily implies a certain band width.

The idea of an anomalous effective index in photonic crystals, exhibiting unusual properties was picked up by Lin et al. [LHWJ96]. These authors tried to make use of this anomalous refractive index and built a highly dispersive PBG prism in the microwave regime. It consisted of dielectric rods arranged in a triangular lattice and was shaped in a equilateral prism (see Fig. 4.3). They measured incident and refracted angles for different wavelengths below the band gap. Then they extracted an empirical index of refraction $n(\lambda)$ by applying the standard prism formula Eq. (4.1) to the deflection angle $\delta(\lambda)$.

$$\delta = \theta_i + \arcsin\left(\sin\alpha\,\sqrt{n^2 - \sin^2\theta_i} - \sin\theta_i\,\cos\alpha\right) - \alpha. \tag{4.1}$$

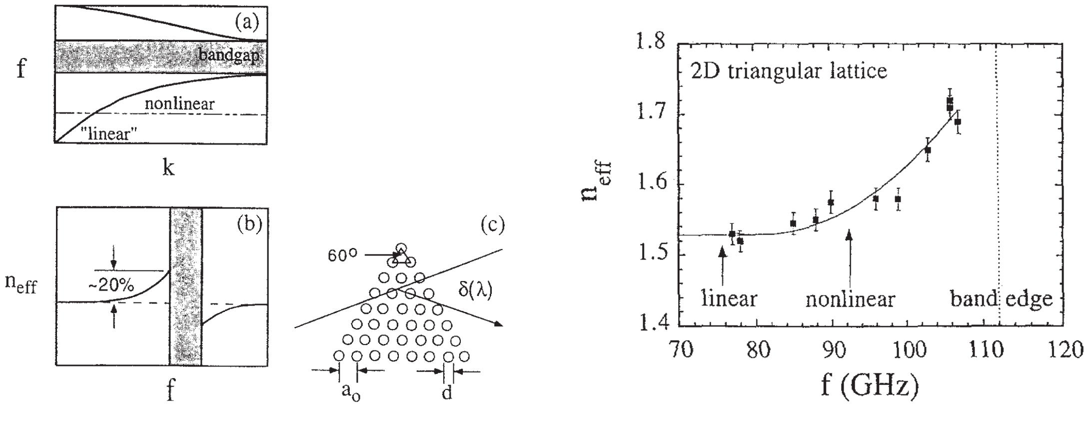

Figure 4.3: *Experiment and results by [LHWJ96]*

Their results show a clear increase of the refractive index ($\sim$ 20%) when approaching the band gap. Unfortunately their work is of pure experimental origin and no attempt was made to relate these results to any quantitative theoretical analysis. Nevertheless the first experimental verification of a highly refractive material was established. It offers high sensitivity to incident wavelengths and angles. Therefore it would be well suited for instance, to increase the bandwidth and reduce the size of optical components used for wavelength-division multiplexing-demultiplexing (WDM).

4.1.2 Field Plots

Investigations based on Diffraction or Scattering methods as performed in the group of Maystre [ETM99], do not rely on either a group velocity or phase velocity picture. With these methods Maxwell's equations are rigorously evaluated numerically for finite structures. This approach yields field maps of a monochromatic wave interacting with, i.e. diffracted by, a given photonic crystal. The figures below show a gaussian beam hitting a slab of photonic crystal from atop and incident, reflected and transmitted fields are simulated.

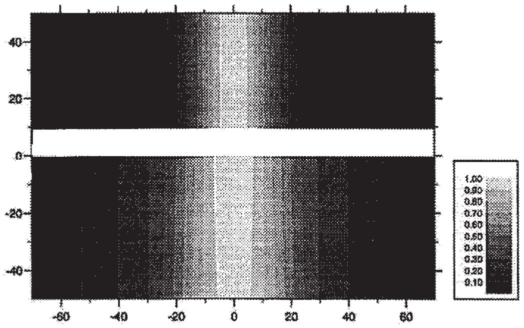

Figure 4.4: *Widening of the beam:* $\lambda = 2.5447$

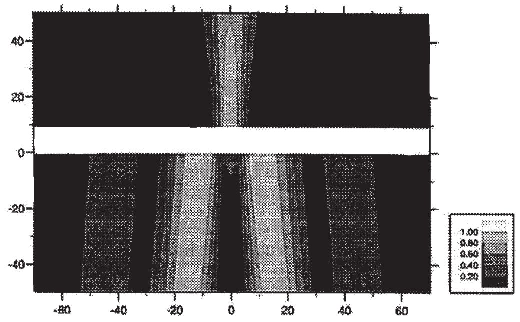

Figure 4.5: *Splitting of the beam:* $\lambda = 2.543$

These results clearly show exceptional diffraction and refraction effects. Under normal incidence [ETM99] widening (Fig. 4.4) and splitting occurs (Fig. 4.5) for only marginally altered wavelengths. The splitting corresponds to spatial Fabry-Perot fringes.

At non-normal incidence ultra-refraction (Fig. 4.6) and negative refraction (Fig. 4.7) is predicted by Gralak et al. [GET00]. Ultra-refraction, where the angle of refraction is greater than the angle of incidence ($\theta_i < \theta_r$), implies that indeed an effective index of refraction less than one ($n_{eff} < 1$) exists for this particular wavelength. Gralak et al. [GET00] extended this analysis to proposed micro-optical components specifically designed to exploit these effects, like micro-lenses and micro-prisms (Fig. 4.8, 4.9).

The beautiful results obtained with Diffraction or Scattering methods confirm that extraordinary refraction properties exist when coupling light into photonic crystals. Unfortunately the field patterns need to be computed for every single configuration (angle, wavelength) separately. Therefore it is difficult with this method to show intrinsic coherencies and provide deeper insight to the underlying causes of the phenomena.

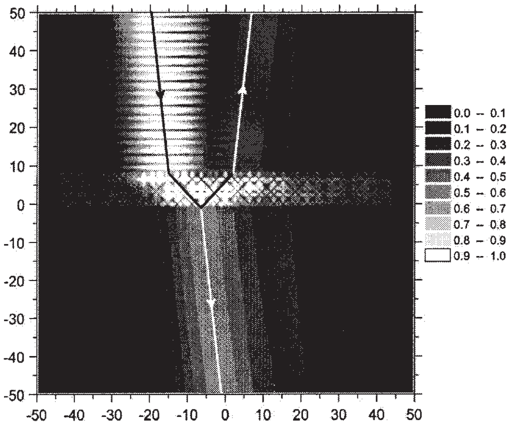

Figure 4.6: *Ultra-refraction*

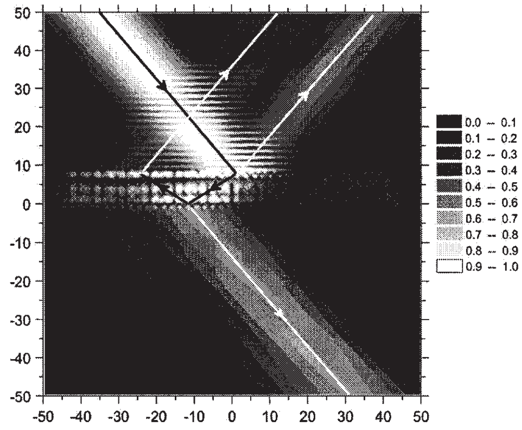

Figure 4.7: *Negative refraction*

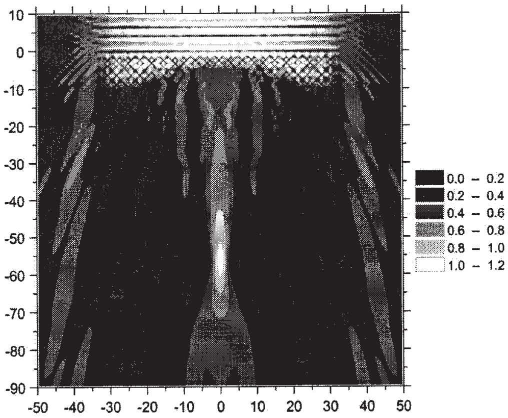

Figure 4.8: *Micro-lens*

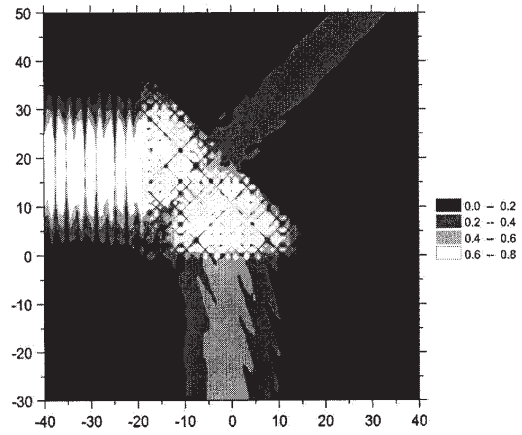

Figure 4.9: *Micro-prism*

4.1.3 Group Velocity Approach

The group velocity approach provides a picture better suited to illustrate the reasons for the remarkable refraction properties of photonic crystals. It is based on two cornerstones:

1. The propagation direction of light inside the crystal is given by the group velocity.
2. The basic boundary conditions in electromagnetic theory (→ Fresnel equations) extend to photonic crystals.

The first theoretical predictions and experiments for refraction properties of photonic crystals based on a group velocity argument were done by Kosaka et al. [KKT$^+$98, KKT$^+$99a, KKT$^+$99b].

Gradient The work by Kosaka et al. picks up a theoretical treatment of Ohtaka [OT96a, OT96b, OT96c, OUT96] who proves that the *energy flux* is indeed in the direction of the *group velocity*, i.e. the gradient of the dispersion curve:

$$\nabla\omega(\boldsymbol{k}) = \boldsymbol{v}_{group} = \boldsymbol{v}_{energy} = \frac{\int_{cell}\frac{c}{4\pi}\left[\boldsymbol{E}(\boldsymbol{r})\times\boldsymbol{H}(\boldsymbol{r})\right]d\boldsymbol{r}}{\int_{cell}\frac{1}{8\pi}\left|\boldsymbol{H}(\boldsymbol{r})\right|^2 d\boldsymbol{r}}, \tag{4.2}$$

where the numerator is basically the integral of the Poynting vector and the denominator the integral of the energy density.

This implies that in order to predict the propagation direction of light inside the crystal requires to have full knowledge of the complete topology of the dispersion curves. Since the gradient is a derivative, also the energy values $\omega[\boldsymbol{k})$ of a certain wave-vector $\boldsymbol{k}$ need to be known in a 3-dimensional surrounding. It is generally not sufficient to just look at a 1-dimensional cut through the band structure, as in a phase velocity picture, since the gradient of a certain point does not necessarily fall into the plane of the cut. Heuristically the gradient points towards the steepest slopes of the function. For instance in a 2-dimensional topology (e.g. alpine landscape) that would be the direction of the greatest slope, i.e. the inverse direction where water would flow.

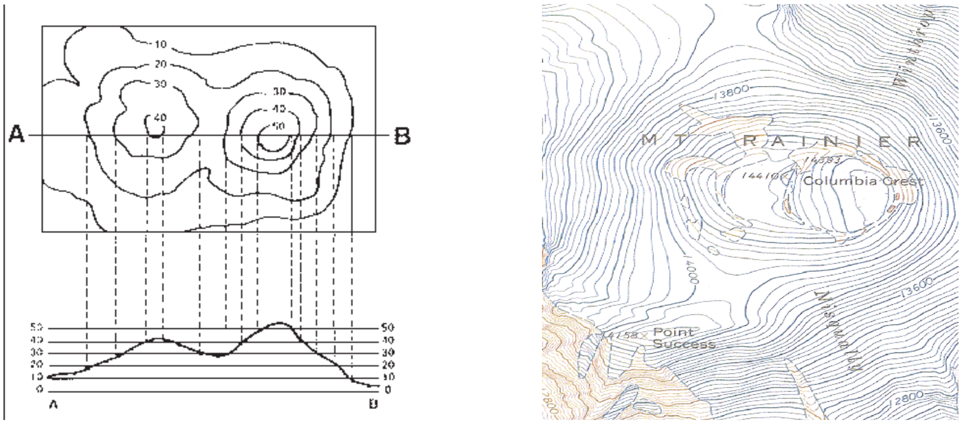

Figure 4.10: *Interpretation of Contour lines and a real life example*

An educational way to find the gradient is by drawing the contour lines of the topology and subsequently constructing the normals on them, bearing in mind that its direction is defined as upward. This method using the contour lines is in many cases easier to implement and usually more intuitive (just think alpine mountain ranges maps).

It is clear now how to find the propagation direction inside the crystal. But in order to do so certain *constraints* apply. Most importantly the correlation between the propagating modes inside (Bloch modes) and outside (plane wave) the crystal have to be determined. This defines the boundary condition.

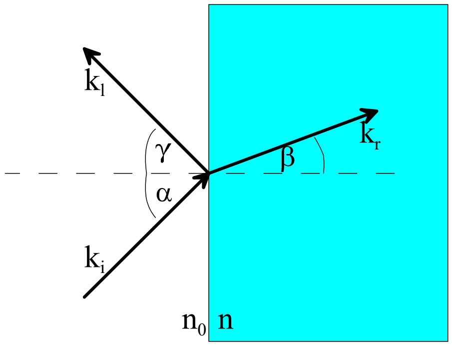

Figure 4.11: *Incident, refracted and reflected beam*

Boundary Condition Let us recall the classical boundary condition in electromagnetic theory at an air-dielectric interface. It is deduced here and leads to the well known Snell's law for homogeneous materials. We consider Maxwell's equation in air (n_0) at the boundary to a dielectric material (n). An incoming beam splits into a refracted (r) and a reflected (l) beam.

$$\boldsymbol{E}_i(\boldsymbol{r},t) = \boldsymbol{E}_i^0\, e^{i\boldsymbol{k}_i\boldsymbol{r}-i\omega t} \tag{4.3}$$

$$\boldsymbol{E}_r(\boldsymbol{r},t) = \boldsymbol{E}_r^0\, e^{i\boldsymbol{k}_r\boldsymbol{r}-i\omega t} \tag{4.4}$$

$$\boldsymbol{E}_l(\boldsymbol{r},t) = \boldsymbol{E}_l^0\, e^{i\boldsymbol{k}_l\boldsymbol{r}-i\omega t} \tag{4.5}$$

where

$$|\boldsymbol{k}_i| = k_i = \frac{\omega}{c} n_0 = k_r = |\boldsymbol{k}_r| \quad , \quad |\boldsymbol{k}_l| = k_l = \frac{\omega}{c} n \tag{4.6}$$

and $\boldsymbol{k}_i, \boldsymbol{k}_r, \boldsymbol{k}_l$ denote the incident, refracted and reflected wave vector, respectively.

The conditions satisfied by the $\boldsymbol{E}$ and $\boldsymbol{H}$ field are simply deducible from Maxwell's equations (Fresnel equations). They must hold in both media and demand the parallel component of $\boldsymbol{E}$ and the normal component of $\boldsymbol{H}$ to be continuous across the interface. Furthermore it is necessary to satisfy a *phase-matching* condition at the boundary for all 3 wave vectors:

$$(\boldsymbol{k}_i \cdot \boldsymbol{r})_{z=0} = (\boldsymbol{k}_r \cdot \boldsymbol{r})_{z=0} = (\boldsymbol{k}_l \cdot \boldsymbol{r})_{z=0} \tag{4.7}$$

Generally this just states the continuity of the parallel component of the wave vectors $\boldsymbol{k}_{||}$ across the interface ! This condition can be expressed alternatively in terms of angles to the normal on the boundary plane for incident (α), refracted (β) and reflected (γ) beam.

$$k_i\, sin(\alpha) = k_r\, sin(\beta) = k_l\, sin(\gamma) \tag{4.8}$$

In conjunction with Eq. (4.6) this simply recovers Snell's law:

$$n_0\, sin(\alpha) = n_0\, sin(\gamma) = n\, sin(\beta) \tag{4.9}$$

But whether this simple condition straightforwardly extends to the photonic crystal case is still a matter of discussion. Nevertheless it is the best available approximation so far.

4.1.4 A Procedure

Having elaborated the relevant building blocks for predicting refraction properties, namely the topology of the dispersion relation (full k-space) and the boundary condition ($\boldsymbol{k}_{||} = constant$), it is now possible to show how this can be implemented to investigate ultra-refractive phenomena. I want to present a procedure for extracting the relationship between the angle of refraction and the angle of incidence. For simplicity this shall be illustrated for the simple case of a homogeneous, isotropic medium ($n = 2$) and will recover the well known refraction properties by means of this 'detour'.

1. Calculate the dispersion relations in full k-space.
2. Draw the topological map with contour lines.
3. Extract the contour line of interest, i.e. cut the surface at a specific height ($\propto$ wavelength).
4. Construct the parallel component of the incident wave vector: $|\boldsymbol{k}| = \frac{2\pi}{\lambda}$ and $k_{||} = |\boldsymbol{k}|\, sin(\alpha)$.
5. Intersect the $\boldsymbol{k}_{||}$-construction line with the contour line.
6. Take the normal of the contour line at the intersection point.
7. Determine the direction of the slope (gradient points upwards).
8. Scanning the incident angle and repeatedly applying this procedure yields the full angle-angle relationship.

Attention needs to be drawn to the following. The resulting directions can be somewhat ambiguous since the $\boldsymbol{k}_{||}$-construction line actually intersects twice with a given contour line. In the homogeneous, isotropic case this does not appear to be a problem. The direction is intuitively determined. Nevertheless in the photonic crystal case this can pose a complex problem which has to be overcome by carefully picking the physically right direction. This ambiguity can be explained by the following argument: Owing to the symmetry in Maxwell's equations the direction with $-k_{\perp}$ is also a solution if the

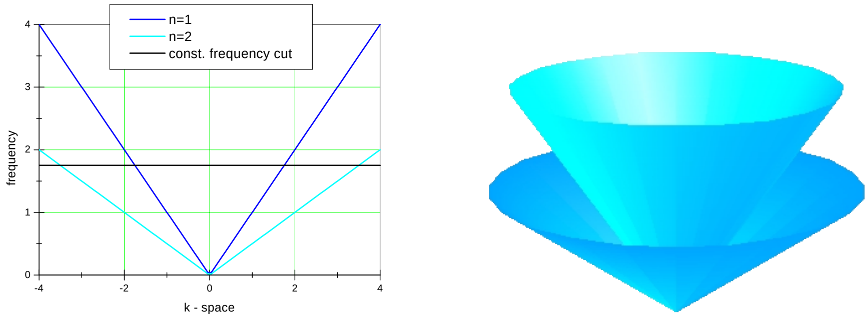

(a) Dispersion Relations

(b) Dispersion Surfaces

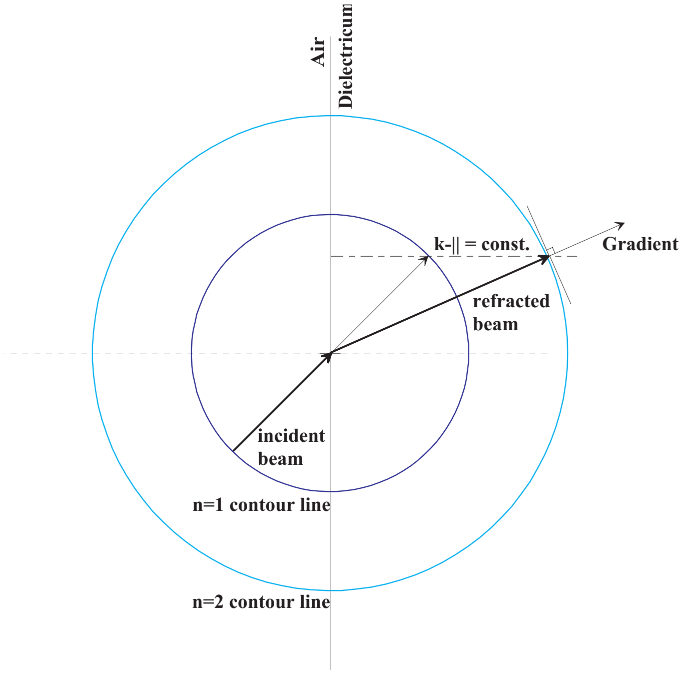

(c) $k_{||}$ - Construction

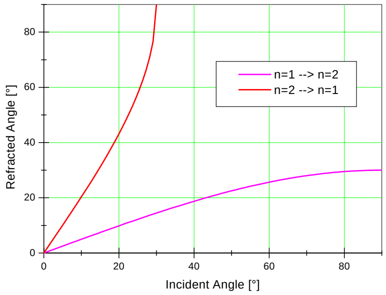

(d) Resulting Refraction Curves

Figure 4.12:

$k_\perp$-direction is one. This is the reason for the non-existence of a direct optical diode. (See appendix C for a case study on a 'brilliant' idea ...)

As can be seen in Fig. 4.12, applying the procedure to a homogeneous dielectric medium the classical refraction relation $\beta = arcsin(\frac{n_0}{n}\, sin\alpha)$ is regained. The inverse case, light traveling from a high index material to a low index material, yields the steep curve depicted in Fig. 4.12(d). Here the effect of total internal reflection can be nicely seen. Since there are no corresponding refracted angles for incident angles $\alpha \geq 30°$ $(n = 2)$, no propagation is supported into the vacuum. All in all this example is a nice confirmation of how the procedure outlined above works. In principle this procedure can also be applied step by step to photonic crystals. However it will be more difficult to obtain refraction relations since the size and especially the shape of the equi-frequency lines are complex.

Problems The procedure presented above is very intuitive. Nevertheless there remain uncertainties about the applicability of this approach to photonic crystals. The strongest doubts refer to the boundary condition under the assumption of a constant $\boldsymbol{k}_{||}$. This condition actually holds only for a plane wave (outside) coupling to a plane wave inside the material.

$$\boldsymbol{E}_i(\boldsymbol{r},t) = \boldsymbol{E}_i^0\, e^{i\boldsymbol{k}_i\boldsymbol{r}-i\omega t} \quad \longrightarrow \quad \boldsymbol{E}_r^0\, e^{i\boldsymbol{k}_r\boldsymbol{r}-i\omega t} = \boldsymbol{E}_r(\boldsymbol{r},t)$$

But in the case of photonic crystals the plane wave hitting the boundary of the crystal couples to one or more photonic bands inside. The fields inside are no plane waves but Bloch modes:

$$\boldsymbol{E}_i(\boldsymbol{r},t) = \boldsymbol{E}_i^0\, e^{i\boldsymbol{k}_i\boldsymbol{r}-i\omega t} \quad \longrightarrow \quad \sum_n \sum_{\boldsymbol{k}} \boldsymbol{E}_r^0(n,\boldsymbol{k})\, u_{n\boldsymbol{k}}(\boldsymbol{r})\, e^{i\boldsymbol{k}\boldsymbol{r}-i\omega t} = \boldsymbol{E}_r(\boldsymbol{r},t)$$

Therefore the phase matching condition for $\boldsymbol{k}_i$ and $\boldsymbol{k}_r$ becomes much more complicated and would have to be solved for every specific case separately. This is a virtually impossible task to realize. Nevertheless the theoretical group velocity approach is generally assumed to be applicable for lower bands, since they resemble plane waves more closely than higher bands, due to less terms in the expansion.

The exact evaluation of how well this theory actually holds is still open. Overall a combination of Diffraction or Scattering methods and group velocity considerations, as performed by Gralak et al. [GET00] seems most promising. However I did not have scattering methods at hand and so I was restricted to an analysis in the group-velocity picture.

4.2 Reviewing Existing Superprism Work

The work by Kosaka et al. [KKT$^+$98, KKT$^+$99a, KKT$^+$99b] served as a starting point for me to the topic of photonic crystals and their refraction properties. Initially I tried to confirm their results on ultra-refraction (termed 'superprism effect' by these authors) in order to test my own numerical routines. In doing so I encountered several inconsistencies in their work. Dealing with these problems consumed a significant amount of time but it also greatly increased my insight in the topic. Therefore I want to report in detail about puzzling points in the existing superprism work.

4.2.1 Overview

Basically the work by Kosaka et al. is a combination of the above explained group-velocity approach and experimental tests of predicted refraction properties. The experiment was carried out with (pseudo) 3-dimensional photonic crystals consisting of alternating layers of amorphous Silicon $[n(a\text{-}Si) = 3.24]$ and Silica $[n(SiO_2) = 1.46]$. Each layer of a certain thickness ($h = 0.16\ \mu m$) represents a 2-dimensional triangular lattice (lattice constants: $a = 0.32\ \mu m$ or $a = 0.4\ \mu m$) combined with a hexagonal motif (diameter $d = 0.4a$) of one material embedded in the other (see Fig. 4.13). The crystals were probed with laser-light of wavelength $\lambda = 0.956\ \mu m$ from a vertical cavity surface-emitting laser (VCSEL). The angle of refraction was determined by observing the refracted beam inside the crystal, collecting the scattered light with a CCD-camera viewing the top of the crystal. A schematic experimental configuration along with the geometry of the employed crystal is shown in Fig. 4.13. The corresponding band structure and the resulting contour lines for $\frac{\omega a}{2\pi c} = 0.42 = \frac{a}{\lambda} = \frac{0.40\ \mu m}{0.956\ \mu m}$ and $\frac{\omega a}{2\pi c} = 0.33 = \frac{a}{\lambda} = \frac{0.33\ \mu m}{0.956\ \mu m}$ respectively are depicted in Fig. 4.14. For details please see [KKT$^+$99c].

The resulting data (see Fig. 4.15) exhibits remarkable features never obtained before with classical optical materials. Multiple refraction, negative angles and ultra-high refraction was confirmed experimentally. All these phenomena promise great potential for implementations in integrated optics. However the experimental results could only partially be interpreted theoretically by the authors. In fact only one set of data was confirmed to agree with predictions. The simulated curve [solid line in Fig. 4.15(top)] nicely resembles the measured set of data [dots in Fig. 4.15]. On the other hand the second data set [circles in Fig. 4.15(bottom)] cannot be fitted properly by a theory based on the group-velocity approach. The origin for the discrepancy remains still unexplained except for speculations by the authors about a locally excited surface mode [MBRJ91].

4.2.2 Critical Analysis

My first interest was to implement the geometrical structure of the crystal in Fig. 4.13 in our PWEM program and to test by verifying the band structure diagram of Fig. 4.14. This effort required several 'trial-and-error' attempts since the exact specification of the crystal was not sufficiently provided in references [KKT$^+$98, KKT$^+$99c].

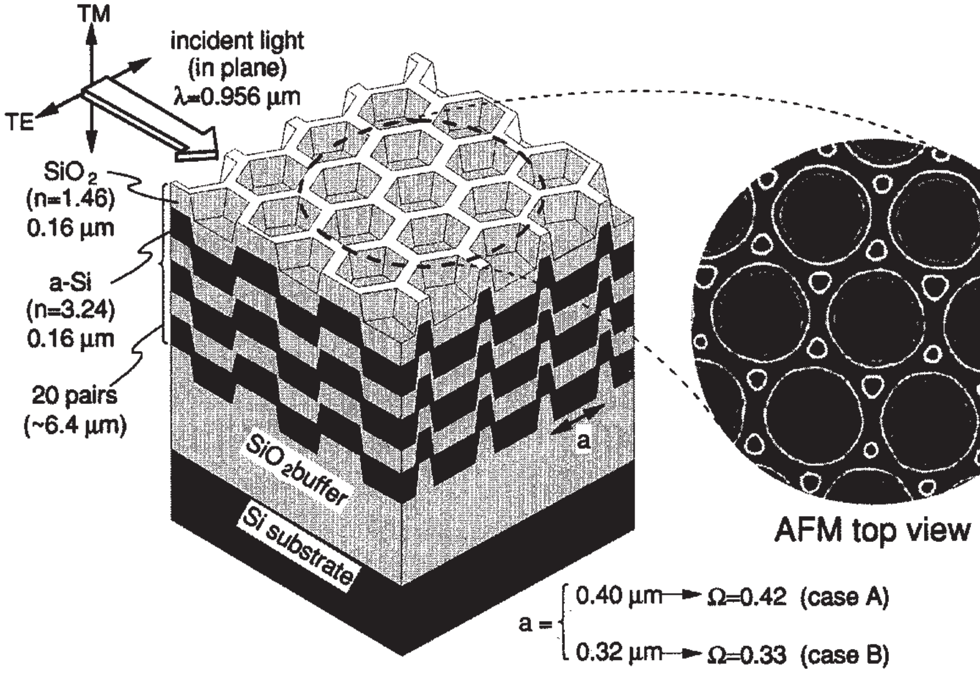

Figure 4.13: *The photonic crystal employed in the experiments by Kosaka et al.*

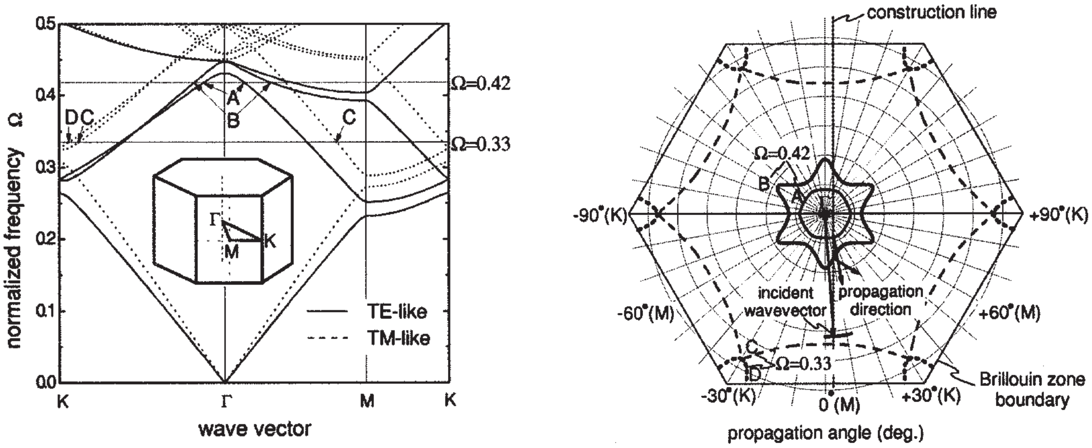

Figure 4.14: *The band structure diagram (left) and corresponding contour lines (right) for the crystal in Fig. 4.13 (from [KKT+98])*

Band Structure Initially I naïvely assumed their calculations to be based on 2-dimensional crystals of arranged hexagonal columns. This implied two possible configurations, either high-index or low-index rods. I performed the band structure calculations for both. The results are shown in Fig. 4.16. It is interesting to compare them with the actual 3-dimensional band structure diagram (see below and Fig. 4.17).

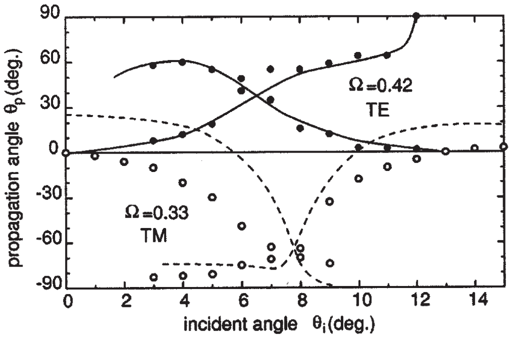

Figure 4.15: *Dependence of the propagation angle on the incident angle observed by Kosaka et al.*

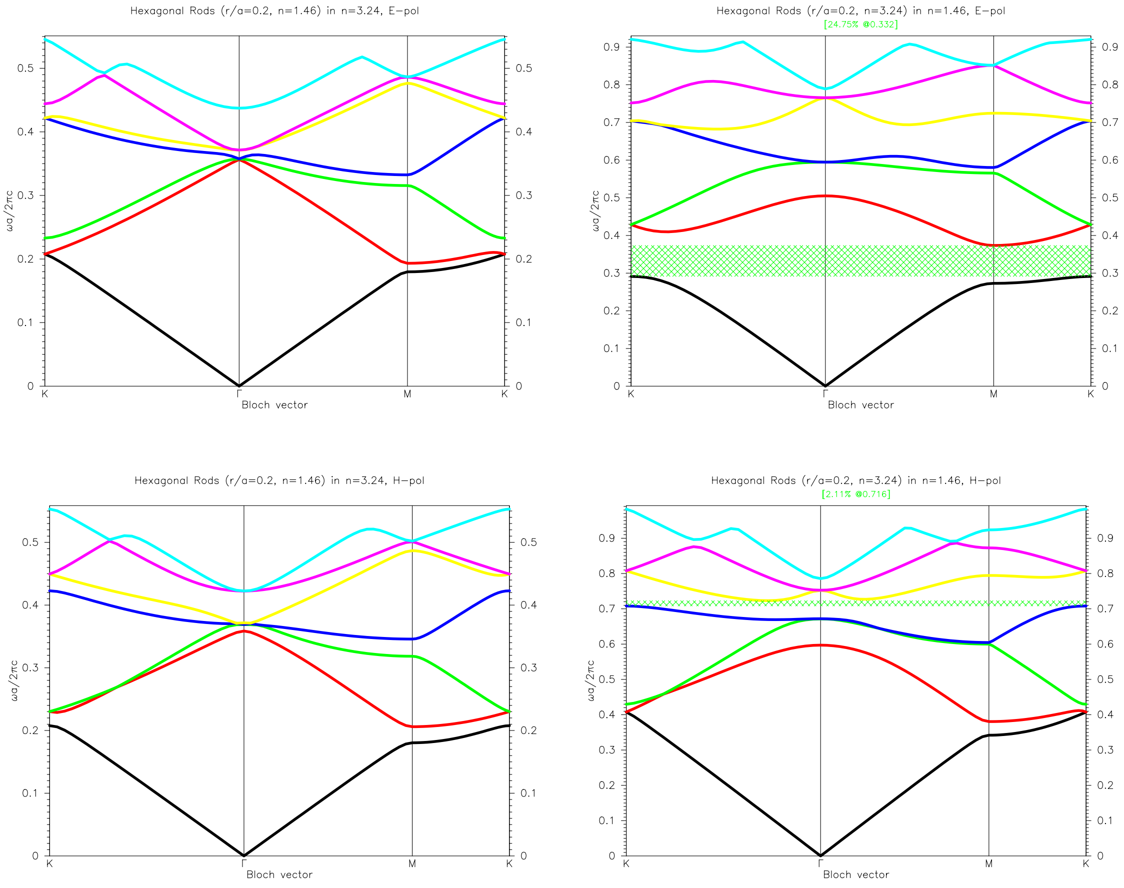

Figure 4.16: *My calculations of 2-dimensional band-structures for hexagonal columns (r/a=0.2) in high index (left) and low index (right) for E-(top) and H-polarization (bottom) respectively.*

The full 3-dimensional crystal structure can be regarded as a hexagonal lattice ($\boldsymbol{a}_1 = \boldsymbol{a}_2 \neq \boldsymbol{a}_3$, $\alpha = 60°$, $\beta = \gamma = 90°$) with a motif formed by the combination of a hexagonal disc ($r = 0.2a$, $h = 0.16\ \mu m$) with a hexagonal rim ($r_{inner} = 0.2a$, $r_{outer} = \frac{a}{\sqrt{3}}$, $h = 0.16\ \mu m$) raised by $0.16\ \mu m$. Motif and backbone are either one of the different refractive indices ($n = 3.24$) and ($n = 1.46$). The results were checked on this intrinsic 'symmetry'. Furthermore the relative thickness of the layers ($h = 0.16\ \mu m$) are different for a crystal with $a = 0.4\ \mu m$ and $a = 0.3\ \mu m$. My simulation also confirmed, as claimed by the authors, that this has no significant impact on the band structure. Therefore the same scale-invariant crystal ($a = 1,\ h = 0.8$) can be used in the computations. The calculated 3-dimensional band structure obtained with a set of 1458 plane waves in our PWEM program is shown in Fig. 4.17.

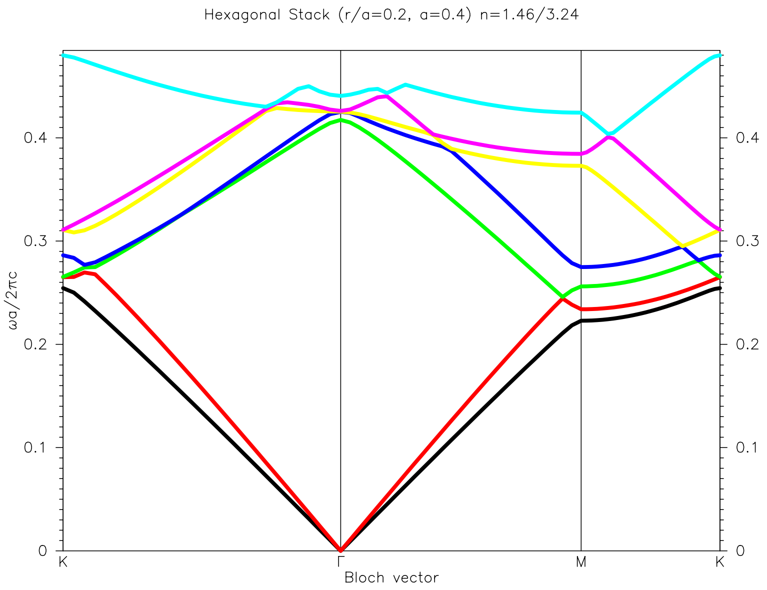

Figure 4.17: *My calculations for the 3-dimensional band structure for the crystal described in [KKT+98]*

This particular structure of the 3-dimensional crystal even allows the definition of polarization directions (see Fig. 4.13). They can be labeled TE and TM regarding the z-axis owing to the fact that its periodicity is different than in the xy-plane. Unfortunately the program I employed does not distinguish polarizations for a 3-dimensional structure. It only labels the bands according to the band index bottom to top. Nevertheless the polarization for different segments of the bands can be retrieved by means of the field distributions. I simply assumed the polarizations defined in the papers [KKT+98, KKT+99c] to be correct and adopted them.

A closer examination of the band structure in Fig. 4.17 and the one shown in Fig. 4.14 shows a difference in normalized frequency of ~ 5% ! This discrepancy was very startling. Because such would impact the refraction properties in a drastical way.

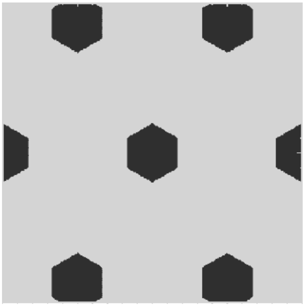

(a) Alternating layers …

(b) Alternating layers …

(c) … to create 3D

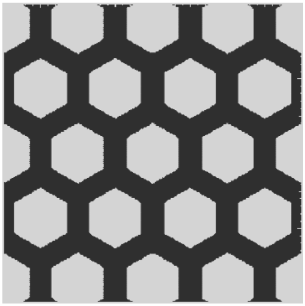

(d) … to create 3D

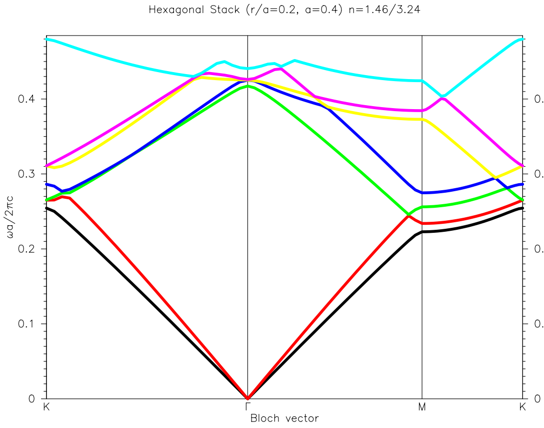

(e) My calculations for the band structure of a crystal as **described** in [KKT+98, KKT+99c]

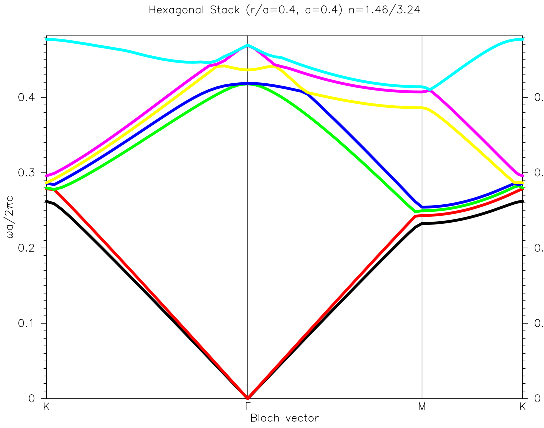

(f) My calculations for the band structure of a crystal as **depicted** in [KKT+98, KKT+99c]

A dispersion surface shifted in height means that the cut at a constant frequency will yield different contour lines. Consequently different refraction properties should be expected theoretically, since the size and shape of the contour line is a very sensitive parameter in the group-velocity approach.

I checked this discrepancy against possible errors in implementing the crystal because it proved difficult to extract the right geometrical configuration from the original papers. It was stated in [KKT+98, KKT+99c] that the diameter of the hexagons is 0.4 times the lattice constant ($d = 0.4a$). I assumed this diameter to be the outer diameter of a hexagon. On the other hand the crystal in Fig. 4.13 rather looks like the radius of the hexagons to be 0.4 times the lattice constant ($r = 0.4a$)! A comparison of the calculated band structures (see Fig. 4.14) nevertheless revealed the structure with $d = 0.4a$ to most closely resemble the diagram presented in the papers [KKT+98, KKT+99c].

Neither slightly modified indices, nor attempts to take account of the inner diameter of a hexagon in the calculations could remove this offset. So I decided to investigate this discrepancy further and analyze the resulting refraction curves.

Contour Lines The calculated dispersion surfaces for the bands number 4,5,6 were calculated in 2-dimensional k-space, ie.e the 1.BZ. They are depicted in Fig. 4.18. The edges or somehow jagged appearance is due to the already mentioned labeling of bands regardless of polarizations.

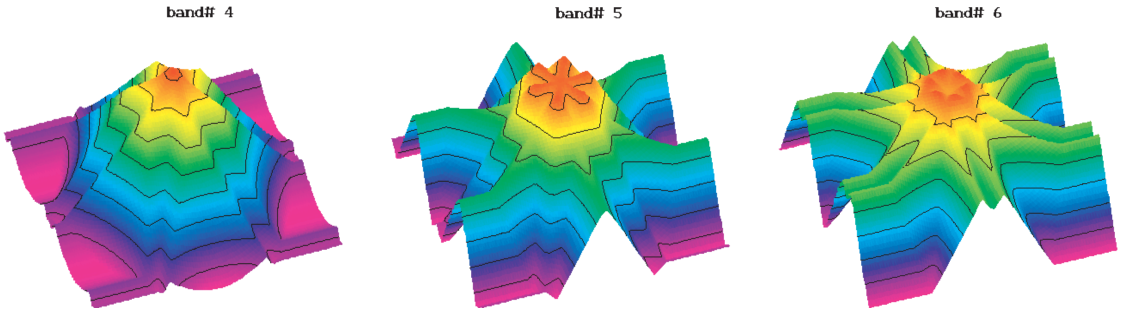

Figure 4.18: *The dispersion surfaces for band #4(left), #5(center) and #6(right)*

First of all I modified the height of the cuts to account for the shift in the bands. This way it was confirmed that a cut at a normalized frequency of $\frac{\omega a}{2\pi c} = 0.401$ yields the predicted curves in the paper (see Fig. 4.19).

The second step is to extract the refraction relation depending on incident angle. Therefore the diameter of the contour line when intersecting the free space dispersion cone at the particular wavelength ought to be known : $R_{free} = 0.401 \cdot 2\pi$.

It is more difficult to extract the contour line of the band(s) cut by this particular frequency. Basically it is just a matter of finding the corresponding wave vectors. But that poses an inverse problem since the bands are expressed as $\omega(\boldsymbol{k})$. In order to 'solve' this problem I calculated the bands along star-lines separated by 1° in the first quadrant of the 1.BZ ($0° \ldots 90°$). The resulting 1-dimensional data could be fitted with high-order polynomials (8 to 11, depending on the complexity and number of

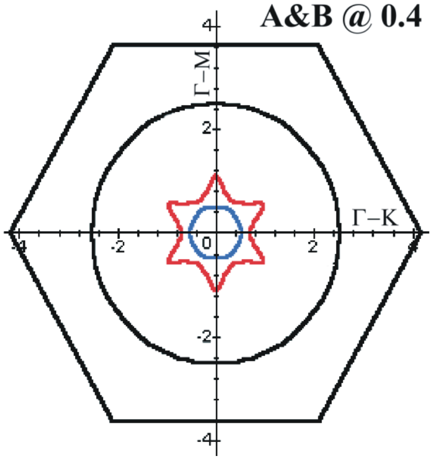

Figure 4.19: *The right equi-frequency lines at* $\frac{\omega a}{2\pi c} = 0.401$

data points), which in turn were solved in the relevant 'radius' region. This strategy is shown in Fig. 4.20. It was implemented by means of a Maple VI script.

Upon knowledge of the equi-frequency lines the incident angle was scanned. By doing so and by constructing the normal (i.e. finding the gradient) to the contour line at its sectioning point with the construction line ($k_{||} = constant$) the refraction relation in Fig. 4.22 was obtained. This sequence is illustrated and summarized in Fig. 4.21.

Three points need special consideration:

- The propagation direction with respect to the crystal axes has to be chosen. In our case the $\Gamma - M$ direction corresponds to an incident angle $= 0°$ (compare [KKT$^+$98]).

- The normal to the contour line is not uniquely determined. Therefore the direction of the gradient needs to be known (remember: The gradient is pointing upward!).

- The $k_{||}$-construction line intersects at least twice with the equi-frequency line. Only proper directions traveling into the crystal ($k_{perp} > 0$) should be selected.

The refraction predicted from the calculations based on these points is shown in Fig. 4.22. The shape of the curves is in good agreement with the curves predicted by Kosaka at al. But quite surprisingly the sign of the refraction is just opposite! (compare with Fig. 4.15). The difference simply arises from the fact that the direction of the gradient stated in the paper is pointing downward. The reason why it fits the observed data anyway is yet unexplained. It is certainly not due to a different definition of the respective angles since the images in the publication [KKT$^+$99c] show the actual beam propagation in- and out-side the crystal.

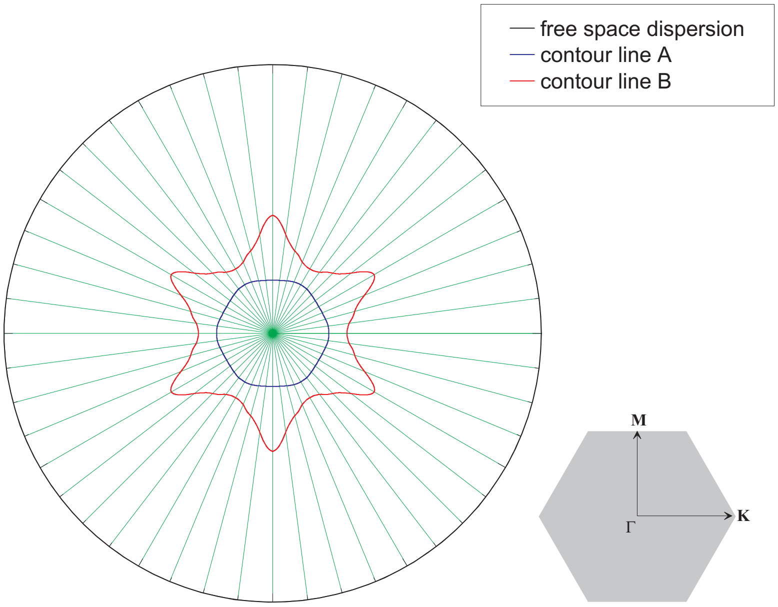

Figure 4.20: *The band structure was calculated along the star-lines and cut at a particular frequency. The corresponding wave-vectors form a contour line in the 1.BZ. The orientation of which is shown in the inset.*

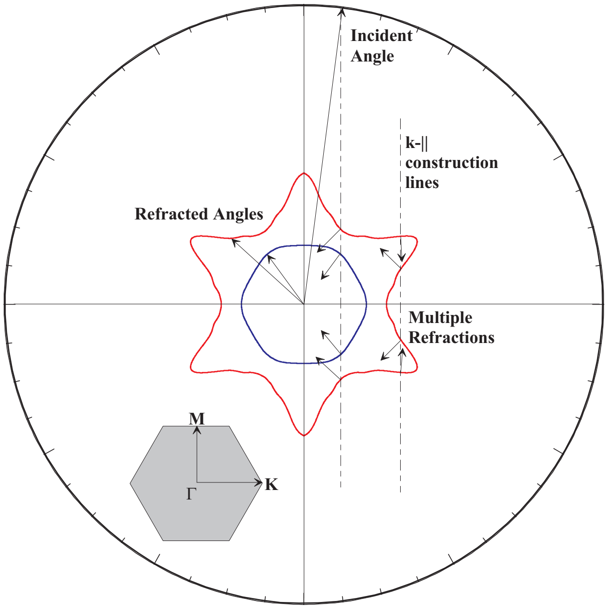

Figure 4.21: *The procedure to extract refraction properties as explained on page 58*

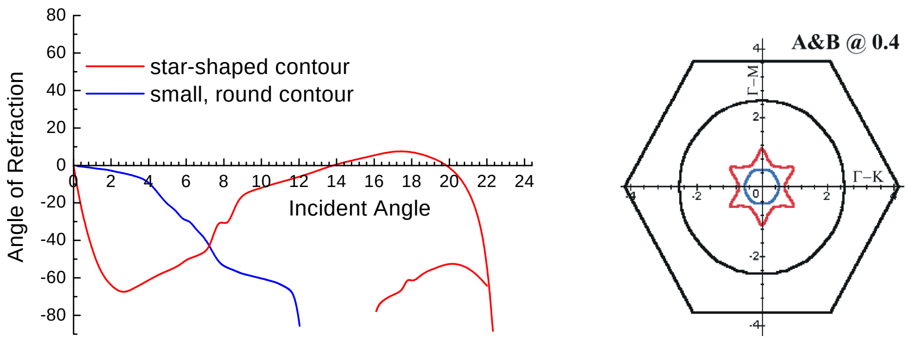

Figure 4.22: *My simulations for the refraction properties in [KKT$^+$98] for* $\frac{\omega a}{2\pi c} = 0.401$

It is also disturbing that the refraction relations for $\frac{\omega a}{2\pi c} = 0.315$ ($\equiv 0.33 - 4.5\%$ to account for the shift) yield completely different theoretical results than the ones presented in [KKT$^+$98] (see dashed line in Fig. 4.15). Although the contour lines are qualitatively the same (see Fig. 4.23. It is not evident how the theoretical predictions (dashed line) in Fig. 4.15 were done. The predicted refraction relation starts at $\sim 25°$. But this is intuitively not clear regarding the shape of the contour line. The calculated curve in Fig. 4.23 would at least be able to interpret the data for small angles, but only if the change in sign is forced. [It remains to note that due to the indetermination of the polarization in our PWEM the true contour lines were selected by hand across the points where they seem to cross (see the red contour lines in Fig. 4.23 example)]

This controversial set of data is only shown in [KKT$^+$98] and not in the subsequent publications.

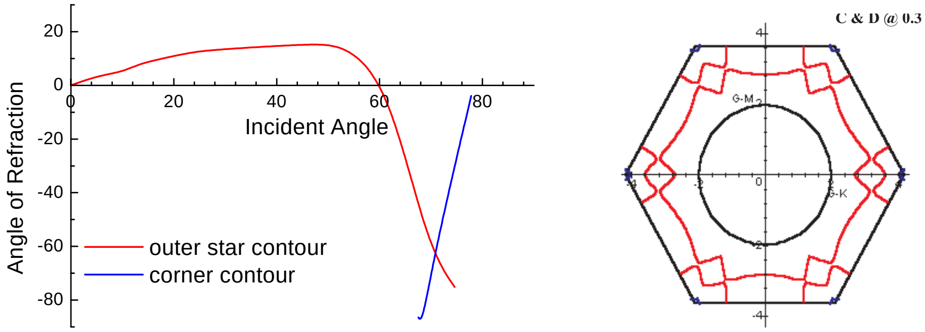

Figure 4.23: *My simulations for the refraction properties in [KKT$^+$98] for* $\frac{\omega a}{2\pi c} = 0.401$

All in all the inconsistencies and 'riddles' seemed to grow the more I engaged in digesting the Japanese work [KKT$^+$98, KKT$^+$99c]. Nevertheless I was motivated by the fact that the method to calculate refraction relations seemed to work (except for the sign?). Furthermore I was hoping to find some clues about the reasons for the discrepancies in the work by Kosaka et al. which they attribute to a locally excited surface mode. So I decided to perform calculations for various scenarios.

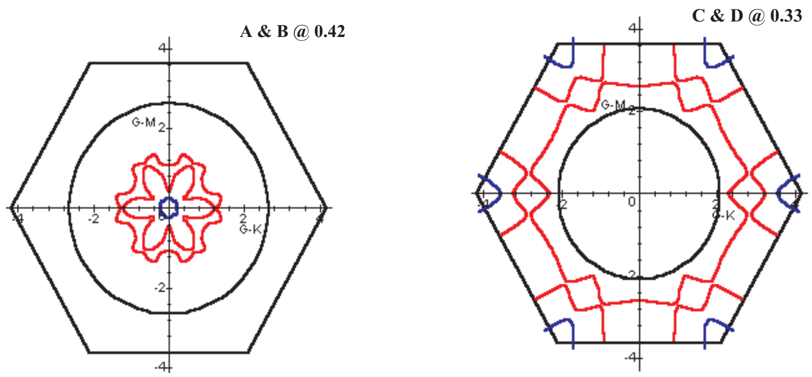

Figure 4.24: *The contour lines obtained without taking the* 5%*-shift of the band structure into account.*

First of all I calculated the contour lines when employing the equi-frequency cuts through our calculated band structure without compensating the 5% shift. The resulting shapes are shown in Fig. 4.24 and especially the one for $\frac{\omega a}{2\pi c} = 0.42$ looks alarmingly different than the one at $\frac{\omega a}{2\pi c} = 0.401$.

The calculated refraction relations based on these equi-frequency lines are shown in Fig. 4.25. Only the curves for $\frac{\omega a}{2\pi c} = 0.401$ in the upper left would actually explain the experimentally observed data up to small angles of $\sim 8°$. But altogether these curves give no deeper insight, except to illustrate that things can get quite complex. This is particularly so when the equi-frequency line consists of more than one band or when one band is intersected more than twice by the $k_{||}$-construction line. In fact it is unclear how the intensity would be distributed among the possible paths in such cases. Perhaps there is also a correlation between the magnitude of the gradient,i.e. group velocity and the energy flux. At least this seems to be tru at the band edges. Furthermore it evident from the above analysis that even the slightest shift in frequency dramatically changes the resulting refraction relations.

Eventually neither the curve for a cut at $\frac{\omega a}{2\pi c} = 0.33$ (upper right in Fig. 4.25) nor a trial for incidence in $\Gamma - K$ direction (bottom graphs in Fig. 4.25) brought any convincing interpretations of the measured data. There would be many parameters in this case to permute (shift, incident direction, gradient direction, polarizations, etc.). But it would be very tedious and doubtful if that could eventually explain the measured data.

In summary the existence of remarkable ultra-refractive effects was directly shown by experimental evidence. Theoretical modeling of the effects however was not very successful. This could of course be partly due to the severe approximations in the boundary problem.

On the other hand the photonic crystal employed in the Japanese experiments is not well suited in my opinion. It consists of rather small structures ($> 100nm$) appropriate for near-IR laser light sources. But the quality of the aspect-ratio of these small features is likelyto be poor. Furthermore the (pseudo) 3-dimensional configuration

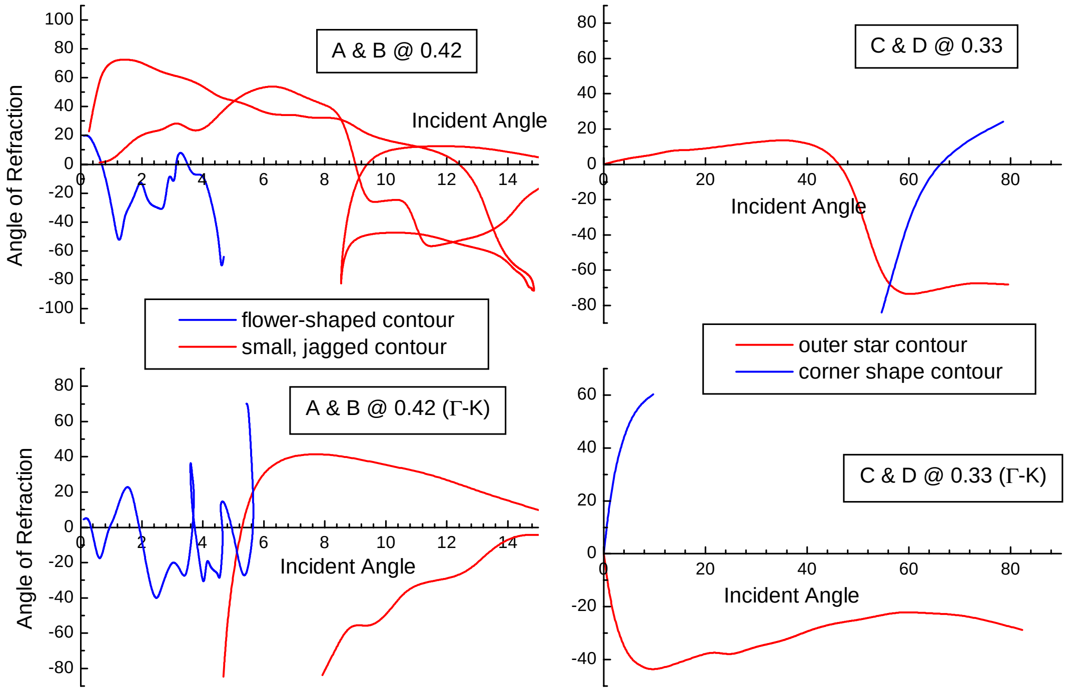

Figure 4.25: *The expected refraction relations for the equi-frequency lines shown in Fig. 4.24.*

adds unnecessary complexity to the delicate matter of ultra-refraction. It remains to establish a link between theoretical approach and the observed phenomena. Therefore a close interplay between theory and suitable experiment is desirable.

4.3 Simulated Refraction Properties of 2-dimensional Si Crystals

The previous section showed that it is not really clear *how* refraction works in photonic crystals. Indeed it exhibits extremely interesting experimental effects but the theoretical explanations lack consistency. It was pointed out that a possible source of error was the complexity of the employed crystals.

Therefore it is desirable to first utilize pure 2-dimensional photonic crystals. Furthermore it is not necessary to use nm-size structured crystal. The scaleability of Maxwell's equations allows equivalent, but easier experiments employing bigger structures. For instance 2-dimensional μm-size structures are already highly developed and posses very high aspect ratios.

4.3.1 Proposed Experiments

In collaboration with Prof. Henry van Driel's research group at the University of Toronto, in particular Jessica Mondia, Steve Leonard and Hong Wee Tan the plan was formed to check the theory of the superprism effect with straightforward experiments.

Crystals The available crystals (see Fig. 4.26) were state of the art 2-dimensional photonic crystals fabricated by the MPI in Halle/Germany [http://www.mpihalle.mpg.-de/˜porous_m/] using reactive ion etching techniques. They consist of air columns forming a triangular lattice in a backbone of Si. They come in slabs with the accessible side perpendicular to the $\Gamma - M$ direction. The slab is supported by thicker parts, resulting in a comb-like, funny-looking shape since the aspect ratio is enormously high, i.e. the columns are very deep compared to their diameter.

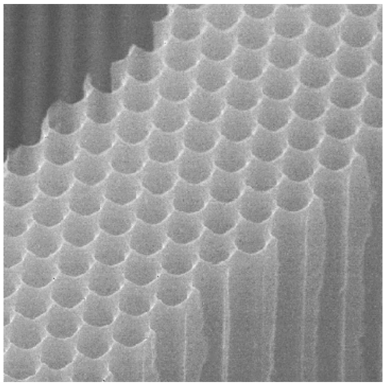

Figure 4.26: *SEM picture of a two-dimensional photonic Si-crystal, fabricated at MPI, Halle.*

Two different filling fractions were available. One with 44.4% air filling ($\frac{r}{a} = 0.35$). The other one has an optimized filling fraction for a maximized TE-gap with 64% air filling ($\frac{r}{a} = 0.42$). Furthermore there were two different pitches, i.e. lattice constants: $a = 1.5\ \mu m$ and $a = 1.58\ \mu m$ for every filling fraction. This makes altogether 4 different configurations regarding polarizations. The absolute pitch does not matter in the band structure calculations because of the scale invariance in Maxwell's equations. The bands were calculated using ~1200 plane waves in the PWEM program. They are shown in Fig. 4.27.

Light-sources The above described crystals should be well suited for our task to analyze the refraction properties of photonic crystals. But due to their lattice constants of $a = 1.5\ \mu m$ and $a = 1.58\ \mu m$ the interesting region in normalized frequency ($\frac{\omega a}{2\pi c}$) is around $2\ \mu m - 4\ \mu m$.

But in this wavelength regime no conventional monochromatic light-sources (lasers) in order to probe them were easy at hand. Eventually it turned out that lasers with a wavelength of $\lambda = 2.39\ \mu m$ and $\lambda = 3.39\ \mu m$ would be at our disposal at Photonics Research Ontario (PRO). The bandwidth of these lasers was stated to be $\sim 20nm$. In the band structure diagram these wavelengths correspond to constant frequency sections at $\frac{a}{\lambda} = 0.44,\ 0.63$ for a lattice constant of $a = 1.5\ \mu m$ and $\frac{a}{\lambda} = 0.47,\ 0.66$ for a pitch of $a = 1.58\ \mu m$ respectively.

Applying these cuts to the 4 band structure diagrams in Fig. 4.27 yields a variety of 12 bands which are actually intersected. Exclusively those bands are relevant for the following closer examination.

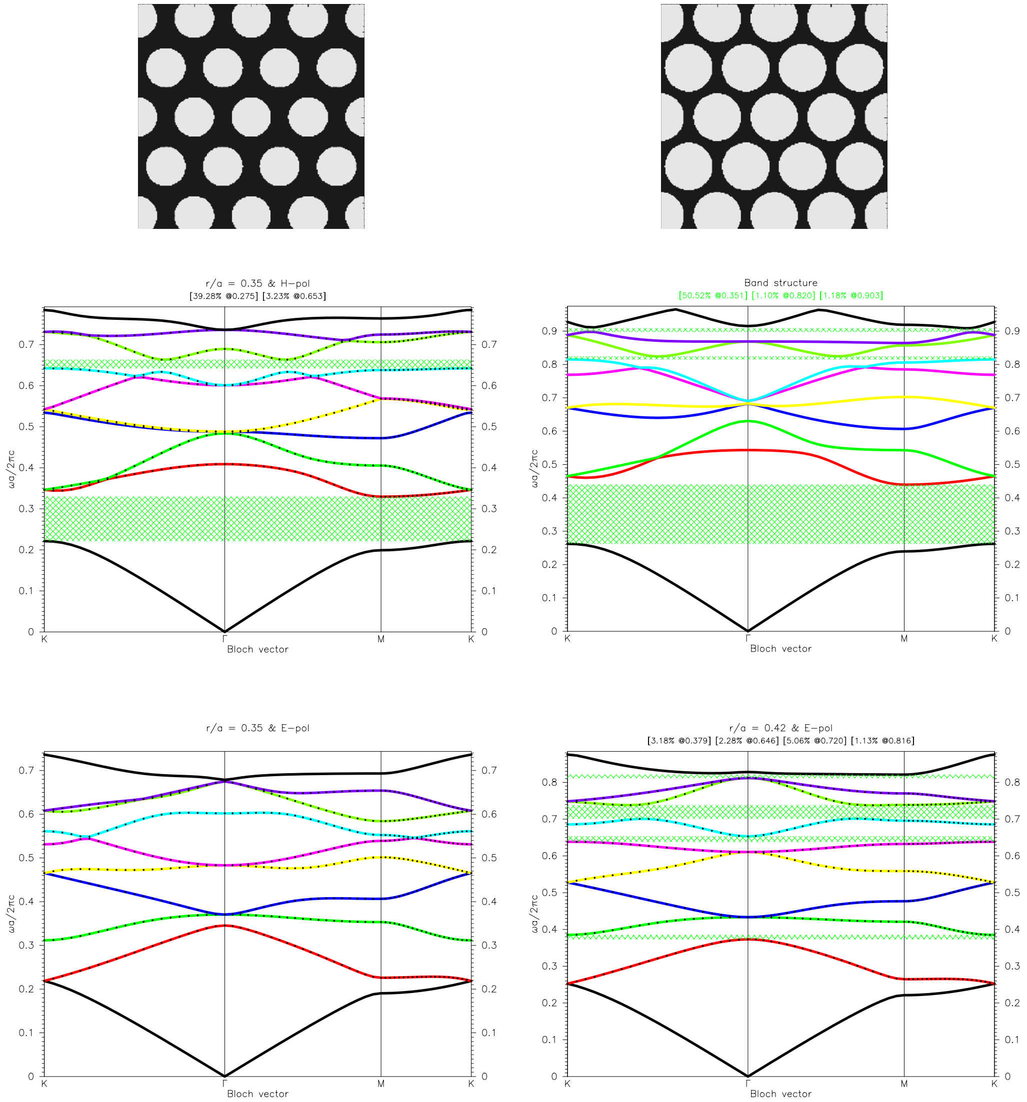

Figure 4.27: *Photonic crystals consisting of air columns (r/a=0.35 [left] and r/a=0.42 [right]) in a Silicon (n=3.45) backbone. TE (H-polarization) [top] vs. TM (E-polarization) [bottom]*

4.3.2 Expected Phenomena

In order simulate the refraction properties for the proposed experiments the relevant bands were calculated in the complete 2-dimensional 1.BZ. I will limit the results and discussions here to 4 important and typical examples. Furthermore a certain bandwidth ($20nm$) is included in the following analysis. The red (or magenta) curve and the blue (or cyan) curve correspond to the red and blue 'edge' of the bandwidth.

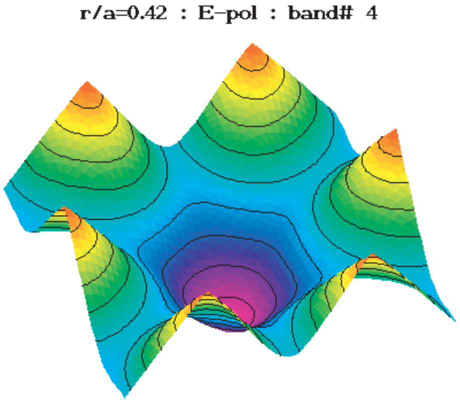

Figure 4.28: *Dispersion surface of band # 4 ($r/a = 0.42$, E-pol)*

Ultra-Refraction When the band structure of ($r/a = 0.42$, E-pol) is cut at 0.44 ($\leftrightarrow a = 1.5\ \mu m, \lambda = 3.39\ \mu m$) its forth band is intersected. The dispersion surface of this band is shown in Fig. 4.28. In figures 4.29 and 4.30 the contour lines and resulting refraction relations are depicted respectively.

Here ultra-refraction in the form of strong refraction is evident. The variation of $0 \ldots \sim 15°$ in incident angle yields refraction angles of $0 \ldots 90°$ in a regular manner. Therefore some sort of refractive index $n = \sin 15° = 0.26$ could be matched this refraction curve. The index is less than 1 since the contour line is (significantly) smaller than the free space dispersion. This is in some analogy to the discussion by Dowling and Bowden [DB94] (see page 52) for the 1-dimensional case. The regular behavior of the refraction curve can be attributed to the shape of the contour line which is almost circular. Furthermore the curve exhibits very strong dispersion since the spread of $20nm$ in wavelength splits over angles of up to $\sim 20°$. This may confidently be called 'superprism effect'.

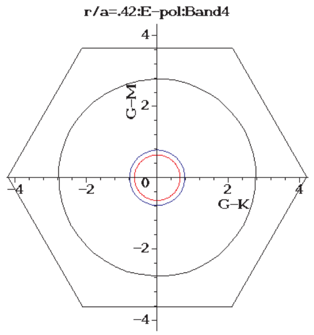

Figure 4.29: *Resulting contour line for a cut at 0.44*

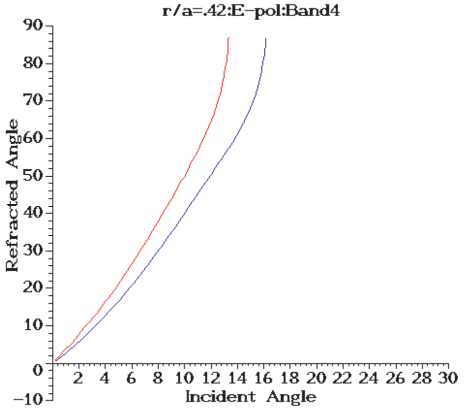

Figure 4.30: *Simulated refraction behavior showing ultra-refraction*

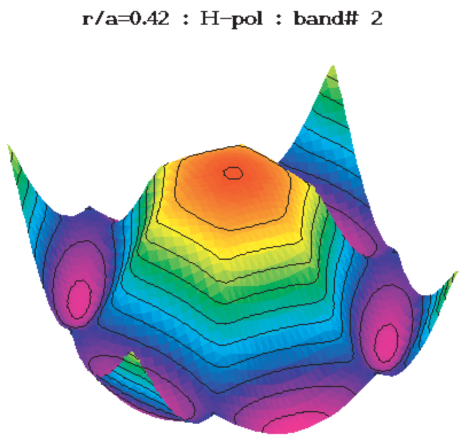

Figure 4.31: *Dispersion surface of band # 2 ($r/a = 0.42$, H-pol)*

Negative-Refraction For a normalized frequency cut at 0.47 ($\leftrightarrow a = 1.58\ \mu m$) the second band of the configuration ($r/a = 0.42$, H-pol) is intersected. Figure 4.31 depicts its surface plot and figures 4.32, 4.33 its contour lines and refraction relations respectively.

In this case negative refraction can be observed. The wiggles in the relation are due to the form of the contour line which deviates from a circular shape. It is also remarkable that the frequency dispersions changes with angle. In the range of $0 \ldots 20°$ the long wavelength part of the bandwidth is deflected more, in the range of $50 \ldots 70°$ the short wavelength side. Furthermore there exist almost no dispersion for the distinct wavelengths in the range of $20 \ldots 50°$. This can be interpreted in a way that the size of the contour lines is very close to that of the free space dispersion. A contour line with the exact same radius would of course yield a refractive index of 1. This also accounts for the strength of refraction in this case: $0 \ldots 75° \rightarrow 0 \ldots -90°$.

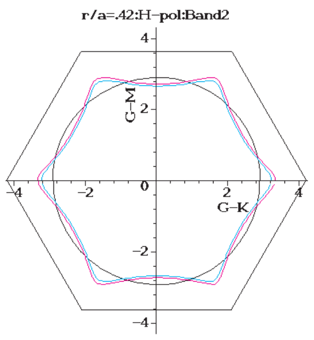

Figure 4.32: *Resulting contour line for a cut at 0.47*

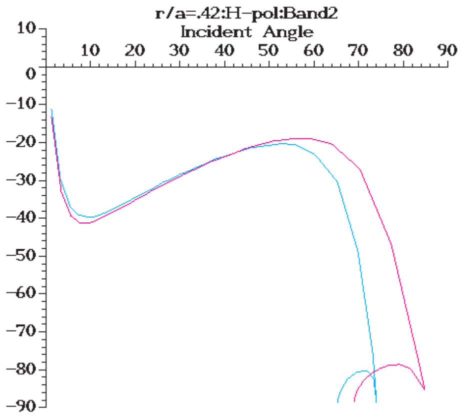

Figure 4.33: *Simulated refraction behavior showing negative refraction*

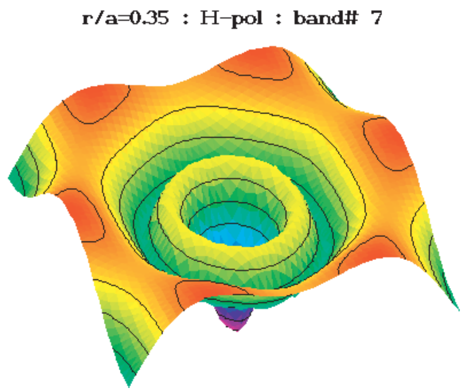

Figure 4.34: *Dispersion surface of band # 7 ($r/a = 0.35$, H-pol)*

Multi-Branching The band # 7 of the constellation ($r/a = 0.35$, H-pol) is cut at 0.63 ($\leftrightarrow a = 1.5\ \mu m$). For the dispersion surface see Fig. 4.34, for the contour lines 4.35. The resulting refraction relations are illustrated in Fig. 4.36.

Since the cut intersects three times with the same band multi-branching occurs. Additionally the gradient for one of the contour lines is opposite to the other two and therefore light is refracted to negative angles. The frequency dispersion for negative refraction is also opposite to positive refraction. The behavior of the frequency dispersion exclusively depends on the orientation of the gradient and the relative size of the contour line compared to free space (see Fig. 4.33). The strength of the different branches can again be attributed to their varying sizes. No prediction (at least in our approach) can be made about the energy distribution to the distinct branches. The same applies when intersecting more than one band. Another case for multi-branching to occur.

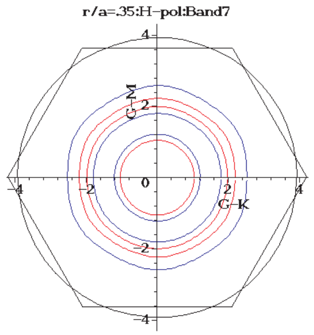

Figure 4.35: *Resulting contour line for a cut at 0.63*

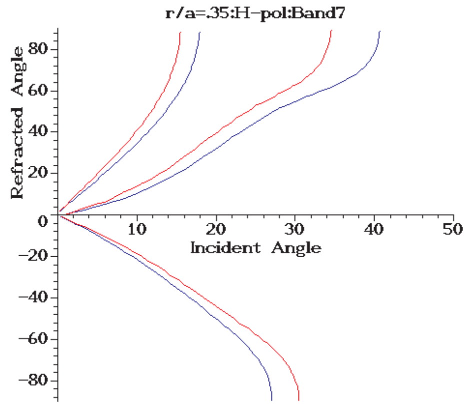

Figure 4.36: *Simulated refraction behavior showing multi-branching*

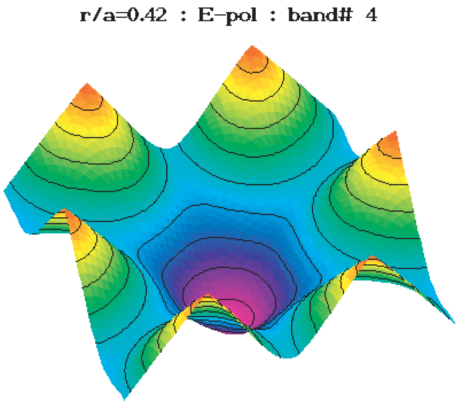

Figure 4.37: *Again the dispersion surface of band #4 ($r/a = 0.42$, E-pol)*

Beam-Steering Again band #4 of the crystal with ($r/a = 0.42$, E-pol) is cut but this time at a normalized frequency of 0.47 ($\leftrightarrow a = 1.58\ \mu m$). As usual the surface plot is depicted on the top of the page (Fig. 4.37) and the contour lines as well as the refraction curves can be found at the bottom of the page in figures 4.38 and 4.39, respectively.

Owing to its almost hexagonal shape this curve exhibits beam-steering qualities. In the range of $0\ldots10°$ and again at $25\ldots35°$ the angle of refraction for the red part of the bandwidth remains constant. Therefore this constellation would be extremely insensitive to variation in the incident angle. Generally a contour line with straight domains exhibits these properties. On the other hand if there are corners present in the contour line than excellent switching can be achieved by slightly varying the incident angle.

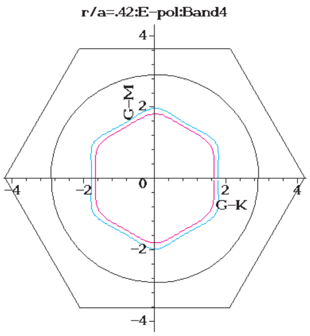

Figure 4.38: *Resulting contour line for a cut at 0.47*

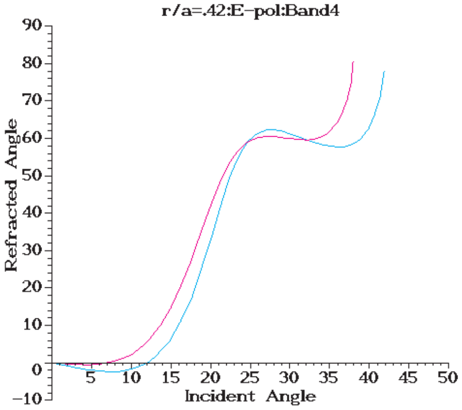

Figure 4.39: *Simulated refraction behavior showing beam-steering properties*

4.4 Conclusions

In summary a review was given on the work done on ultra-refractive effects by photonic crystals. After an intuitive 1-dimensional argument, approaches to tackle the problem of non-normal, non-monochromatic incidence of light on photonic crystals were presented. The methods tracing the electromagnetic field through a slab of crystal and its boundaries show beautiful, promising results of anomalous refraction properties. The group-velocity approach offers a deeper understanding of the mechanisms involved but relies on a weak boundary condition. Furthermore experimental evidence of ultra-refraction is present. The results could partly be explained by means of the group-velocity method. This method was also employed for simulating theoretical refraction relations of purely 2-dimensional crystal in a designated experiment. The predictions confirm expectations of extraordinary refraction properties achievable with photonic crystals. But these refraction phenomena only occur in a very distinct wavelength range and are subject to greatest precision. Unfortunately the proposed experiments were never accomplished.

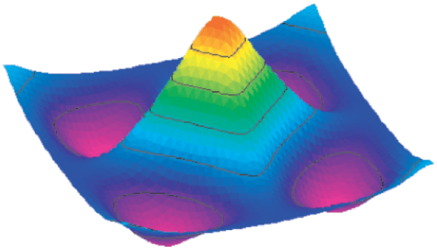

Figure 4.40: *A prospect band for superior beam-steering applications*

The applications of ultra-refractive effects in industry are promising and numerous, especially in the booming field of optical telecommunications. But in order to make use of the phenomena they have to be set on a firm basis. This is only possible with an interplay between experimental and theoretical aspects of this field.

Chapter 5

Optical Properties of Colloidal Crystals

This chapter covers a collaboration with Matthias Soddemann and Prof. Walter Richtering, Kiel (Deptartment of Applied Physical Chemistry of Polymers and Colloids) (formerly Freiburg). They prepared and experimentally analyzed photonic crystals based on colloidal particles, as described in section 2. First a brief overview of the field of colloidal crystals is given in section 1. Then I will report on theoretical simulations based on the methods explained in chapter II for the optical properties of their specific crystals. Results will be shown and discussed. A publication on our combined efforts is in preparation.

I wish to thank Dr. Carsten Winnewisser and Prof. Jürgen Schneider from the Freiburger Materialforschungszentrum FMF who were responsible for this collaboration to materialize.

5.1 Overview

Basically colloidal particles represent a link between huge molecules and tiny particles. Typical size scales are shown below in Fig. 5.1.

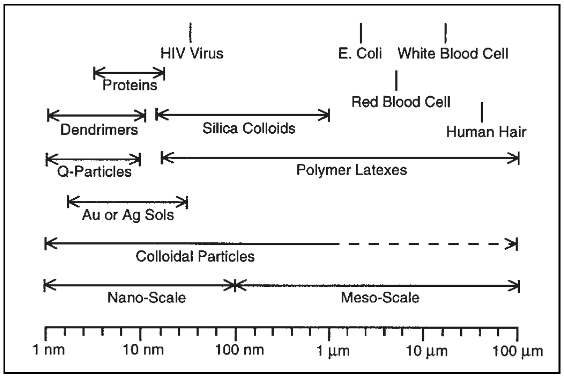

Figure 5.1: *Representative colloidal systems with typical dimension ranges*

Photonic crystals made out of colloidal systems attract much attention nowadays. This is mainly due to their formation process of self-assembling in a 3-dimensional crystal with excellent long range periodicity. This elegant and fast way of fabrication is superior to micro-lithography and layer-by-layer methods. Colloidal particles have long been synthesized ($\sim$ 1930's), scientifically studied and applied in industry. They are available in a wide range of materials and sizes. This makes colloidal crystals very suitable as photonic band gap (PBG) materials in the optical and near infrared (NIR) wavelength domain. The best established systems are silica colloids (opals) and polymer latexes like PMMA (polymethylmethacrylate) and PS (polystyrene).

However most colloidal materials do not have high dielectric constants. To overcome this obstacle a common method is to use the colloidal crystals as templates which are then in turn infiltrated with higher index material. In this fashion, state of the art photonic crystals have been manufactured. In the form of inverted opals of Si with a complete band gap at the optical telecommunication wavelength of 1.5 μm [BCG$^+$00].

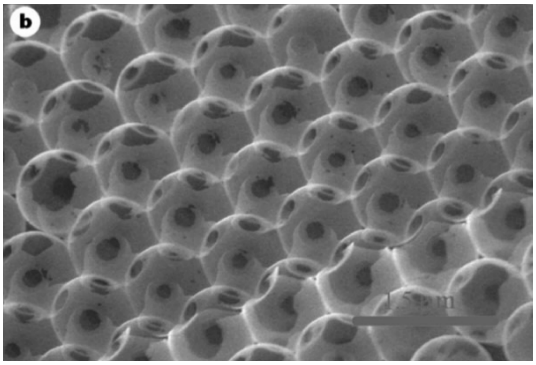

Figure 5.2: *State of the art photonic crystal: inverted opal in Silicon [BCG$^+$00]*

A very important feature of colloidal spheres is that they can be made monodisperse, i.e. all having the same size. The size and even the intrinsic structure of the spheres can be adjusted in the chemical synthesis. Some typical kinds, like a solid sphere (with surface groups), a core shell sphere and a hollow sphere are shown in Fig. 5.3.

The crystallization of monodispersed spheres is possible in various ways. Hard spheres will self-assembly simply by sedimentation or by hydrodynamic flow and physical confinement [see Fig. 5.4 (A) and (C)]. The resulting crystal structure is generally cubic-close-packed (ccp, corresponds to fcc with 74% volume fraction as in naturally occurring opals) or hexagonal-close-packed (hcp). A phase diagram illustrating crystallization is shown in Fig. 5.5 (A). Charged colloidal spheres arrange themselves by repulsive electrostatic interactions [Fig. 5.4 (B)] and crystallize preferably in a face-centered-cubic structure. A body-centered-cubic (bcc) lattice type can be achieved under the right conditions (Fig. 5.5).

An excellent overview on the synthesis, crystallization and applications of colloidal systems is given in the article by Y. Xia [XGYL00] where the three shown figures are taken from.

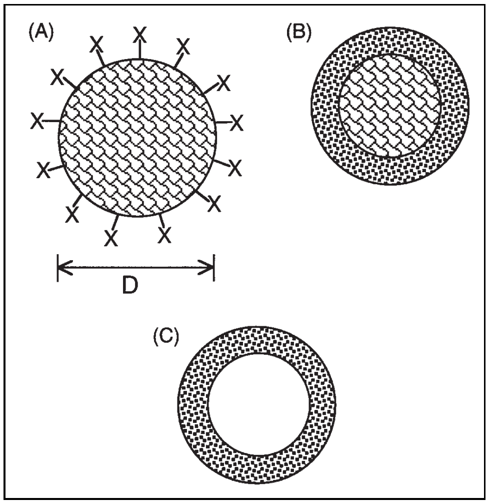

Figure 5.3: *Different kinds of monodispersed particles: (A) solid sphere [with magnified surface groups], (B) core shell sphere and (C) hollow sphere*

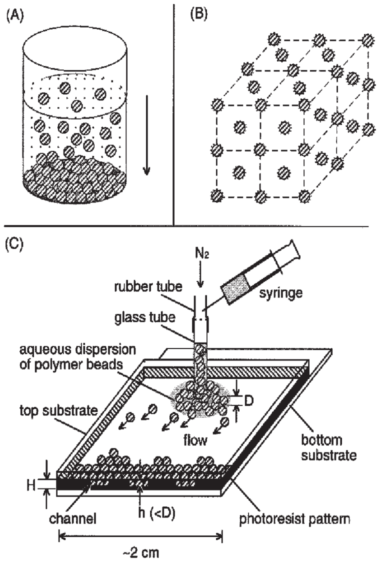

Figure 5.4: *Crystallization methods: (A) Sedimentation, (B) Electrostatic repulsion and (C) Hydrodynamic flow with physical confinement*

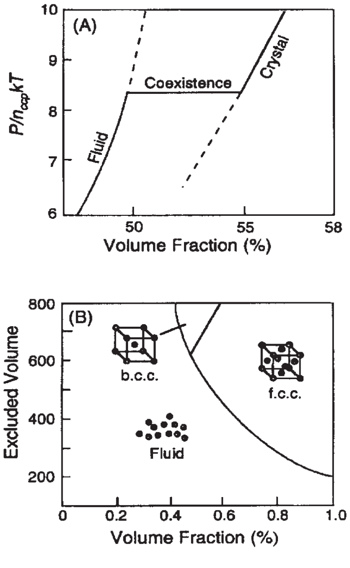

Figure 5.5: *Phase diagrams for crystallizing hard spheres (top) and charged particles (bottom)*

5.2 Synthesis and Experimental Characterization

The particular colloidal crystals under study in this work were synthesized and crystallized by M. Soddemann. Basically they comprise highly charged monodispersed colloidal spheres in aqueous solution. Some of the samples were further fixated by embedding them in a hydrogel matrix. The images shown in this section are excerpts from M. Soddemanns Diploma Thesis [Sod98].

Polymerization The colloidal emulsions were prepared following a standard procedure. Polystyrene (PS) latex dispersions were synthesized by means of *emulsifier-free emulsion polymerization* from the monomer styrene. To initiate the polymerization potassium peroxosulfate was used. The potassium salt of p-styrenesulfonic acid functioned as a stabilizer. The polymerization was allowed to proceed at $80^\circ\,C$ for 10h. The resulting size of these PS spheres is determined by the experimental parameters and can be adjusted to desired values.

Determination of the Particle Size Mainly dynamic light scattering (DLS) by means of a Krypton ion laser ($\lambda = 647\,nm$) was employed to determine the size of the PS beads diluted in water. A standard computer program extracted the actual diameter from the angle dependent data. Furthermore the particle sizes were measured via transmission electron microscopy (TEM) and digital image analysis of several hundreds of clearly separated particles (see Fig. 5.6 for a typical image). This procedure confirms almost perfectly spherical particles with a diameter of $113 \pm 6\ nm$. This is a size distribution on the order of 6%.

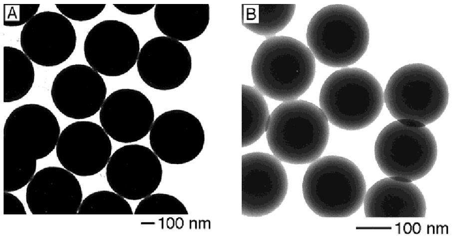

Figure 5.6: *Transmission electron microscopy (TEM) image of PS beads in water [XGYL00]*

However the diameter resulting with the DSL method yielded values of $150 \pm 7\ nm$. The discrepancy is not clear. The DSL results seemed to be more trustworthy and were backed by measurements of a fluorescence-correlation-spectrometer (FCS).

Crystallization Impurities in the dispersion were removed by dialysis for 1-2 weeks. Then ultra-pure water was added to the latex. Latex concentrations used in this study were 1.0 to 6.0 wt.-% (wt.-%= mass fraction $\mu = \frac{m_{PS}}{m_{PS}+m_{H_2O}}$). The crystallization took places in a capillary flow cell ($0.4 \times 5 \times 40\ mm$) where a peristaltic pump slowly circulated the dispersion added to an ion exchange resin (mixture of both anionic and cationic ion exchange resins) (see Fig. 5.7).

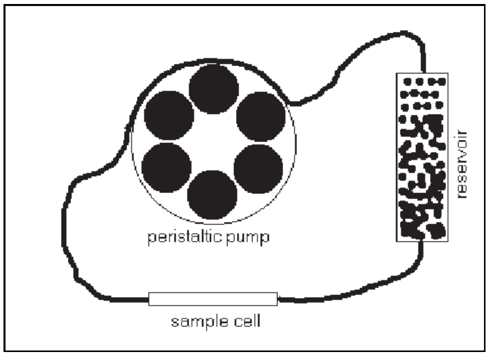

Figure 5.7: *Schematic apparatus for preparation of colloidal crystals*

The crystals were grown in an fcc lattice type from the window of the cell. Their (111) crystal plane is generally assumed to be oriented parallel to the window. The shear of the hydrodynamic flow further let them grow along the capillary. An fcc lattice is the preferred configuration for concentrations of more than 3 wt.-%. Concentrations less than 1 wt.-% yield a bcc lattice type (compare with Fig. 5.5). However less concentrated dispersions are very difficult to crystallize.

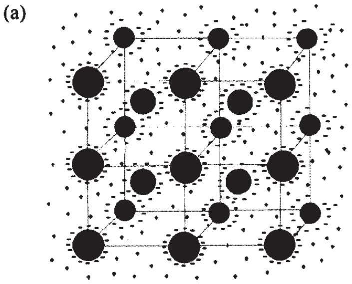

Figure 5.8: *Colloidal crystal in aqueous solution*

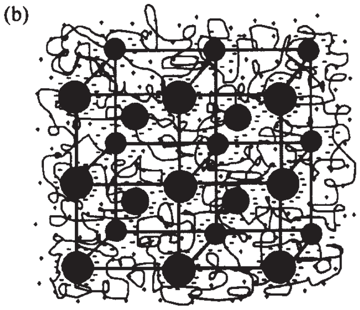

Figure 5.9: *Hydrogel fixated colloidal crystal (schematic)*

Since these crystals in aqueous solution are unstable it was intended to embed them in a hydrogel matrix (see figs. 5.8 and 5.9). In order to achieve this, a mixture consisting of a monomer (acrylamide), a cross-linker (N,N'-methylenebisacrylamide) and a UV-photo-initiator (diethoxyacethophenone) was added to the dispersion. After crystallization the sample cell was exposed to UV-light ($\lambda = 254\ nm$). This led to polymerization, forming an acrylamid network which stabilized the crystal without disturbing the periodicity of the particles. Such systems are referred to as polymerized crystalline colloidal arrays (PCCA) [HA97]. The so fixated colloidal crystals were, and remained extremely well oriented and were of the physical size of the cell itself.

Optical Measurements The formation of the crystals could be viewed by the naked eye. They exhibit beautiful iridescence in the visible and appear in angular dependent reddish to greenish colors on a basically white hue. The exact optical properties were measured by means of transmission spectroscopy with a UV/VIS/NIR spectrometer (Perkin Elmer Lambda 11 & Lambda 2). In order to get angle resolved transmission data the cell containing the crystal was mounted on a rotation stage. This allowed its re-orientation around the vertical axis. This is schematically depicted in Fig. 5.10.

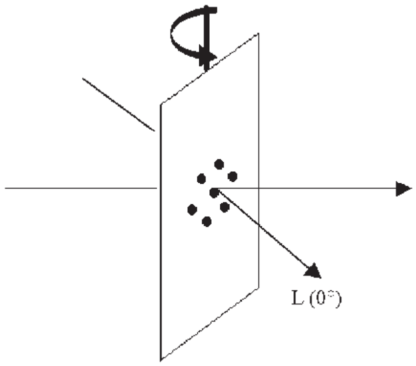

Figure 5.10: *Schematic setup of angular dependent transmission measurements*

5.3 Results And Theoretical Simulations

It is known that the PS spheres with a radius of $r \approx 75\ nm$ arrange themselves in an fcc lattice type as shown in Fig. 5.11. The volume fraction of PS, i.e. the filling fraction can be determined from the known mass fraction μ and the density of PS ($\varrho_{PS} = 1.05\ g/cm^3$):

$$f = \frac{\mu}{\varrho_{PS}} \tag{5.1}$$

The geometrical lattice filling fraction of the fcc lattice is given by

$$f = \frac{16\pi}{3}\left(\frac{r}{a}\right)^3 \tag{5.2}$$

The values obtained through this geometrical arguments for r/a in a crystal with 6.0 wt-% (from now on referred to as crystal M60) and one with 4.3 wt-% (M43) are 0.151 and 0.135 respectively. This corresponds to lattice constants of 498 nm for M60 and 557 nm for M43.

A typical result of the transmission measurements for the crystals (here M60) is shown in Fig. 5.13. This scan was recorded under normal incidence on the cell window, which corresponds to the crystallographic Γ-L direction. Clearly a well defined minimum is observed in transmission at a wavelength of $\sim 760\ nm$.

According to classical Bragg - von Laue theory these transmission minima can be interpreted as diffraction peaks. Classically speaking diffraction from consecutive layers of spheres in the crystal [in our case the (111)-plane] leads to destructive interference.

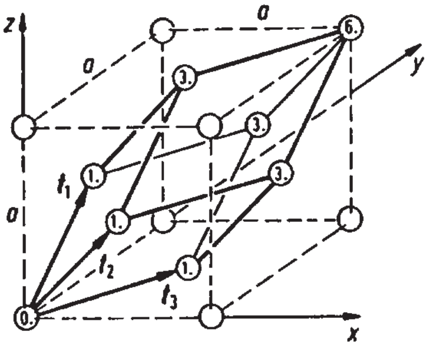

Figure 5.11: *The fcc lattice and its conventional (dashed) and primitive (solid) unit cell*

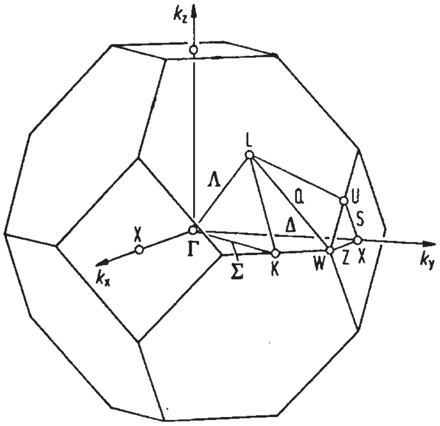

Figure 5.12: *1.BZ of the fcc lattice with symmetry points*

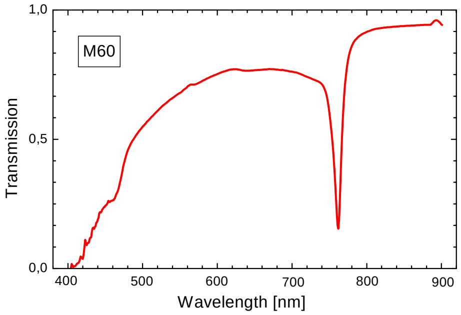

Figure 5.13: *Transmission of M60 at normal incidence*

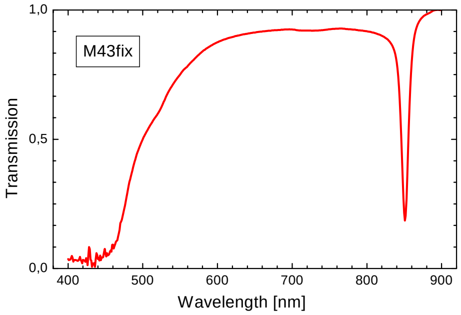

Figure 5.14: *Transmission of M43fix at normal incidence*

Thus the lattice constant a can alternatively be extracted by applying the quadratic Bragg equation applicable for cubic crystals:

$$a^2 = \frac{\lambda^2}{4n_{eff}\sin^2(\theta)}(h^2 + k^2 + l^2), \tag{5.3}$$

where h, k, l are the Miller indices [(1,1,1) in our case] and n_{eff} the mean value of the refractive indices (water n=1.333, polystyrene n=1.59). The effective refractive index has to be averaged by the volume fraction of the compounds and yields $n_{eff} =$ 1.348 and 1.344 for the M60 and M43 crystal respectively.

This directly results in lattice constants of ~ 490 *nm* and ~ 550 *nm*. The discrepancy of $\sim 2\%$ compared to the geometrically derived lattice constant is well within the experimental uncertainty limits. The main difference certainly stems from the uncertainties in determining the radius of the spheres.

Further measurements resolved the angular dependency of the transmission through the sample. It was recorded for angles of 0° …55°. (An angle of 53° is generally assumed to correspond to the crystallographic Γ-W axis, since L-Γ-W embrace an angle of so much). The results for the sample M60 are plotted in Fig. 5.15 and Fig. 5.16. In

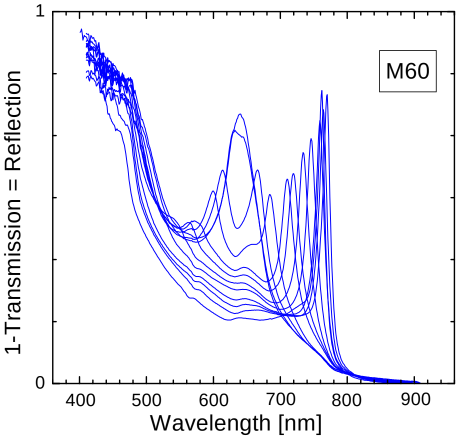

Figure 5.15: *The evolution of the diffraction peaks with incident angle (plotted as 1 minus transmission, which is equal to the reflection in such a lossless system)*

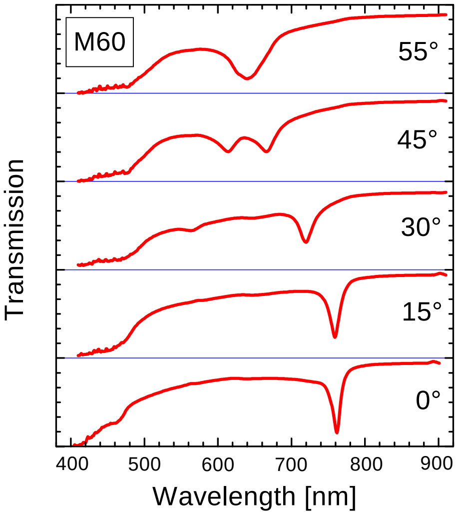

Figure 5.16: *Angular dependency of the transmission curves*

Fig. 5.15 the absorption curves (in this case this corresponds to reflection curves since the system is absorptionless and R+T=1) for increasing angles are plotted in the same diagram. The angular evolution of the diffraction peaks can qualitatively be followed.

For the angular transmission data of the M43fix crystal see Fig. 5.27. A remarkable shift of the transmission minimum from ~ 760 nm to ~ 630 nm is noticeable in Fig. 5.16 when rotating the crystal from 0° to 55° . Additionally a second dip evolves for angles greater than 30° and merges with the original one.

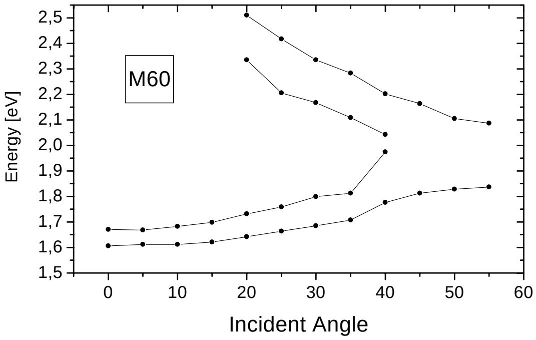

Figure 5.17: *Extracted qualitative band gap diagram from Fig. 5.16 for M60*

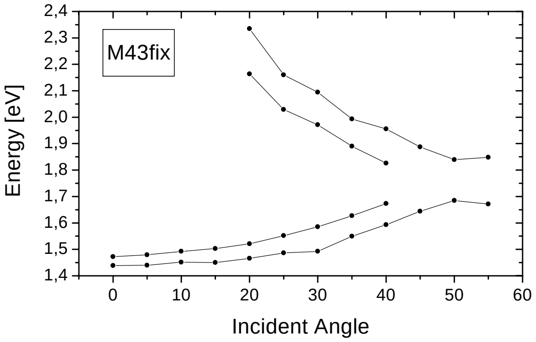

Figure 5.18: *Extracted qualitative band gap diagram from Fig. 5.27 for M43fix*

The data obtained in this way was transferred by M. Soddemann to a qualitative band gap (i.e. band structure) diagram. He measured the size and position of the transmission gap on its base and plotted it versus the incident angle (see Fig. 5.17).

My first task was to verify this band gap diagram with the PWEM program at hand. The parameters entered were a fcc lattice type consisting of spheres ($r/a = 0.151$) of

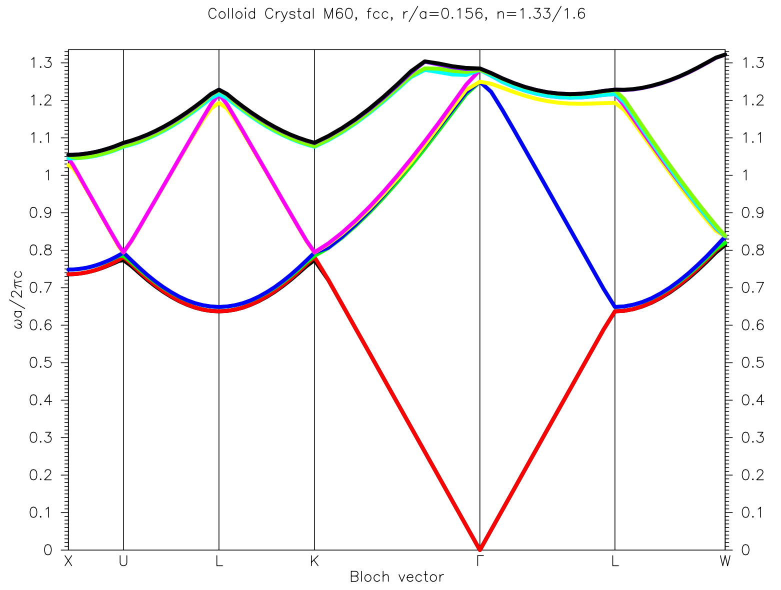

Figure 5.19: *Computed band structures for the M60 colloidal crystal*

n=1.59 (PS) in a ”backbone” of n=1.33 (H_2O). A set of 680 plane-waves was used in the calculations which should be accurate to around 1%. The resulting band structure diagram is shown in Fig. 5.19. At first glance it does not exhibit any dramatic features due to the low dielectric contrast. But upon magnifying the relevant part, i.e. the range from the L to the W point (as well as parts of the corresponding paths to the Γ-point to make the picture more interpretable), a general behavior of the bands very much resembling the one in diagram 5.17 appears (see fig.5.20). At the L-point a pseudo gap is apparent between the 2^{nd} and 3^{rd} band (band number 1, 2 and 3, 4 are degenerate respectively) at a value of $a/\lambda \approx 0.65$ on the normalized frequency scale. The absolute position of the pseudo gap depends of course on the lattice constant a. For a lattice constant with $a = 497\ nm$ the stop band is located at $\lambda = 765 \pm 8\ nm$. The error is due to uncertainties in the numerical calculation and the geometrically obtained radius was employed. This value agrees well to the observed transmission minimum at 760 nm.

This stop band however closes when approaching the W-point, although generally the degeneracy between the bands is lifted. The center position of the bands at the W-point is ~ 0.83 which corresponds to a wavelength of $\sim 598 \pm 6\ nm$. This does not match the observed value of 630 nm.

The similarity in the behavior of the simulated and measured results becomes even more striking when calculating the 1-dimensional DOS. It is plotted for the corresponding angles in Fig. 5.21. The solid and dashed lines refer to distinct polarization states (in this case assumed to be the odd and even bands). They are degenerate at the L-point but they form non-overlapping pseudo-gaps at the W-point. This could explain the observed gap there. Nevertheless the position is of course unchanged. Furthermore the light used to probe the samples was not polarized. Moreover does the 1-dimensional

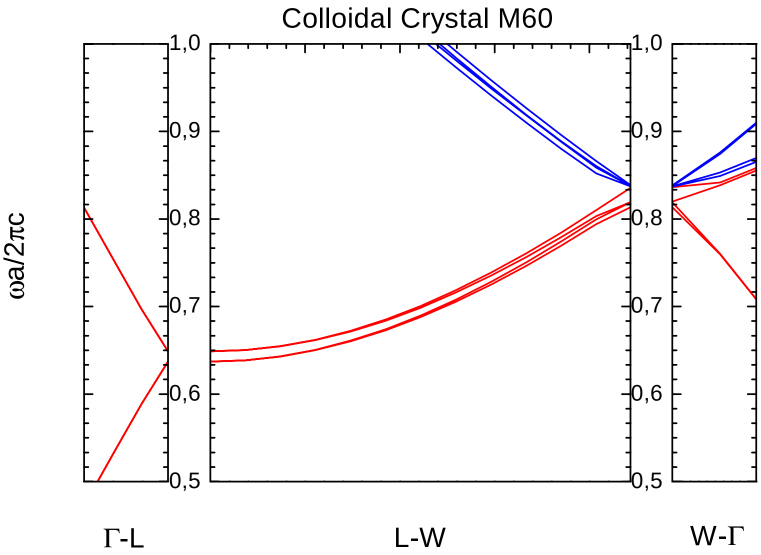

Figure 5.20: *Computed band structures for the M60 colloidal crystal*

photonic DOS only very qualitatively resemble the real transmission.

Therefore the structure of the colloidal crystals was implemented in the Tranfer-Matrix program and the actual transmission coefficients were calculated. The red and blue curve represent different polarization states again. They have the same transmission property at the L-point (since they 'see' the same crystal structure there). For other crystal directions marginal differences occur. As for the W-point a overlapping transmission minimum for both polarizations is present here. This is probably due to the many flat bands in this domain. But again the position of the gap at the W-point is around 590 *nm* which is considerably less than observed.

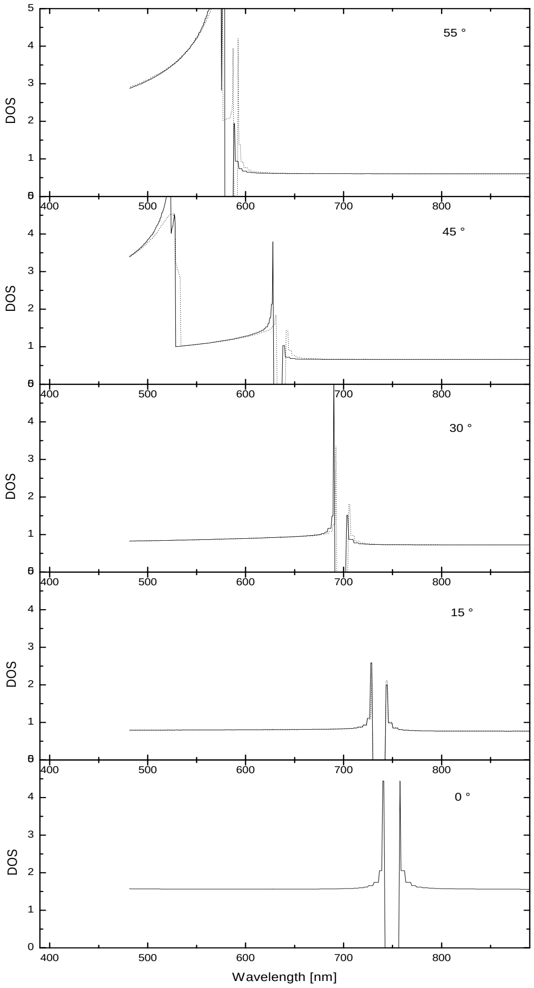

Figure 5.21: *Computed 1-dimensional photonic DOS for relevant directions*

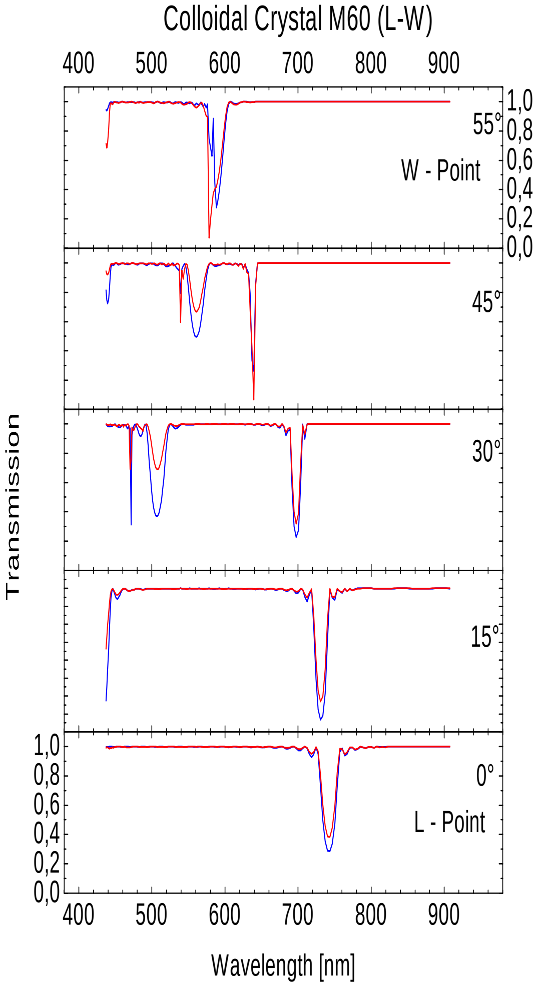

Figure 5.22: *Simulated transmission curves for M60 based on the Transfer-Matrix method*

5.4 Discussion

A solution to this mismatch at the W-point can be provided by looking at the transmission properties for other crystal axis. For instance the K- and U-point of the 1.BZ are located closer to the Γ-point and therefore have their pseudo-gaps at lower frequencies (the Γ-K and Γ-U axes in the 1.BZ are 1/8 of $2\pi/a$ shorter than the Γ-W axis [for a complete reference about the 1.BZ see appendix A]). When calculating the angular transmission dependency for the L-K and L-U ranges almost the same behavior is retained as for the L-W case. But the resulting minima at the K- and U-point are with a value of $\sim 620\ nm$ much closer to the experimentally observed wavelength of $\sim 630\ nm$. Therefore the rotation of the sample altered the crystal direction from Γ-L to Γ-K or Γ-U in my opinion. This seems plausible since the rotation axis is not uniquely determined by the initial Γ-L direction. By looking at the 1.BZ this can be clarified. All possible rotation axes lie on the hexagonal plane perpendicular to the Γ-L direction. Rotating the 1.BZ by 53.1° around an axis through two U- or K-points yields a W-Γ direction. On the other hand by rotating 27.3° around an axis through two W-points we get a K-Γ or U-Γ direction. No angles are stated in Fig. 5.23 and Fig. 5.24, because L-Γ-K and L-Γ-U embrace an angle of 27.3° , whereas the angle for L-Γ-W is 53.1° .

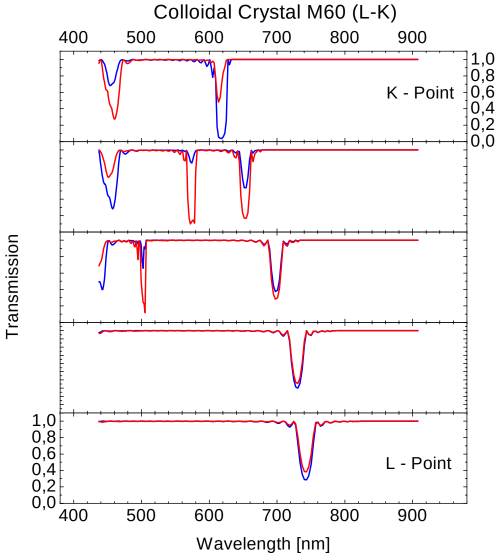

Figure 5.23: *Predicted transmission curves for the Γ-L to the Γ-K direction (M60)*

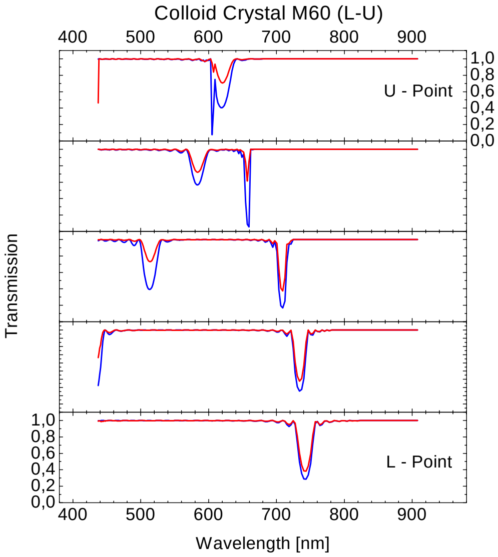

Figure 5.24: *Predicted transmission curves for the Γ-L to the Γ-U direction (M60)*

Moreover we should take into account the difference in incident angle on the glass capillary compared to the actual angle on the colloidal crystal. Applying Snell's law gives us:

$$\beta = \arcsin\left(\frac{1}{n}\sin(\alpha)\right) \tag{5.4}$$

Inserting a value of $\sim 50°$ (because $50°$ seems to be a symmetry point in Fig. 5.18) for α and the refractive index of PS ($n = 1.59$) (the refractive index of the glass would be in the same range) in eq. (5.4) we get $\sim 29°$. This is almost the exact angle of the K-Γ or U-Γ axes with the initial Γ-L direction (27.3°)! That seems to confirm my speculation.

The great advantage of those numerical simulations, besides interpretation and verification of experimental results, is the ease to alter parameters. Since there was no choice in material (e.g. particles with a higher refractive index) and lattice type (fcc) I tried to maximize the pseudo-gap at the L-point by optimizing the the filling fraction, i.e. the ratio r/a for the given configuration. As mentioned before the size of the particles can be selected relatively easily in the polymerization process. The result is shown in Fig. 5.25 and reveals a ration of $r/a \approx 0.28$ to be ideal in for this system. The gap could be increased this way by almost 3 times in size (from $\sim 1.5\%$ to $\sim 4.2\%$). Further ideas to increase the gap would be employing non-spherical objects (ellipsoids) as the motif in the crystal lattice. Unfortunately such systems are extremely difficult to synthesize on a monodispersed basis. Therefore an extension to polydispersed systems (spheres with different sizes), yielding for instance AB_2 lattice types, seems more feasible in the future [PKA97].

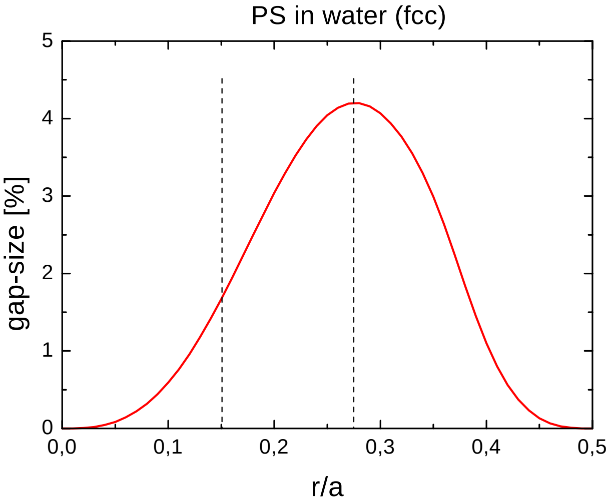

Figure 5.25: *Dependence of the pseudo-gap in the* Γ-L *direction for aqueous colloidal crystals* ($n_0 = 1.33$, $n_1 = 1.59$) *on the filling fraction (r/a) of the fcc lattice*

In a second study the effect of the hydrogel fixation on the optical properties of the colloidal crystals were investigated. Therefore two sample (M43 and M43fix, both with 4.3-wt% PS. M43 was fixated by the hydrogel matrix) were prepared and characterized by M. Soddemann. Their transmission curves are compared in Fig. 5.26 and Fig. 5.27.

It is remarkable that the fixated sample shows much more pronounced peaks. This can be attributed to a better long range periodicity in the crystal which solely affects the intensity of the peaks. In fact the unfixated crystal M43 seems to 'melt' in the

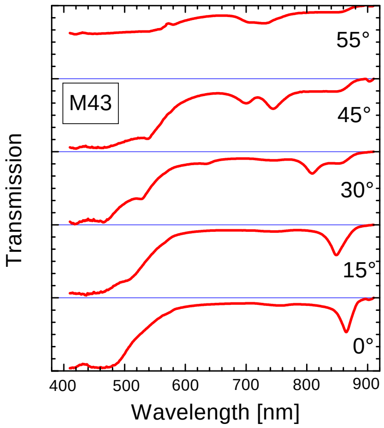

Figure 5.26: *Angular dependence of the transmission curves for the unfixated crystal M43*

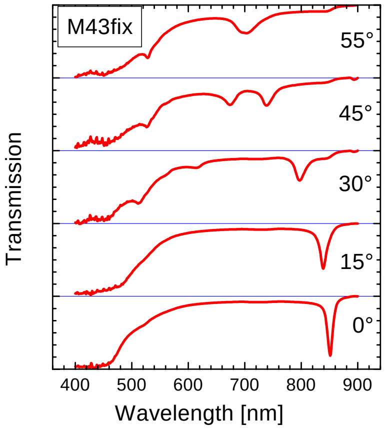

Figure 5.27: *Angular dependence of the transmission curves for the fixated crystal M43fix*

measurement at 55° in Fig. 5.26. Within experimental accuracy the position of the peak was confirmed to remain the same. With the theoretical simulations it was confirmed that the slightly increased refractive index of the backbone (n=1.34) due the infiltration with the hydrogel had no significant impact, but is generally a measure for the long range periodicity. The intensity of the peaks could not be accounted for with the simulation.

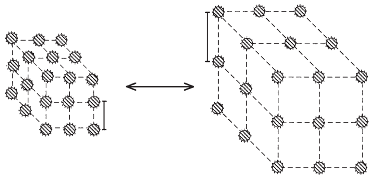

Figure 5.28: *Hydrogel fixated colloidal crystal as a sensing device*

A highly interesting feature of fixated colloidal crystals in general is the sensitivity of the hydrogel to environmental changes like temperature or chemical properties like acidity. Upon a variation of such a parameter the matrix expands or shrinks and mediates a change in lattice constant. Consequently the optical properties of the crystal change, i.e. the diffraction peak shifts in wavelength. Such systems could conveniently be applied as sensing devices [HA97].

Chapter 6

Photonic Crystals in the THz Frequency Range

Besides theoretical and numerical simulations my interest in photonic crystals focuses on the experimental side. Quite generally I think of it as a good idea when theory and experiment go hand in hand. This is especially true in physics.

In the research group of Prof. Hanspeter Helm (Department of molecular and optical physics) in Freiburg the 'squad' around Dr. Peter Uhd Jepsen, which I was part of, has great expertise in the creation and detection of THz radiation. The frequency range between 0.1 … 3 THz is generally termed THz regime. THz radiation is usually applied in Time-Domain Spectroscopy experiments (THz-TDS). With such experiments it is possible to measure both amplitude and phase of the detected electromagnetic wave.

Coincidentally these features of THz-TDS are invaluable tools to analyze optical properties of photonic crystals. Ideal photonic crystals possess a periodicity in dielectric constant on the order of the wavelength to be affected. Therefore structure sizes desirable in the THz-regime are on the scale of $\sim 100\ \mu m$. This considerably eases the fabrication compared to structures in the IR or optical region. Nevertheless the findings can be extended to any wavelength due to the scale invariance of Maxwell's equations.

Furthermore a phase-sensitive detection permits the analysis of the wavelength dependent phase delay and therefore measurements of the phase velocity. This is the only way to directly probe the bands of a band structure diagram and draw conclusions about their coupling strength [RAM$^+$93].

In section 6.1 I will very briefly present the experimental requisites of THz-TDS before showing the outcomes for two specific examples in sections 6.2 and 6.3. Of course both are backed and interpreted by simulations.

Remark: Layered (rectangular or square) bars were termed *'Lincoln Log'* and layered (circular) rods were named *'Woodpile'* in my documentation, although both names are common for both types. Fig. 6.1 shows a schematic drawing of this kind of crystal structures. This is just for clarity reasons to point out the difference and none of these depicted structures were actually used. Both possibilities, a Lincoln-Log and a

Woodpile structure were always taken into account in the subsequent simulations in this chapter, but never showed significant differences.

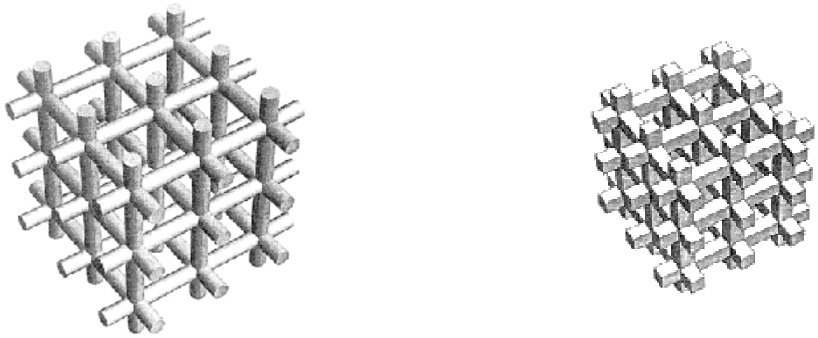

Figure 6.1: *My terminology schematically: Woodpile (left) and Lincoln-Log (right) structures [Hau94]*

6.1 Experimental Setup

Experiments involving THz radiation became some sort of standard in our research group over the past years. Therefore I will not go into too much detail here.

The field was introduced by Grischkowsky [Gri93] and co-workers in 1989. A typical experimental setup, as employed in our experiments is shown in Fig. 6.2.

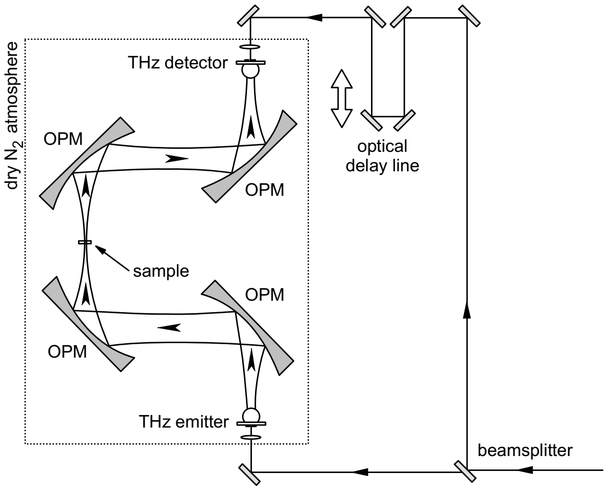

Figure 6.2: *Outline of a classical setup of a THz-TDS experiment* ©*P. Uhd Jepsen*

On the lower right corner of Fig. 6.2 a femtosecond (fs)-laser beam is incident on a beamsplitter. In the conducted experiments the fs-laser beam was produced by a home-built self-modelocked Ti:Sapphire system. Pulse duration was $\sim$ 40 fs with an average power of $\sim$ 100 mW at a repetition rate of 80 MHz. After the beamsplitter one portion of the beam (emitter-beam) is then focused onto a photo-conductive THz emitter, consisting of a semiconductor material (GaAs) with two conductive paths separated by 50 μm. A bias (40 V) is applied to the antenna so the static electric field between the electrodes accelerates free charges created by the focused fs-pulse in between. The accelerated electrons function as a radiating dipole and emit a single-cycle THz pulse of less than 1 ps duration. The beam of THz pulses is widened and collimated by a spherical Si-lens atop of the emitter and a paraboloidal mirror respectively. A subsequent paraboloidal mirror focuses the beam onto the sample. The same optical elements (inverse order now) guide and focus the beam after the sample onto a photo-conductive detector. This detector functions according to the same principle as the emitter. Except that no bias is applied here but the $\boldsymbol{E}$-field of the THz pulse is responsible for the transport of free carriers towards the electrodes on the semiconductor (SiliconOnSapphire SOS) substrate. The free carriers are again created by means of focusing the second portion of the fs-beam onto the detector. It is crucial to ensure a spatial and temporal overlap of the two pulses on the detector. By scanning the delay line in the detector-beam the temporal shape of the single-cycle THz pulse is recorded. The THz pulse is ensured to travel in a dry Nitrogen atmosphere, since water vapor in air considerably absorbs THz radiation.

The information about the sample contained in the pulse can be extracted by Fourier-transforming it from time- to frequency-space. By comparison to the spectrum of the original pulse this reveals the spectral amplitude and phase behavior in transmission of the sample. A typical free space THz pulse along with its corresponding spectrum is shown in Fig. 6.3.

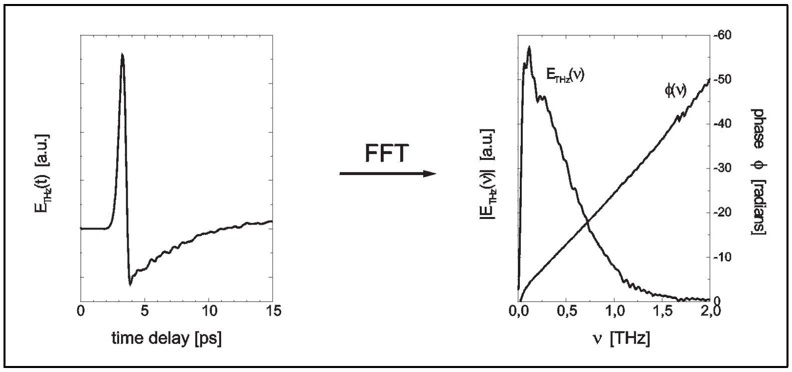

Figure 6.3: *Extracting the amplitude and phase of the electromagnetic field via Fourier-transformation [Win99]*

The phase-recovering Fourier-transformation is usually performed with a Turbo Pascal program written by P. Uhd Jepsen. This yields directly the frequency dependent absorption coefficient $\alpha(\omega)$ and index of refraction $n(\omega)$. As is the general case with FT spectroscopy the resolution of the spectrum is determined by the scan length and the maximal detectable frequency is determined by the step size.

6.2 Alumina 'Woodpile' Structure

In the scope of his Ph.D. thesis C Winnewisser characterized transmission properties of frequency selective surfaces or dichroic filters, sometimes simply called 'strainers'.

These are thin slabs of 2-dimensional periodically (in the slab plane) structures (e.g. holes), which serve as band-pass filters in the THz-frequency range. Their theoretical treatment is based on a waveguide interpretation. Although their structure is related to 2-dimensional photonic crystals, there is a fundamental difference in the fact that dichroic filters do not possess periodicity of the dielectric constant in propagation direction.

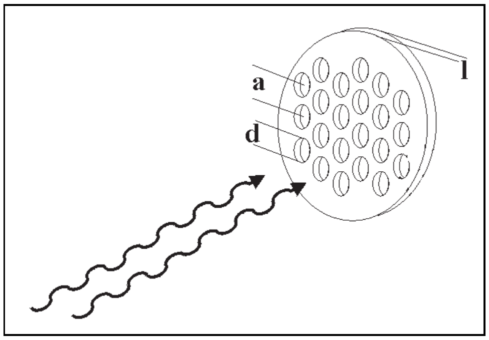

Figure 6.4: *Dichroic filters characterized by C. Winnewisser [Win99]*

To extend his investigations to 3-dimensional structures C. Winnewisser collaborated with M. Stuke from the MPI in Göttingen. M. Stuke and his co-workers succeeded to grow 3-dimensional micro-structures by Laser Chemical Vapor Deposition LCVD [LS95]. In a vapor cell containing the precursors and mounted on a computer-controlled xyz-translation stage, two laser beams were focused. At the combined focus Alumina (Al_2O_3) solidified from the gas phase. The growth of the micro-structure could be guided in a controlled way. In this fashion crystals consisting of layers of Alumina rods (diameter: 40 μm) displaced by 133 μm were fabricated. The second layer of rods was rotated by 90° and centered between two rods of the first layer. A drawing is shown in Fig. 6.6.

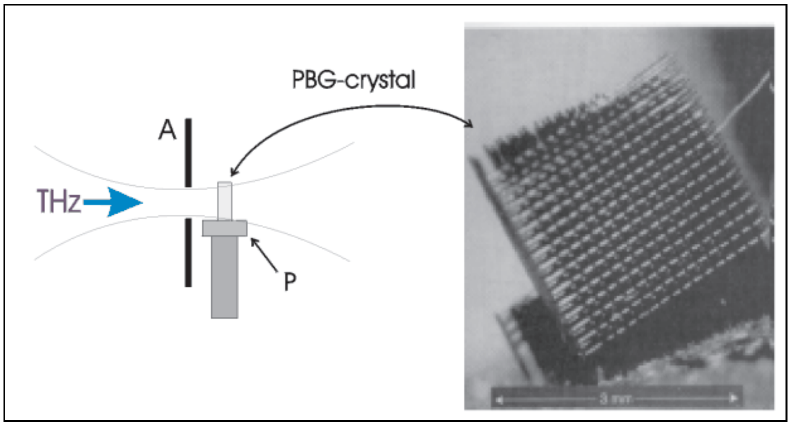

Figure 6.5: *The experimental configuration (left) and an image of the analyzed photonic crystal (right) [Win99]*

The experimental configuration is depicted in Fig. 6.5. An aperture (A) was used in order to limit the THz beam to the size of the crystal (3 mm). However the crystal was very small and could not be positioned closely enough to the aperture due to its mounting on a socket (P).

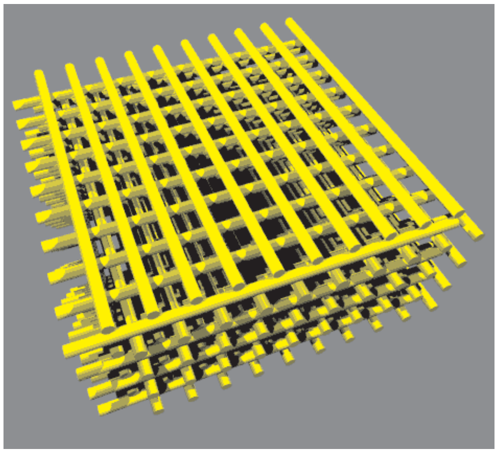

Figure 6.6: *Povray image of the Alumina woodpile structure under study*

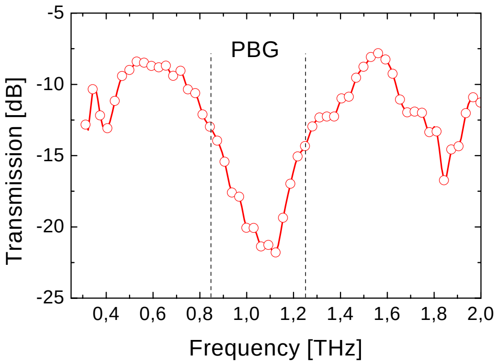

Figure 6.7: *The experimentally recorded transmission spectrum*

The resulting transmission spectra is shown in Fig. 6.7. The overall transmission was very low and only a broad smeared minimum (∼10dB dip) is revealed at around 1 THz. At the time of the experiment this was not considered a convincing photonic band gap. Moreover did Prof. Stuke claim a band gap around 2 THz in a science-paper [WLM+97]. Due to this unclarities and lacking theoretical support further experiments were discarded.

Unfortunately these experiments were long past when I gained experience in theoretically simulating optical properties of photonic crystals. Nevertheless I implemented the above described woodpile structure to the PWEM and Transfer-Matrix method. From a crystallographic point of view the structure is built from cross-like shapes in a body-centered-tetragonal (bct) lattice type. That is because the separation in x- and y-direction (133 μm) is smaller than the lattice constant in z-direction ($4 * 40\,\mu m = 160\ \mu m$). The conventional and primitive unit cell for the bct-lattice (see Fig. 6.8) along with its corresponding 1.BZ (see Fig. 6.9), which is basically a compressed fcc BZ are shown below.

The band structure calculations were performed with a set of 1458 plane-waves and yielded the diagram depicted in Fig. 6.10. The refractive index of Alumina at THz frequencies was assumed to be the average (n=3.25) of two possible indices (n=3.08 and n=3.42) for the ordinary and extraordinary crystal axis. This seems appropriate since the LCVDed rods were randomly oriented Al_2O_3 crystals. A rather big ($\sim 15\%$) complete band gap is found to be centered at 0.96 THz. The calculation of the complete photonic DOS (top fraction in Fig. 6.11 confirms this finding).

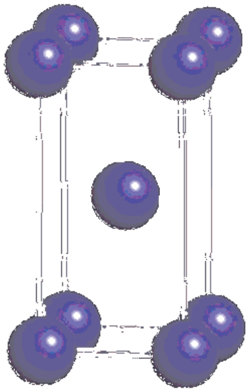

Figure 6.8: *A body-centered-tetragonal (bct) unit cell*

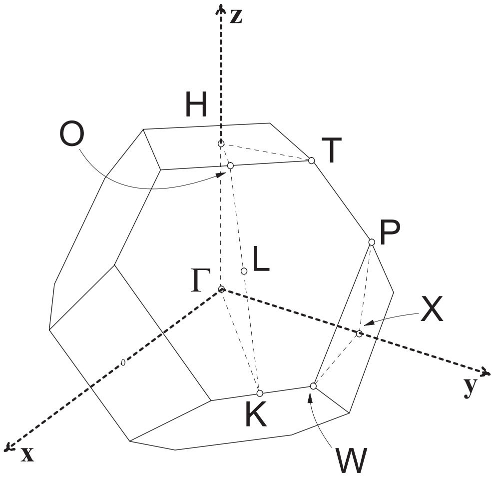

Figure 6.9: *The 1.BZ of the bct-lattice with relevant symmetry points*

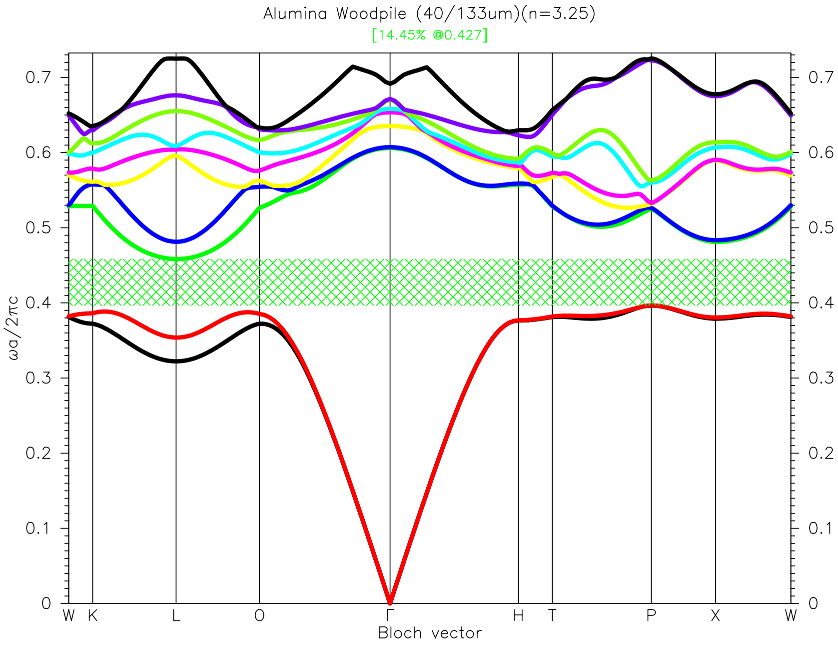

Figure 6.10: *Calculated band structure diagram for the Alumina woodpile structure*

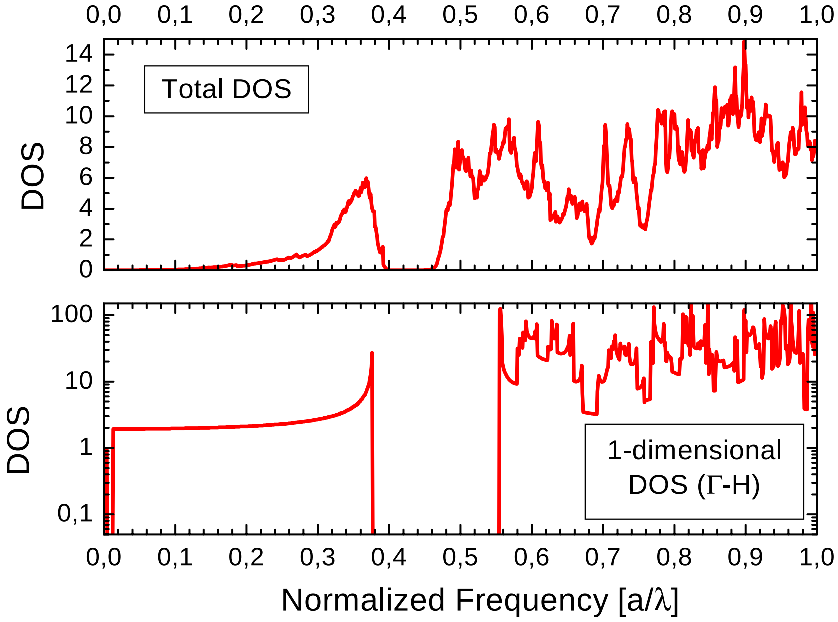

Figure 6.11: *Total (top) and projected (on Γ-H) photonic density of states*

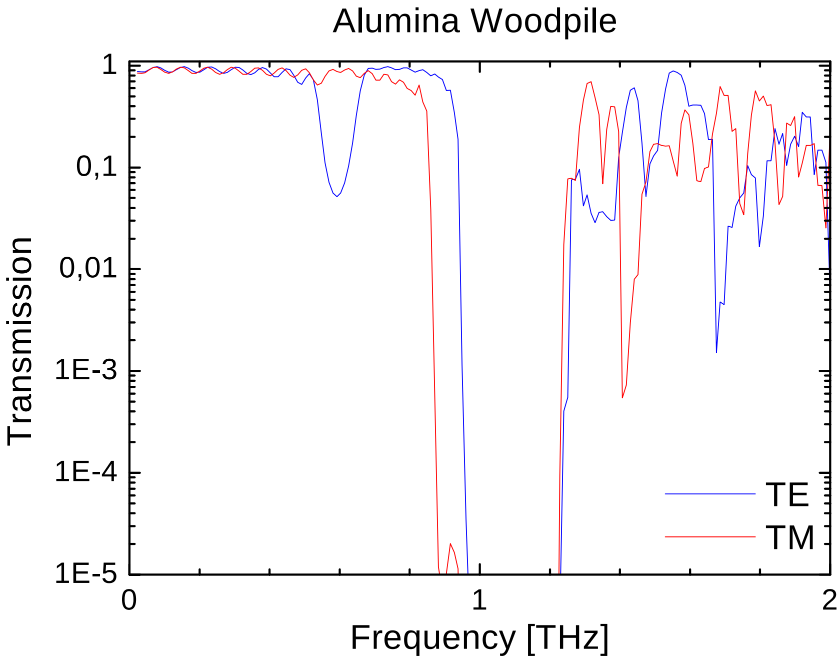

Figure 6.12: *The transmission spectra for two distinct polarization states as obtained by the Transfer-Matrix method*

The 1-dimensional photonic DOS in Γ-H direction is plotted in Fig. 6.11 (solid line), since this was the direction in which the crystal was probed. The band gap in this particular direction is much larger (rel. size ∼ 40%) and centered at 1.05 THz . Very good agreement is evident by comparing these values to the experimentally observed gap.

Finally the actual transmission curves in Γ-H direction are calculated by means of the Transfer-Matrix method (see Fig. 6.12). The large band gap centered around 1 THz is re-confirmed. Furthermore the overall transmission behavior strongly resembles the measured curve. Please note that the numerical accuracy for higher frequencies above the fundamental gap is decreasing.

In conclusion it was exciting to confirm these results measured by C. Winnewisser and give them the theoretical support they deserve. Unfortunately these experiments were not carried on any further but may be pursued in the future in Freiburg. The combination of the LCVD technique to fabricate photonic crystals of desired structures and the THz-TDS to characterize and probe them seems very promising.

6.3 Rapid Prototyped PE Structures

In the progress of my thesis I decided to conduct experiments investigating refraction properties of photonic crystals myself. The advantages of the existing THz-TDS utilities were already pointed out. In order to get angle-resolved measurements a slightly modified version of the THz spectrometer was built. A schematic drawing of it is shown in Fig. 6.13. The modifications to the original setup comprise the usage of just one pair of paraboloidal mirrors, which focus the THz beam onto the photonic crystal slab. Furthermore the detector mount was re-designed to permit position dependent measurements by translating it laterally at the immediate backside of the sample. It was intended to mount the entity of sample and detection system on a rotation stage in order to vary the incident angle on the photonic crystal. Unfortunately the limited time did not permit to accomplish this last step.

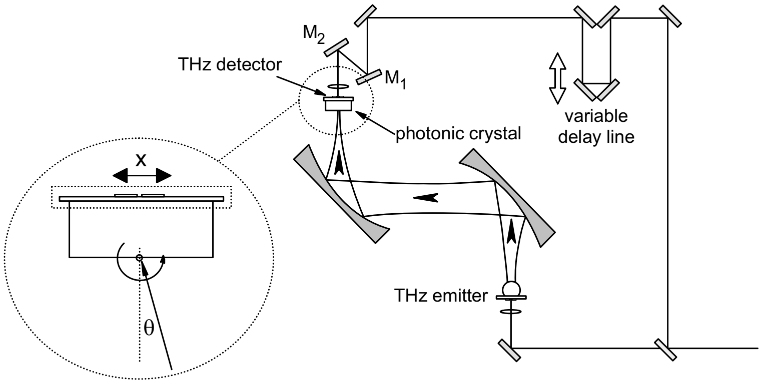

Figure 6.13: *The slightly modified THz-TDS setup to investigate superprism effects* ©P. Uhd Jepsen

Suitable crystals for the THz frequency regime can quite easily be fabricated mechanically. But our initial plan to drill ordered holes in materials such as HDPE or TPX failed since the required precision ($r = 100\ \mu m$, $a = 270\ \mu m \rightarrow f \approx 50\%$ [optimized for TE-gap in triangular lattice]) could not be achieved. Further plans to arrange fibers, possible with a core structure (e.g. being hollow or layered) or having non-spherical cross-section (e.g. hollow square fibers), were postponed for the benefit of rapid prototyped 3-dimensional structures. These structure are fabricated by R. Landers at the Freiburger Materialforschungszentrum FMF on a 3D plotting device. The 3D plotter is shown in action in Fig. 6.14. A heated reservoir containing the liquid polymer is mounted to a computer controlled xyz-translation stage. The polymer emanates through a nozzle into a tank of glycerin kept a certain constant temperature in order to control the solidifying process of the polymer. By moving the nozzle (and the reservoir) 3-dimensional structures can be written. With this method layered structures of polymer skeins ($r = 230\ \mu m$) in a cubic lattice ($a = 900\ \mu m$) were grown. We used polyethylen PE (n=1.5) as the polymer material in this study .

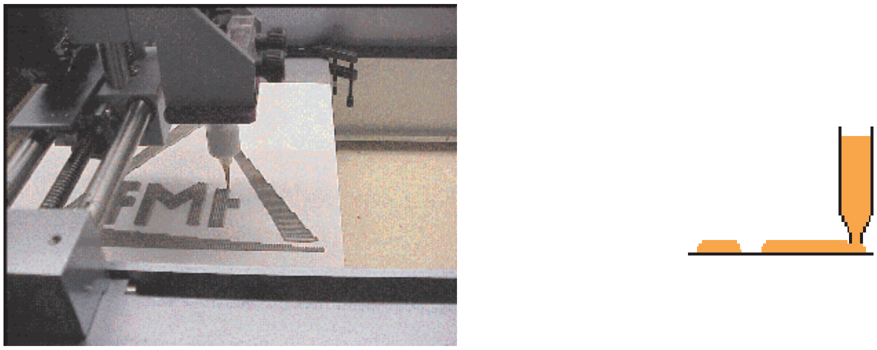

Figure 6.14: *The 3D plotter in action (left) and a schematic drawing (right)*

Fig. 6.1 shows a schematic drawing of this woodpile structure. The possibility of a Lincoln Log structure was also taken into account for the numerical simulations but showed no significant differences.

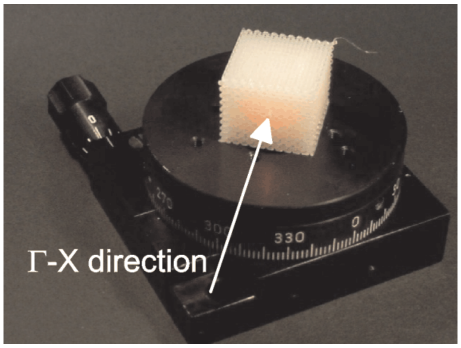

Figure 6.15: *A photograph of the PE woodpile structure*

A cubic lattice consisting of cross-like structures of PE (n=1.54) was implemented for the calculations. The space lattice and 1.BZ of the cubic lattice is shown in Fig. 6.16. Results obtained with the PWEM, i.e. band structure diagram and photonic DOS are plotted in Fig. 6.17 and Fig. 6.18 respectively. Due to the low dielectric contrast only pseudo-gaps for the respective crystal axes are present.

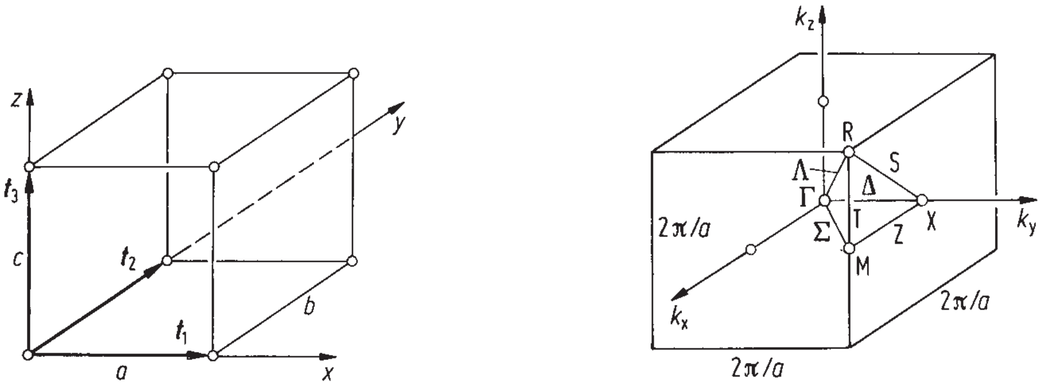

Figure 6.16: *Simple cubic space lattice (left) and corresponding 1.BZ (right)*

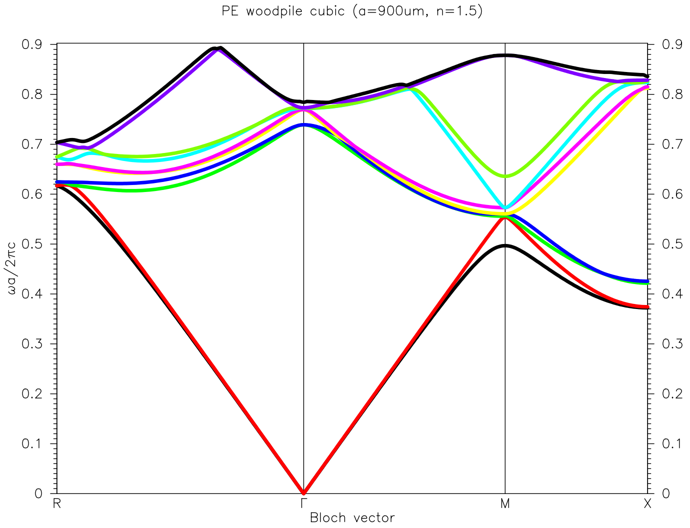

Figure 6.17: *Band structure diagram for the PE woodpile crystal*

The experiments conducted were not carried out under N_2 atmosphere. Therefore water absorption lines from water vapor in air are present in the reference pulse spectrum. The temporal shape and spectrum of reference and sample pulse are plotted in Fig. 6.19. The intensity of the pulse probing the photonic crystal slab is overall appreciably lower than that of the free pulse. This is mainly due to the lack of a Si-lens focusing the THz pulse onto the detector.

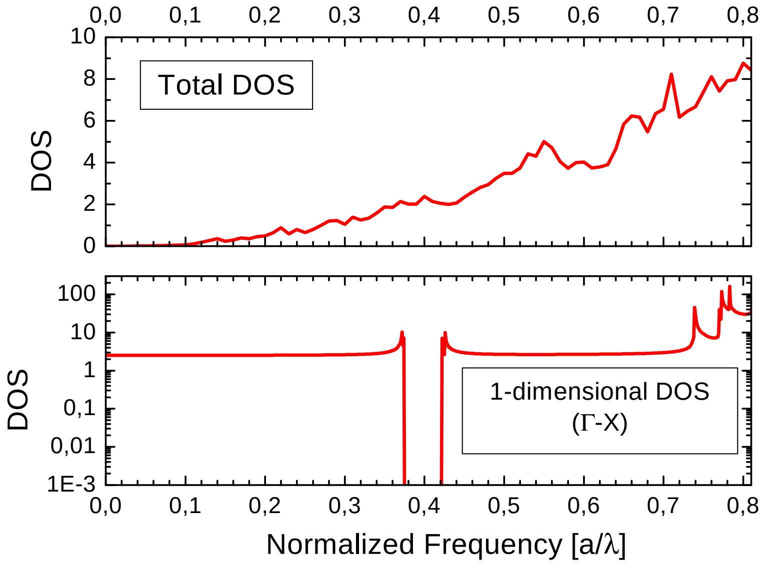

Figure 6.18: *Calculated total (top) and 1-dimensional (bottom) photonic DOS for the PE structure*

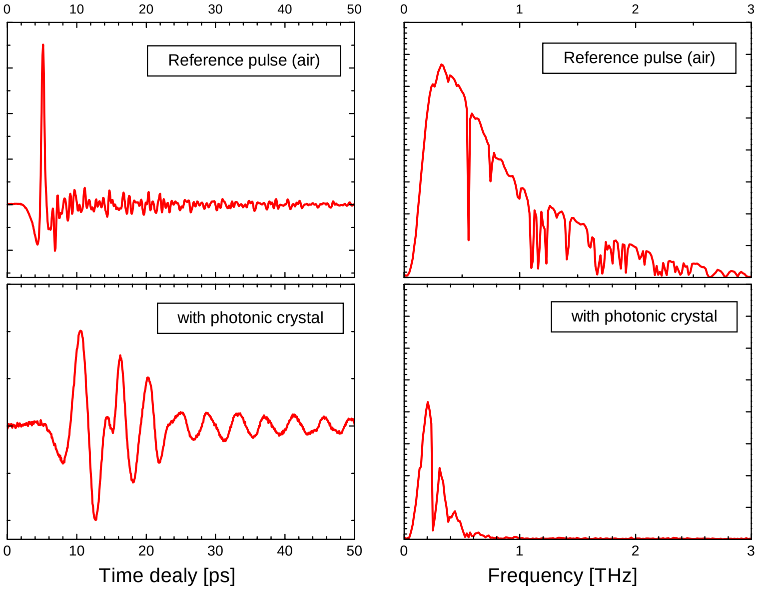

Figure 6.19: *Reference pulse in air and the corresponding spectrum with the rotational water absorption lines in the top part. Bottom fraction shows the (magnified) pulse after probing the photonic crystal slab and the corresponding spectrum (same scale as free spectrum)*

The resulting relative transmission spectrum for the Γ-X direction of the crystal exhibits a clear gap at $\sim 0.26\ THz$ (see Fig. 6.20[center]). The simulated transmission curve by the Tranfer-Matrix method is also shown in Fig. 6.20[top]. It agrees well with the features of the measured curve. Only the actual intensity distribution can not be accounted for. We could attribute this to a possible absorption in the material induced be the plotting mechanism in glycerin, since bulk PE shows no absorption. But probably a non-perfect periodicity and low aspect ratio of the crystal pose more important factors negatively affecting the transmission.

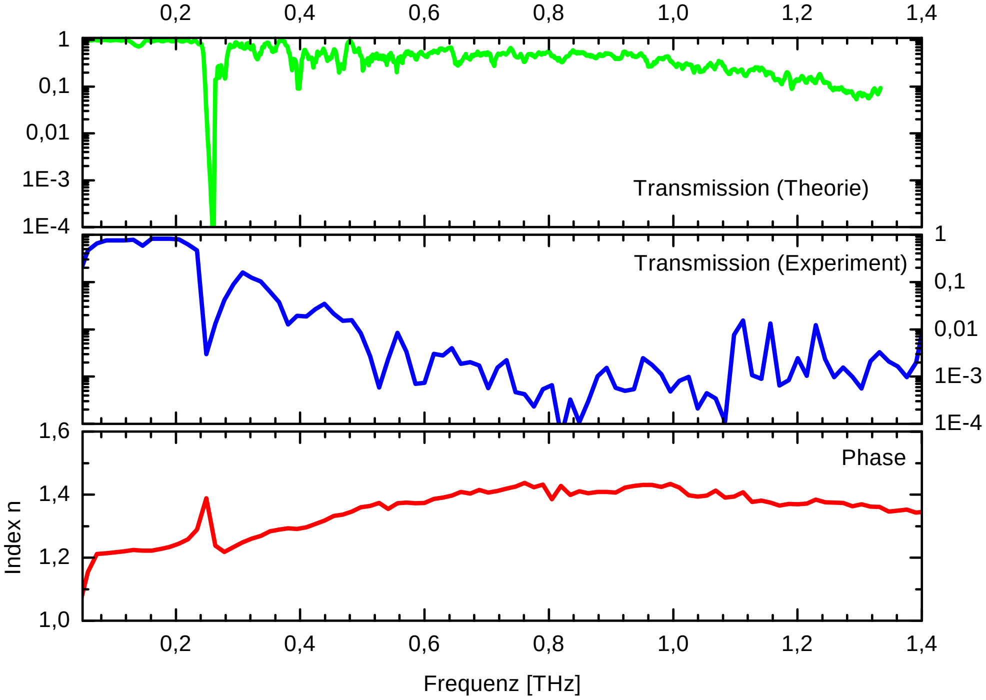

Figure 6.20: *The final results to date for the PE photonic crystal: simulated (top) and measured (centered) transmission. The bottom part shows the extracted index*

The most exciting feature however is shown in Fig. 6.20[bottom]. Here the resulting effective index of refraction is plotted, extracted from the recorded phase information (ϕ) and the known thickness of the slab (L).

$$n_{eff}(\omega) = \frac{c\,\phi}{\omega L} + 1, \tag{6.1}$$

It is evident that the transmission minimum corresponds to an increase in refractive index, i.e. decrease in phase velocity: $v_{phase} = c/n_{eff}$. In principle the band structure could also be recovered with this sort of analysis via:

$$k(\omega) = \frac{\omega n(\omega)}{c} \tag{6.2}$$

and be compared to the theoretically calculated one. In this fashion uncoupled bands can be identified [RAM+93].

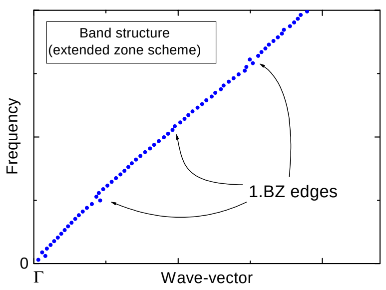

Figure 6.21: *Recovered band structure in an extended zone scheme*

However the features we observed in this recovered band structure diagram are not very strong. Refined measurements would be required to increase the resolution.

In conclusion it has been shown that these rapid prototyped structures can well be applied as photonic crystals in the THz range. Additional, more sophisticated crystals could be fabricated and employed. For instance mixing a high index powder to the liquid PE when it is plotted should increase the dielectric contrast of our crystals. Thus we expect more pronounced features. Furthermore the strand size and lattice constant can be reduced in order to create band gaps at higher frequencies.

If the quality of these structures, i.e. the long range periodicity can be improved, then even measurements investigating the refraction properties of these crystals should be possible with THz-TDS.

Chapter 7

Conclusion

This thesis covers a broad range of numerical simulations and experimental analysis of optical properties of photonic crystals.

A general outline of the topic photonic crystals was first presented in order to establish a firm basis of the theoretical background. It is my hope that this chapter serves as an educational introduction to the topic of photonic crystals. In the second part I describe my efforts to gain expertise in programming computer codes for simulations and to perceive the fundamental coherences in the different aspects of photonic crystals. Chapter III serves as a map of the photonic crystal landscape easing the orientation and the identification of basic parameters and dependencies which govern the properties of photonic crystals.

Ultra-refractive effects are the topic of chapter IV. This study was exclusively carried out at the University of Toronto in the research group of Prof. Sajeev John. Our initial attempt to verify existing superprism work (by H. Kosaka, NEC-Laboratories, Japan) was only partially successful. However the investigation of refraction properties for 2-dimensional crystals led us to predict remarkable features and design novel experiments. Our predicted results have yet to be confirmed. Chapter V reports my theoretical simulations of angular dependent transmission characteristics of colloidal crystals. My findings confirm the measurements carried out at in the group of Prof. W. Richtering, department of physic chemistry in Kiel (formerly Freiburg) very well. Chapter VI reports experiments I carried out in the THz frequency range. These results were interpreted in theoretical models. Similar simulations were applied to previous data obtained in Freiburg on a 3-dimensional photonic crystal. This crystal was fabricated at the MPI Göttingen by Prof. M. Stuke from laser-assisted chemical vapor deposition (LCVD) of Alumina. There is good agreement between the experimental and numerical findings for all these experiments.

All in all this has been a highly instructive year for me and I am very grateful to all the people I could interact with.

Bibliography

[AM76] N. W. Ashcroft and N. D. Mermin, *Solid state physics*, Saunders College Publishers, Orlando, Florida, 1976.

[BCG$^+$00] A. Blanco, E. Chomski, S. Grabtchak, M. Ibisate, S. John, S. W. Leonard, C. Lopez, F. Meseguer, H. Miguez, J. P. Mondia, G. A. Ozin, O. Toader, and H. M. van Driel, *Large-scale synthesis of a silicon photonic crystal with a complete three-dimensional bandgap near 1.5 micrometres*, Nature **405** (2000), 437.

[Ber99] V. Berger, *From photonic band gaps to refractive index engineering*, Opt. Mater. **11** (1999), 131–142.

[BJ99] K. Busch and S. John, *Liquid-crystal photonic band-gap-materials: The tuneable electromagnetic vaccum*, Phys. Rev. Lett. **83** (1999), 967–970.

[BVJS00] K. Busch, N. Vats, S. John, and B. C. Sanders, *Radiating dipoles in photonic crystals*, Phys. Rev. E **62** (2000), 4251–4260.

[BW75] M. Born and E. Wolf, *Principles of optics*, Pergamon Press, Frankfurt, 1975.

[CSH$^+$00] M. Campbell, D. N. Sharp, M. T. Harrison, R. G. Denning, and A. J. Turberfield, *Fabrication of photonic crystals for the visible spectrum by holographic lithography*, Nature **404** (2000), 53–56.

[DB94] J. P. Dowling and C. M. Bowden, *Anomalous index of refraction in photonic bandgap materials*, J. Mod. Opt. **41** (1994), no. 2, 345–351.

[ET95] J. M. Elson and P. Tran, *Dispersion in photonic media and diffraction from gratings: a different modal expansion for the r-matrix propagation technique*, J. Opt. Soc. Am. A **12** (1995), no. 8, 1765–1771.

[ET96] J. M. Elson and P. Tran, *Coupled-mode calculation with the r-matrix propagator for the dispersion of surface waves on a truncated photonic crystal*, J. Phys. C **54** (1996), 1711.

[ETM99] S. Enoch, G. Tayeb, and D. Maystre, *Numerical evidence of ultrarefractive optics in photonic crystals*, Opt. Comm. **161** (1999), 171–176.

[FG97] A. Figotin and Y. A. Godin, *The computation of spectra of some 2d photonic crystals*, J. Comput. Phys. **136** (1997), 585–598.

[FGV98] A. Figotin, Y. A. Godin, and I. Vitebsby, *Two-dimensional tunable photonic crystals*, Phys. Rev. B **57** (1998), 2841–2848.

[FVJ96] S. Fan, P. R. Villeneuve, and J. P. Joannoploulos, *Large omnidirectional band gaps in metallodielectric photonic crystals*, Phys. Rev. B **54** (1996), 11245–11251.

[GET00] B. Gralak, S. Enoch, and G. Tayeb, *Anomalous refractive properties of photonic crystals*, J. Opt. Soc. Am. A **17** (2000), no. 6, 1012–1020.

[Gra98] O. Graydon, *Nature's nanostructures colour wings and stones*, OLE (1998), 31–36.

[Gri93] D. Grischkowsky, *Nonlinear generation of sub-ps pulses of thz electromagnetic radiation by opto-electronics-applications to time-domain spectroscopy*, Frontiers in Nonlinear Optics: The Sergei Akhmanov Memorial Volume (Bristol & Philadelphia) (H. Walther, N. Koroteev, and M. O. Scully, eds.), vol. The Sergei Akhmanov Memorial Volume, Institute of Physics Publishing, Bristol & Philadelphia, frontiers in nonlinear optics ed., 1993, ISBN: 0-7503-0218-6, pp. 196–227.

[HA97] J. H. Holtz and S. A. Asher, *Polymerized colloidal crystal hydrogel films as intelligent chemical sensing materials*, Nature **389** (1997), 829–832.

[Hau94] J. W. Haus, *A brief review of theoretical results for photonic band structures*, jmo **41** (1994), 195–207.

[HCS90] K. .M. Ho, C. T. Chan, and C. .M. Soukoulis, *Existence of a photonic gap in periodic dielectric structures*, Phys. Rev. Lett. **65** (1990), 3152–3155.

[IVSL99] A. Imhof, W. L. Vos, R. Sprik, and A. Lagendijk, *Large dispersive effects near the band edges of photonic crystals*, Phys. Rev. Lett. **83** (1999), 2942–2945.

[JB99] S. John and K. Busch, *Photonic band gap formation and tunability in certain self-organizing systems*, draft, June 1999.

[JMW95] J. D. Joannopoulos, R. D. Meade, and J. N. Winn, *Photonic crystals: Molding the flow of light*, Princeton University Press, New Jersey, 1995.

[Joh87] S. John, *Strong localization of photons in certain disordered dielectric superlattices*, Phys. Rev. Lett. **58** (1987), 2486–2489.

[Kit99] C. Kittel, *Einführung in die festkörperphysik*, Oldenbourg, Muenchen, 1999.

[KKT+98] H. Kosaka, T. Kawashima, A. Tomita, M. Notomi, T. Tamamura, T. Sato, and S. Kawakami, *Superprism phenomena in photonic crystals*, Phys. Rev. B **58** (1998), 10096–10099.

[KKT+99a] H. Kosaka, T. Kawashima, A. Tomita, M. Notomi, T. Tamamura, T. Sato, and S. Kawakami, *Self-collimating phenomena in photonic crystals*, Appl. Phys. Lett. **74** (1999), 1212–1214.

[KKT+99b] H. Kosaka, T. Kawashima, A. Tomita, M. Notomi, T. Tamamura, T. Sato, and S. Kawakami, *Photonic crystals for micro lightwave circuits using wavelength-dependent angular beam steering*, Appl. Phys. Lett. **74** (1999), 1370–1372.

[KKT+99c] H. Kosaka, T. Kawashima, A. Tomita, M. Notomi, T. Tamamura, T. Sato, and S. Kawakami, *Superprism phenomena in photonic crystals: Toward microscale lightwave circuits*, IEEE J. Ligthwave Tech. **17** (1999), 2032–2038.

[LCH+98] S. Y. Lin, E. Chow, V. Hietala, P. R. Villeneuve, and J. D. Joannopoulos, *Experimental demonstration of guiding and bending of electromagnetic waves in a photonic crystal*, Science **282** (1998), 274–276.

[LHWJ96] S-Y. Lin, V. M. Hietala, L. Wang, and E. D. Jones, *Highly dispersive photonic band-gap prism*, Opt. Lett. **21** (1996), no. 21, 1771–1773.

[LL90] K. M. Leung and Y. F. Liu, *Full vector wave calculation of photonic band structures in face-centered-cubic dielectric media*, Phys. Rev. Lett. **65** (1990), 2646–2649.

[LS95] O. Lehmann and M. Stuke, *Laser-driven movement of three-dimensional microstructures generated by laser rapid prototyping*, Science **270** (1995), 1644–1646.

[MBRJ91] R. D. Meade, K. D. Brommer, A. M. Rappe, and J. D. Joannopolous, *Electromagnetic bloch waves at the surface of a photonic crystal*, Phys. Rev. B **44** (1991), 10961–10964.

[OT96a] K. Ohtaka and Y. Tanabe, *Photonic bands using vector spherical waves. i. various properties of bloch electric fields and heavy photons*, J. Phys. Soc. Jpn **65** (1996), no. 7, 2265–2275.

[OT96b] K. Ohtaka and Y. Tanabe, *Photonic bands using vector spherical waves. ii. reflectivity, coherence and local field*, J. Phys. Soc. Jpn **65** (1996), no. 7, 2276–2284.

[OT96c] K. Ohtaka and Y. Tanabe, *Photonic bands using vector spherical waves. iii. group-theoretical treatment*, J. Phys. Soc. Jpn **65** (1996), no. 8, 2670–2684.

[OUT96] K. Ohtaka, T. Ueta, and Y. Tanabe, *Photonic bands using vector spherical waves. iv. analogy of optics of photonic crystals to that of anisotropic crystals*, J. Phys. Soc. Jpn **65** (1996), no. 9, 3068–3077.

[Pen94] J. B. Pendry, *Photonic band structure*, J. Mod. Opt. **41** (1994), 209–229.

[PKA97] G. Pan, R. Kesavamoorthy, and S. A. Asher, *Optically nonlinear bragg diffraction nanosecond optical switches*, Phys. Rev. Lett. **78** (1997), 3860–3863.

[PM92] J. B. Pendry and A. MacKinnon, *Calculation of photonic dispersion relations*, Phys. Rev. Lett. **69** (1992), 2772–2775.

[PMM$^+$01] A. R. Parker, R. C. McPhedran, D. R. McKenzie, L. C. Botten, and N.-A. P. Nicorovici, *Aphrodite's iridescence*, Nature **409** (2001), 36.

[RAM$^+$93] W. M. Robertson, G. Arjavalingam, R. D. Meade, K. .D. Brommer, A. .M. Rappe, and J. D. Joannopoulos, *Measurement of the photon dispersion relation in two-dimensional ordered dielectric arrays*, J. Opt. Soc. Am. B **10** (1993), no. 2, 322–327.

[RJ96] A. Reineix and B. Jecko, *A new photonic band gap equivalent model using finite difference time domain method*, Ann. Telecommun. **51** (1996), 656.

[Roe00] H. Roemer, *private communications*, 2000.

[Rus86] P. St. J. Russell, *Interference of integrated floquet-bloch waves*, Phys. Rev. A **33** (1986), 3232–3242.

[Sak95] K. Sakoda, *Symmetry, degeneracy and uncoupled modes in two-dimensionsal photonic lattices*, Phys. Rev. B **52** (1995), 7982–7986.

[Sod98] M. Soddemann, *Darstellung, fixierung und untersuchung photonischer eigenschaften an gefärbten und nicht gefärbten kolloidkristallen*, Master's thesis, Fakultät fr Chemie und Pharmazie, Albert-Ludwigs-Universität, Freiburg, 1998.

[Win99] C. Winnewisser, *Elektrooptische detektion von ultrakurzen elektromagnetischen pulsen. anwendungen: Thz-spektroskopie in der zeitdomäne und abbildung von thz-strahlungsprofilen*, Ph.d. thesis, Universtität Freiburg, 1999.

[WLH98] C. Winnewisser, F. Lewen, and H. Helm, *Transmission characteristics of dichroic filters measured by thz time-domin spectroscopy*, Appl. Phys. A **66** (1998), 593–598.

[WLM$^+$97] M. Wanke, O. Lehmann, K. Müller, Q. Wen, and M. Stuke, *Laser rapid prototyping of photonic band-gap microstructures*, Science **275** (1997), 1284–1286.

[WP96] A. J. Ward and J. B. Pendry, *Refraction and geometry in mawell's equations*, J. Mod. Opt. **43** (1996), 773–793.

[XGYL00] Y. Xia, B. Gates, Y. Yin, and Y. Lu, *Monodispersed colloidal spheres: Old materials with new applications*, Adv. Mat. **12** (2000), no. 10, 693–713.

[Yab87] E. Yablonovitch, *Inhibited spontaneous emission in solid-state physics and electronics*, Phys. Rev. Lett. **58** (1987), 2059–2062.

[Yab99] E. Yablonovitch, *Liquid versus photonic crystals*, Nature **401** (1999), 539–541.

[Yeh79] P. Yeh, *Electromagnetic propagation in birefringent layered media*, J. Opt. Soc. Am. **69** (1979), no. 5, 742–755.

[YGL91] E. Yablonovitch, T. J. Gmitter, and K. M. Leung, *Photonic band structure: The face-centered-cubic case employing nonspherical atoms*, Phys. Rev. Lett. **67** (1991), 2295–2298.

[ZS90] Z. Zhang and S. Satpathy, *Electromagnetic wave propagation in periodic structures: Bloch wave solution of maxwell's equations*, Phys. Rev. Lett. **65** (1990), 2650–2653.

Appendix A

3-dimensional Bravais Lattices

This appendix shows real and inverse space configurations of important 3-dimensional Bravais lattices with the specifications of conventional and primitive unit cell, i.e. the 1.BZ. These specifications are crucial for implementing any crystal structure to the computer programs. Therefore they are reproduced from the original Landolt-Brnstein III/13a,c appendix here:

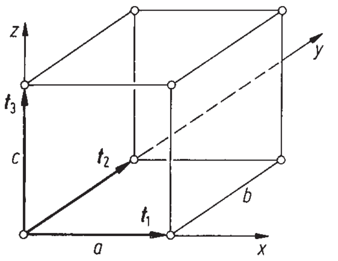

Fig. 33. Conventional (Bravais) unit cell (identical with the primitive unit cell, solid lines) and basis vectors t_i (i=1, 2, 3, bold arrows) of the simple cubic ($a=b=c$) or tetragonal ($a=b\neq c$) lattices. The small circles may represent a basis of more than one atom.

$t_1=(a,\ 0,\ 0)$,
$t_2=(0,\ b,\ 0)$,
$t_3=(0,\ 0,\ c)$.

(Components are given in the Cartesian system x, y, z).

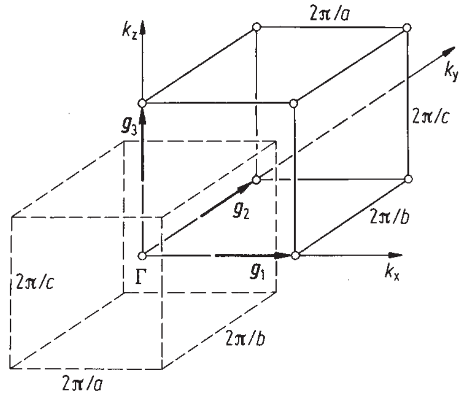

Fig. 34. Reciprocal lattice (full lines), reciprocal basis vectors g_j (j=1, 2, 3, bold arrows) and first Brillouin zone (dashed lines) of the simple cubic ($a=b=c$) and simple tetragonal ($a=b\neq c$) lattices. k_x, k_y, k_z indicate the Cartesian coordinate system in reciprocal space parallel to the x, y, z system in real space (see Fig. 31). The components of any wave vector k or q are referred to this system, including the g_j:

$g_1=(2\pi/a,\ 0,\ 0)$,*)
$g_2=(0,\ 2\pi/b,\ 0)$,
$g_3=(0,\ 0,\ 2\pi/c)$.

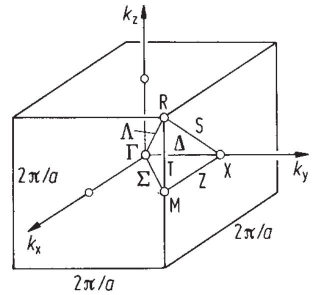

Fig. 35. First Brillouin zone of the simple cubic lattice ($a=b=c$). Symmetry points and symmetry lines are indicated (BSW notation [36Bo]). The following coordinates refer to the Cartesian system k_x, k_y, k_z (see Fig. 32) and are given in units of π/a.

Coordinates of points:
Γ: (000); X: (010); M: (110); R: (111);

along lines:
Δ: [0ζ0] with $0<\zeta<1$; Σ: [ζζ0] with $0<\zeta<1$;
Λ: [ζζζ] with $0<\zeta<1$;

Distances: $\overline{\Gamma X}=\pi/a$; $\overline{\Gamma M}=\sqrt{2}\,\pi/a$; $\overline{\Gamma R}=\sqrt{3}\,\pi/a$.

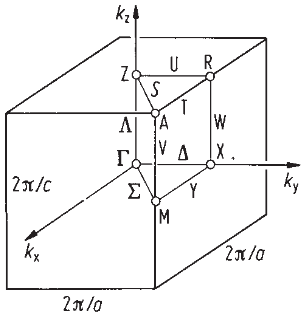

Fig. 36. First Brillouin zone of the simple tetragonal lattice ($a=b\neq c$). Symmetry points and symmetry lines are indicated. The following coordinates refer to the Cartesian system k_x, k_y, k_z (see Fig. 32) and are given in units of π/a, π/a, π/c respectively:

Coordinates of points:
Γ: (000), X: (010); Z: (001); M: (110); R: (011); A: (111).

along lines:
Δ: [0ζ0] with $0<\zeta<1$; Λ: [00ζ] with $0<\zeta<1$;
Σ: [ζζ0] with $0<\zeta<1$;

Distances:
$\overline{\Gamma X}=\pi/a$; $\overline{\Gamma Z}=\pi/c$; $\overline{\Gamma M}=\sqrt{2}\,\pi/a$.

Figure A.1: **simple cubic (sc) and simple tetragonal (st)**

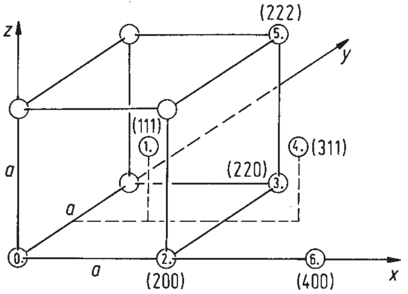

Fig. 1. Structure of the body centred cubic (bcc) metals characterized by lattice parameter a. The size of the atoms (circles) is drawn arbitrarily. A representative position of one of the 8 first, one of the 6 second, one of the 12 third, one of the 24 fourth, one of the 8 fifth, and one of the 6 sixth neighbours of atom "0" are indicated. Their Cartesian coordinates (xyz) in units of $a/2$ are also given.

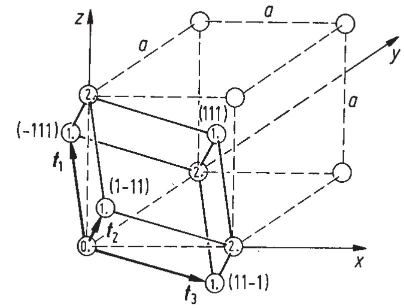

Fig. 2. The primitive unit cell of the bcc lattice (full lines) with its basis vectors $\boldsymbol{t}_i$ (i = 1, 2, 3, bold arrows) is shown relative to the conventional (Bravais) unit cell (dashed lines, see Fig. 1) of the bcc lattice.

$\boldsymbol{t}_1 = (-a/2,\ a/2,\ a/2) = (a/2)(-1,\ 1,\ 1)$,
$\boldsymbol{t}_2 = (a/2,\ -a/2,\ a/2) = (a/2)(1,\ -1,\ 1)$,
$\boldsymbol{t}_3 = (a/2,\ a/2,\ -a/2) = (a/2)(1,\ 1,\ -1)$.

(Components are given in the Cartesian system x, y, z). Volume of the conventional (Bravais) unit cell: $\Omega_B = a^3$. Volume of the primitive unit cell: $\Omega = \Omega_B/2$.

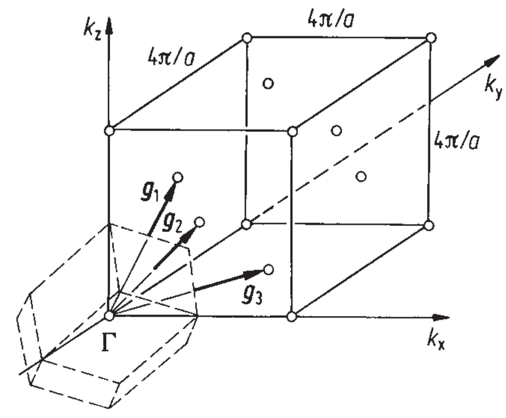

Fig. 3. Reciprocal lattice (fcc, full lines), reciprocal basis vectors $\boldsymbol{g}_j$ (j = 1, 2, 3, bold arrows) and first Brillouin zone (dashed lines) of the bcc lattice. k_x, k_y, k_z indicate the Cartesian coordinate system in reciprocal space parallel to the x, y, z system in real space (see Fig. 2). The components of any wave vector $\boldsymbol{k}$ or $\boldsymbol{q}$ are referred to this system, including the $\boldsymbol{g}_j$:

$\boldsymbol{g}_1 = (0,\ 2\pi/a,\ 2\pi/a) = (2\pi/a)(0,\ 1,\ 1)$,
$\boldsymbol{g}_2 = (2\pi/a,\ 0,\ 2\pi/a) = (2\pi/a)(1,\ 0,\ 1)$,
$\boldsymbol{g}_3 = (2\pi/a,\ 2\pi/a,\ 0) = (2\pi/a)(1,\ 1,\ 0)$,

which are derived from the $\boldsymbol{t}_i$ (see Fig. 2) by*)

$\boldsymbol{g}_j \boldsymbol{t}_i = 2\pi\,\delta_{ji}$, and

$$\boldsymbol{g}_1 = 2\pi\frac{(\boldsymbol{t}_2 \times \boldsymbol{t}_3)}{(\boldsymbol{t}_1 \times \boldsymbol{t}_2)\boldsymbol{t}_3}, \quad \boldsymbol{g}_2 = 2\pi\frac{(\boldsymbol{t}_3 \times \boldsymbol{t}_1)}{(\boldsymbol{t}_2 \times \boldsymbol{t}_3)\boldsymbol{t}_1}, \quad \boldsymbol{g}_3 = 2\pi\frac{(\boldsymbol{t}_1 \times \boldsymbol{t}_2)}{(\boldsymbol{t}_3 \times \boldsymbol{t}_1)\boldsymbol{t}_2}.$$

Volume of the reciprocal fcc unit cell: $\Omega_R = (4\pi/a)^3$.
Volume of the first Brillouin zone: $\Omega_{BZ} = \Omega_R/4$.

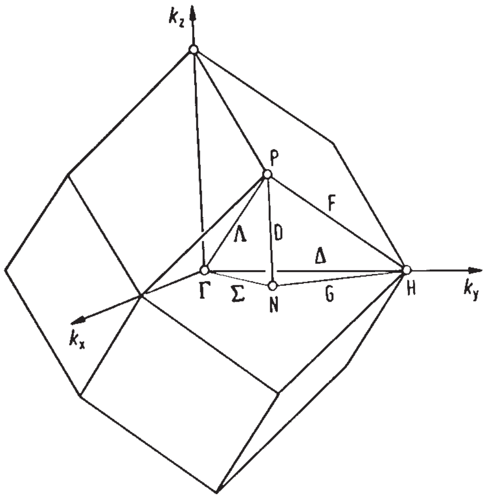

Fig. 4. First Brillouin zone of the bcc lattice. Symmetry points and symmetry lines are indicated (BSW notation [36Bo]). The following coordinates refer to the Cartesian system k_x, k_y, k_z (see Fig. 3) and are given in units of $2\pi/a$.

Coordinates of points:

Γ: (000); H: (010); N: (1/2 1/2 0); P: (1/2 1/2 1/2);

along lines:

Δ: $[0\zeta 0]$ with $0 < \zeta < 1$;	Σ: $[\zeta\zeta 0]$ with $0 < \zeta < 1/2$;
Λ: $[\zeta\zeta\zeta]$ with $0 < \zeta < 1/2$;	F: $[\zeta\zeta\zeta]$ with $1/2 < \zeta < 1$;
G: $[\zeta\zeta 1]$ with $0 < \zeta < 1/2$;	D: $[1/2\ 1/2\ \zeta]$ with $0 < \zeta < 1/2$;

(The coordinates are those in the drawn BZ or in a neighbouring repeated zone, as commonly used in the literature). Distances: $\overline{\Gamma H} = 2\pi/a$; $\overline{\Gamma N} = \sqrt{2}\pi/a$; $\overline{\Gamma P} = \sqrt{3}\pi/a$.

Figure A.2: **body centered cubic (bcc)**

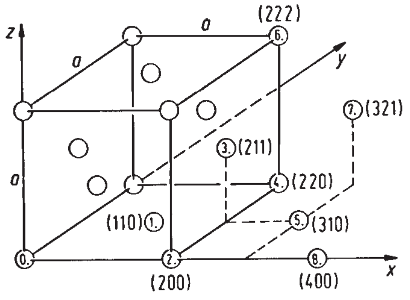

Fig. 5. Structure of the face centred cubic (fcc) metals characterized by lattice parameter a. The size of the atoms (circles) is drawn arbitrarily.

A representative position of one of the 12 first, one of the 6 second, one of the 24 third, one of the 12 fourth, one of the 24 fifth, one of the 8 sixth, one of the 48 seventh, and one of the 6 eighth neighbours of atom "0." are indicated. Their Cartesian coordinates (xyz) in units of $a/2$ are also given.

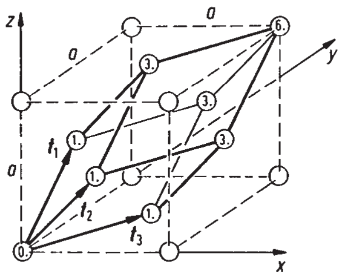

Fig. 6. The primitive unit cell of the fcc lattice (full lines) with its basis vectors t_i (i=1, 2, 3, bold arrows) is shown relative to the conventional (Bravais) unit cell (dashed lines, see Fig. 5) of the fcc lattice.

$t_1=(0,\ a/2,\ a/2)=(a/2)(0,\ 1,\ 1)$,
$t_2=(a/2,\ 0,\ a/2)=(a/2)(1,\ 0,\ 1)$,
$t_3=(a/2,\ a/2,\ 0)=(a/2)(1,\ 1,\ 0)$.

(Components are given in the Cartesian system x, y, z).
Volume of the conventional (Bravais) unit cell: $\Omega_B=a^3$.
Volume of the primitive unit cell: $\Omega=\Omega_B/4$.

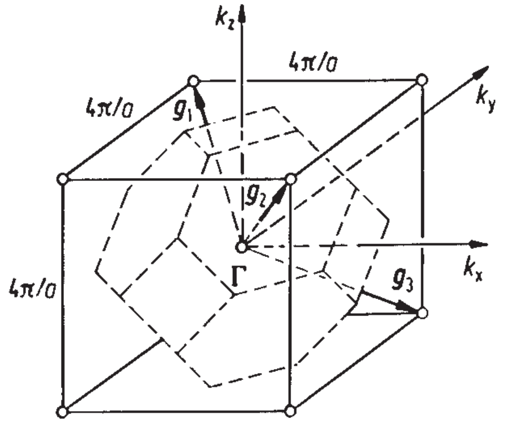

Fig. 8. First Brillouin zone of the fcc lattice. Symmetry points and symmetry lines are indicated (BSW notation [36Bo]). The following coordinates refer to the Cartesian system k_x, k_y, k_z, (see Fig. 7) and are given in units of $2\pi/a$.

Coordinates of points:
Γ: (000); X: (010); L: (1/2; 1/2; 1/2); W: (1/2 1 0)
K: (3/4 3/4 0); U: (1/4 1 1/4);

along lines:
Δ: $[00\zeta]$ with $0<\zeta<1$; Σ: $[\zeta\zeta 0]$ with $0<\zeta<3/4$
for $\Gamma \xrightarrow{\Sigma} K$ and $0<\zeta<1$ for $\Gamma \xrightarrow{\Sigma} K \xrightarrow{S} X'$;
Λ: $[\zeta\zeta\zeta]$ with $0<\zeta<1/2$;

(The coordinates are those in the drawn BZ or in a neighbouring repeated zone, as commonly used in the literature).

Distances: $\overline{\Gamma X}=2\pi/a$; $\overline{\Gamma KX}=\sqrt{2}\,2\pi/a$; $\overline{\Gamma L}=\sqrt{3}\,\pi/a$;

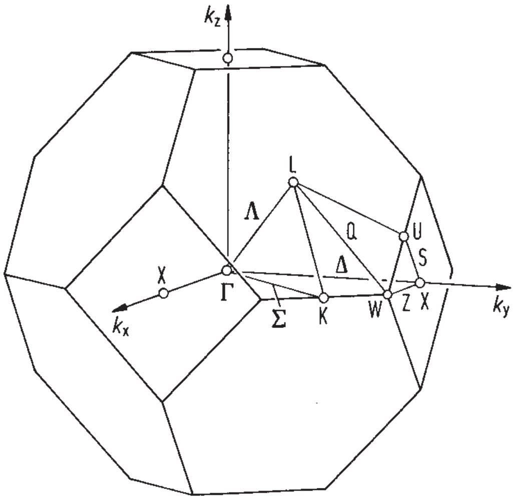

Fig. 7. Reciprocal lattice (bcc, full lines), reciprocal basis vectors g_j (j=1, 2, 3, bold arrows) and first Brillouin zone (dashed lines) of the fcc lattice. k_x, k_y, k_z indicate the Cartesian coordinate system in reciprocal space parallel to the x, y, z system in real space (see Fig. 6). The components of any wave vector k or q are referred to this system, including the g_j:

$g_1=(-2\pi/a,\ 2\pi/a,\ 2\pi/a)=(2\pi/a)(-1,\ 1,\ 1)$,*)
$g_2=(2\pi/a,\ -2\pi/a,\ 2\pi/a)=(2\pi/a)(1,\ -1,\ 1)$,
$g_3=(2\pi/a,\ 2\pi/a,\ -2\pi/a)=(2\pi/a)(1,\ 1,\ -1)$.

Volume of the reciprocal bcc unit cell: $\Omega_R=(4\pi/a)^3$.
Volume of the first Brillouin zone: $\Omega_{BZ}=\Omega_R/2$.

Figure A.3: **face centered cubic (fcc)**

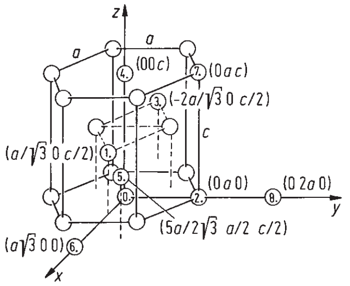

Fig. 9. Structure of the hexagonal close packed (hcp) metals characterized by lattice parameters a and c*). The size of the atoms (circles) is drawn arbitrarily. Representative positions of the first to eighth neighbours of atom "0." are indicated (the order of succession may change if the ratio of c/a is not ideal). Their Cartesian coordinates (xyz) are also given.

---

*) (The ideal ratio of $c/a = 1.633$).

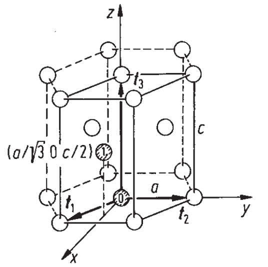

Fig. 10. The primitive unit cell of the hexagonal lattice (full lines) with its basis vectors t_i (i = 1, 2, 3, bold arrows) relative to the conventional (Bravais) unit cell (dashed with full lines). The basis consists of two atoms (hatched circles): one "0." at (000) and a second one "1." at $((a/\sqrt{3})\ 0\ c/2)$ (see Fig. 9).

$t_1 = (\sqrt{3}\,a/2,\ -a/2,\ 0)$,
$t_2 = (0,\ a,\ 0)$,
$t_3 = (0,\ 0,\ c)$.

(Components are given in the Cartesian system x, y, z).
Volume of the conventional (Bravais) unit cell:
$\Omega_B = (3/2)\sqrt{3}\,a^2 c$.
Volume of the primitive unit cell: $\Omega = \Omega_B/3$.

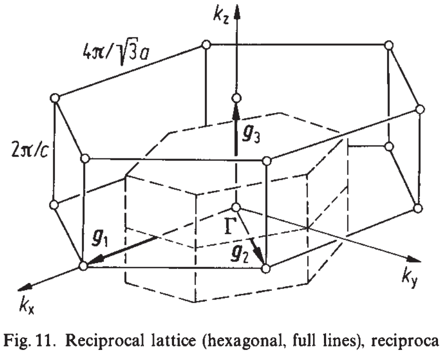

Fig. 11. Reciprocal lattice (hexagonal, full lines), reciprocal basis vectors g_j (j = 1, 2, 3, bold arrows) and first Brillouin zone (dashed lines) of the hcp lattice. k_x, k_y, k_z indicate the Cartesian coordinate system in reciprocal space parallel to the x, y, z system in real space (see Fig. 10). The following components of the g_j are referred to this system:

$g_1 = (4\pi/\sqrt{3}\,a,\ 0,\ 0)$,*)
$g_2 = (2\pi/\sqrt{3}\,a,\ 2\pi/a,\ 0)$,
$g_3 = (0,\ 0,\ 2\pi/c)$.

Volume of the reciprocal hexagonal unit cell:
$\Omega_R = (6/\sqrt{3})(2\pi)^3/a^2 c$.
Volume of the first Brillouin zone: $\Omega_{BZ} = \Omega_R/3$.

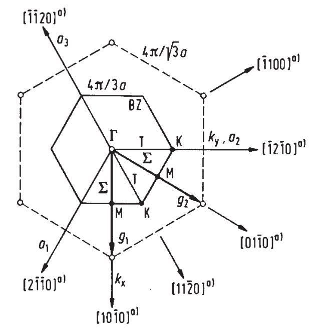

Fig. 12A. Alternative coordinate systems are used in the literature to describe the (reciprocal) hexagonal lattice.

1. The coordinate system referring to the primitive basis vectors g_j (j = 1, 2, 3) (as used in this volume, see Figs. 11, 12): two axes g_1 and g_2 in the hexagonal plane with an angle of 60° between them, the g_3 axis normal to the hexagonal plane.

2. The Cartesian coordinate system: The orthogonal k_x and k_y axes in the hexagonal plane, the k_z axis normal to the hexagonal plane.

3. The four component hexagonal system (Bravais-Miller): three axes a_1, a_2, a_3 in the hexagonal plane with angles of 120° between them, the a_4-axis normal to the hexagonal plane. Directions are described by the appropriate four Bravais-Miller indices $[uvtw]$. Some special directions are indicated in the figure ($\equiv u\,a_1 + v\,a_2 + t\,a_3 + w\,a_4$, with $u + v + t = 0$).

The relative positions of these coordinate systems are shown, and some symmetry points and symmetry directions are indicated:

e.g. directions:
$\Sigma \triangleq [10\bar{1}0]^{a)}$ or $[01\bar{1}0]^{a)}$ etc., $\triangleq [\zeta 00]^{g)}$
$T \triangleq [2\bar{1}\bar{1}0]^{a)}$ or $[11\bar{2}0]^{a)}$ or $[\bar{1}2\bar{1}0]^{a)}$ etc., $\triangleq [\zeta\zeta 0]^{g)}$
$\Delta \triangleq [0001]^{a)} \triangleq [00\zeta]^{g)}$

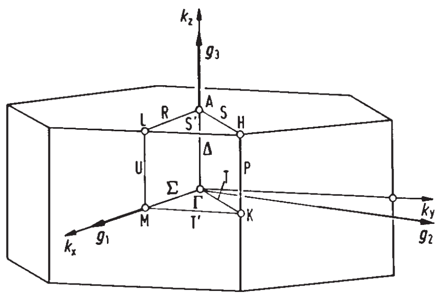

Fig. 12. First Brillouin zone of the hexagonal lattice. The basis vectors g_j of the reciprocal lattice, and symmetry points and symmetry lines are indicated. k_x, k_y, k_z indicate the Cartesian coordinate system. The components of any wave vector $\boldsymbol{k}$ or $\boldsymbol{q}$ and the coordinates of symmetry points and along symmetry lines are referred to the hexagonal coordinate system g_1, g_2, g_3 (see Fig. 11) and are given in units of $4\pi/a\sqrt{3}$, $4\pi/a\sqrt{3}$, $2\pi/c$ respectively:

Coordinates of points:
Γ: (0 0 0); A: (0 0 1/2); M: (1/2 0 0); K: (1/3 1/3 0)
H: (1/3 1/3 1/2); L: (1/2 0 1/2);

along lines:
Σ: $[\zeta 00]$ with $0<\zeta<1/2$; T: $[\zeta\zeta 0]$ with $0<\zeta<1/3$
for $\Gamma \xrightarrow{T} K$ and $0<\zeta<1/2$ for $\Gamma \xrightarrow{T} K \xrightarrow{T'} M$
Δ: $[00\zeta]$ with $0<\zeta<1/2$;
U: $[1/2\ 0\ \zeta]$; P: $[1/3\ 1/3\ \zeta]$; R: $[\zeta\ 0\ 1/2]$ with $0<\zeta<1/2$
S: $[\zeta\ \zeta\ 1/2]$; with $0<\zeta<1/3$
S': $[\zeta\ \zeta\ 1/2]$, T': $[\zeta\zeta 0]$ with $1/3<\zeta<1/2$

(The coordinates are those in the drawn BZ or in a neighbouring repeated zone, as commonly used in the literature).
Distances: $\overline{\Gamma M} = 2\pi/a\sqrt{3}$; $\overline{\Gamma K} = 4\pi/3a$; $\overline{\Gamma A} = \pi/c$.

Figure A.4: **hexagonal close packed (hcp)**

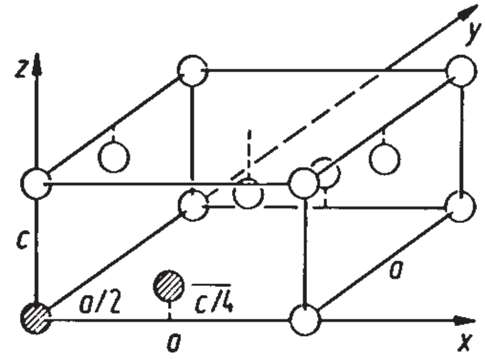

Fig. 13. The structure of white (*β*-)Sn is described by a body centred tetragonal (bct) lattice, with a basis of two atoms, one at (000) and a second one at ($a/2$ 0 $c/4$) (hatched circles). The conventional (Bravais) unit cell characterized by the lattice parameters a and c is drawn with $c/a \approx 1/2$ and contains two such pairs [67Pr, 67Ro].

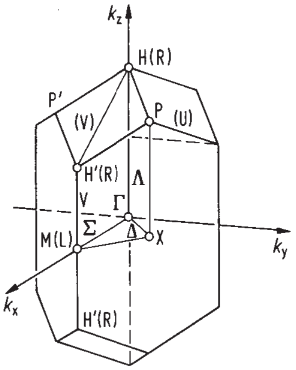

Fig. 16. First Brillouin zone of the body centred tetragonal lattice ($c<a$). Symmetry points and symmetry lines are indicated [67Pr, 67Ro]. (Labels in paranthesis are also used). The following coordinates refer to the Cartesian system k_x, k_y, k_z (see Fig. 15) and are given in units of $2\pi/a$, $2\pi/a$, $2\pi/c$, respectively.

Coordinates of points:

Γ: (000), M: (100), X: (1/2 1/2 0), H: $(0\,0((a^2+c^2)/2a^2))$
H′: $(1\,0((a^2-c^2)/2a^2))$;

along lines:

Σ: [ζ00] with $0<\zeta<1$; Δ: [$\zeta\zeta$0] with $0<\zeta<1/2$
Λ: [00ζ] with $0<\zeta<0.65$ for $\Gamma \xrightarrow{\Lambda} \mathrm{H}$ and Λ, V: [00ζ]
with $0<\zeta<1$ for $\Gamma \xrightarrow{\Lambda} \mathrm{H} \xrightarrow{\mathrm{V}} \mathrm{M}$

(The coordinates are those in the drawn BZ or in a neighbouring repeated zone, as commonly used in the literature).

Distances:

$\overline{\Gamma \mathrm{H}} = (2\pi/c)((a^2+c^2)/2a^2) \approx 0.65\, 2\pi/c$; $\overline{\Gamma \mathrm{M}} = 2\pi/a$;
$\overline{\Gamma \mathrm{X}} = \sqrt{2}\pi/a$; $\overline{\mathrm{MH}'} = (2\pi/c)((a^2-c^2)/2a^2)$

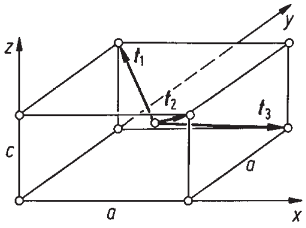

Fig. 14. Conventional body centred tetragonal (Bravais) unit cell of the Sn lattice and basis vectors $\boldsymbol{t}_i$ (i = 1, 2, 3, bold arrows) of the primitive unit cell drawn from the centre of the cell (full lines). Each small circle represents a basis pair of two atoms (see Fig. 13).

$\boldsymbol{t}_1 = (-a/2,\ a/2,\ c/2)$,
$\boldsymbol{t}_2 = (a/2,\ -a/2,\ c/2)$,
$\boldsymbol{t}_3 = (a/2,\ a/2,\ -c/2)$.

(Components are given in the Cartesian system x, y, z).
Volume of the conventional (Bravais) unit cell: $\Omega_B = a^2 c$.
Volume of the primitive unit cell (containing two atoms): $\Omega = \Omega_B/2$.

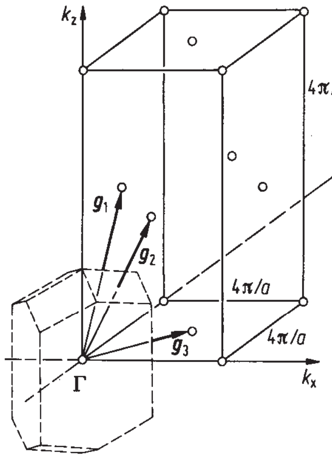

Fig. 15. Reciprocal lattice (fct, full lines), reciprocal basis vectors $\boldsymbol{g}_j$ (j = 1, 2, 3, bold arrows) and first Brillouin zone (dashed lines) of the bct lattice. k_x, k_y, k_z indicate the Cartesian coordinate system in reciprocal space parallel to the x, y, z system in real space (see Fig. 14). The components of any wave vector $\boldsymbol{k}$ or $\boldsymbol{q}$ are referred to this system, including the $\boldsymbol{g}_j$:

$\boldsymbol{g}_1 = (0,\ 2\pi/a,\ 2\pi/c)$,*)
$\boldsymbol{g}_2 = (2\pi/a,\ 0,\ 2\pi/c)$,
$\boldsymbol{g}_3 = (2\pi a,\ 2\pi/a,\ 0)$.

Volume of the reciprocal fct unit cell: $\Omega_R = (4\pi)^3/a^2 c$.
Volume of the first Brillouin zone: $\Omega_{BZ} = \Omega_R/4$.

Figure A.5: **body centered tetragonal (bct)**

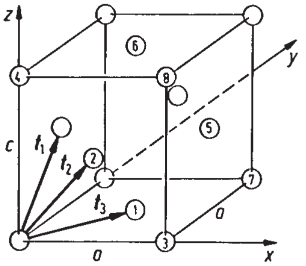

Fig. 17. Conventional (Bravais) unit cell of the face centred tetragonal (fct) lattice (solid lines) and basis vectors $\boldsymbol{t}_i$ ($i=1,2,3$, bold arrows) of the primitive unit cell. Lattice parameters a and c are drawn with $c/a \approx 1.08$. This lattice is very similar to the fcc lattice but the next neighbours are different, due to the fact that $a<c$. The Cartesian coordinates (x y z) in units of ($a/2$ $a/2$ $c/2$) of representative positions of the first to tenth neighbours are: 1. (110), 2. (101), 3. (200), 4. (002), 5. (211), 6. (112), 7. (220), 8. (202), 9. (310), 10. (103), (some of them are indicated).

Components of the basis vectors $\boldsymbol{t}_i$ are given in the same system:

$\boldsymbol{t}_1=(0,\ a/2,\ c/2)$,
$\boldsymbol{t}_2=(a/2,\ 0,\ c/2)$,
$\boldsymbol{t}_3=(a/2,\ a/2,\ 0)$.

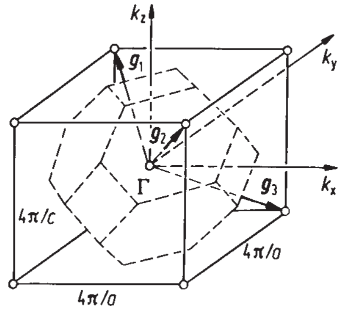

Fig. 18. Reciprocal lattice (nearly bcc, full lines), basis vectors $\boldsymbol{g}_j$ ($j=1,2,3$, bold arrows) and first Brillouin zone (dashed lines) of the face centred tetragonal lattice. k_x, k_y, k_z indicate the Cartesian coordinate system in reciprocal space, parallel to the x, y, z system in real space (see Fig. 17). The components of any wave vector $\boldsymbol{k}$ or $\boldsymbol{q}$ are referred to this system, including the $\boldsymbol{g}_j$:

$\boldsymbol{g}_1=(-2\pi/a,\ 2\pi/a,\ 2\pi/c)$,*)
$\boldsymbol{g}_2=(2\pi/a,\ -2\pi/a,\ 2\pi/c)$,
$\boldsymbol{g}_3=(2\pi/a,\ 2\pi/a,\ -2\pi/c)$.

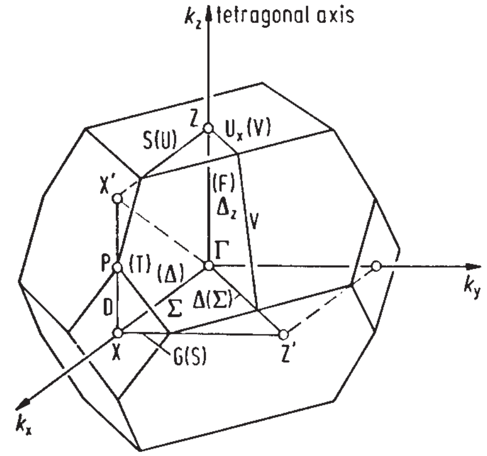

Fig. 19. First Brillouin zone of the face centred tetragonal lattice*). Symmetry points and symmetry lines are indicated [69Sm, 68Lu] (labels in paranthesis are also used).

The following coordinates refer to the Cartesian system k_x, k_y, k_z (see Fig. 18) and are given in units of $2\pi/a$, $2\pi/a$, $2\pi/c$ respectively.

Coordinates of points:
Γ: (000); X: (100); Z: (001); P: (1 0 1/2);

along lines:
Σ: [ζ00] with $0<\zeta<1$; Δ: [ζζ0] with $0<\zeta<1$;
Δ_z: [00ζ] with $0<\zeta<1$; D: [10ζ] with $0<\zeta<1/2$;

(The coordinates are those in the drawn BZ or in a neighbouring repeated zone, as commonly used in the literature).

Distances:
$\overline{\Gamma Z}=2\pi/c$; $\overline{\Gamma X}=2\pi/a$; $\overline{XP}=\pi/c$; $\overline{\Gamma Z'}=\sqrt{2}\,2\pi/a$
lengths of: $\overline{G}=(\pi/a)(a^2/c^2)$; $\overline{S}=2\pi/a\,(1-a^2/2c^2)$;

Figure A.6: **face centered tetragonal (bct)**

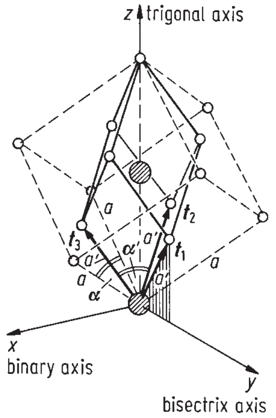

Fig. 20. The rhombohedral structure of As, Sb and Bi can be described by cubic lattices with slight displacements of the atoms.

The conventional (Bravais) unit cell is a slightly distorted face centred cube (dashed lines, note: $\alpha=87°\,34'$ for Bi, instead of $\alpha=90°$ for fcc) with a basis of two atoms: one at (000) and the second one near the centre of the cube, slightly displaced parallel to the trigonal axis (hatched circles). Each small circle represents another basis pair of such two atoms. This cell is characterized by the lattice parameters a and α.

The rhombohedral primitive unit cell (full lines) is that of the slightly distorted face centred cube just described, with the same two basis atoms (hatched circles). The basis vectors $\boldsymbol{t}_i$ (i=1, 2, 3, bold arrows) are characterized by the lattice parameters a' and α' (length of and angle between the $\boldsymbol{t}_i$, note: $\alpha'=57°\,16'$ for Bi instead of $\alpha'=60°$ for fcc).

The binary, bisectrix and trigonal axes are used as the Cartesian coordinate system x, y, z [68Br].

$\boldsymbol{t}_1=(0,\ a'\sin\theta,\ a'\cos\theta)$,
$\boldsymbol{t}_2=((-1/2)\sqrt{3}\,a'\sin\theta,\ (-1/2)\,a'\sin\theta,\ a'\cos\theta)$,
$\boldsymbol{t}_3=((1/2)\sqrt{3}\,a'\sin\theta,\ -(1/2)\,a'\sin\theta,\ a'\cos\theta)$.

(Components are given in the Cartesian system x, y, z, θ is the angle between the $\boldsymbol{t}_i$ and the z-axis: $\cos\theta=(1/\sqrt{3})\cdot\sqrt{1+2\cos\alpha'}$).

Sometimes this structure is described by separating a simple cubic lattice (not shown in the figure) into two face centred sublattices performing a slight trigonal distortion (further information, see [55Er, 71Cr, 60Jo].

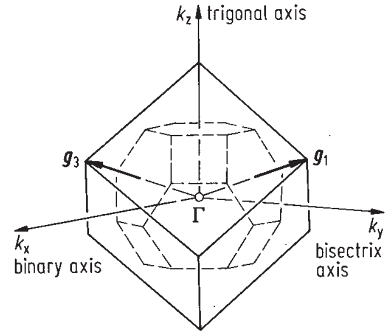

Fig. 21. Reciprocal lattice (rhombohedral, nearly bcc, full lines), basis vectors $\boldsymbol{g}_j$ (j=1, 2, 3, bold arrows, $\boldsymbol{g}_2$ is not drawn for clarity of the figure) and the first Brillouin zone (dashed lines) of the nearly fcc lattice of As, Bi, Sb. The binary, bisectrix and trigonal axes are used as the Cartesian coordinate system k_x, k_y, k_z parallel to the x, y, z system in real space:

$\boldsymbol{g}_1=(0,\ g\sin\varphi,\ g\cos\varphi)$,
$\boldsymbol{g}_2=((-1/2)\sqrt{3}\,g\sin\varphi,\ -(1/2)\,g\sin\varphi,\ g\cos\varphi)$,
$\boldsymbol{g}_3=((1/2)\sqrt{3}\,g\sin\varphi,\ -(1/2)\,g\sin\varphi,\ g\cos\varphi)$.

(g is the length of the $\boldsymbol{g}_j$ and φ is the angle between them and the k_z-axis: $\cot\varphi=(1/2)\tan\theta$, $g=(2\pi/a'\cos(\theta-\varphi))$).*).

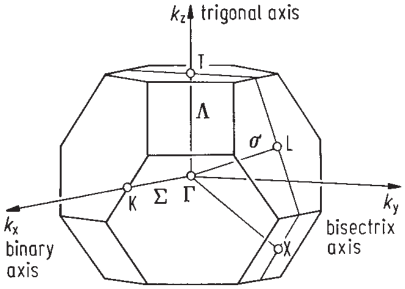

Fig. 22. First Brillouin zone of the rhombohedral lattice. Symmetry points and symmetry lines are indicated. (σ denotes the vertical plane containing the trigonal and bisectrix axes).

Because of the deformation of the cubic lattice, the coordinates of symmetry points and along symmetry lines are not given here as function of the lattice parameters a, α or a', α' respectively. The lengths of wave vectors $\boldsymbol{k}$ or $\boldsymbol{q}$ along symmetry lines from the centre Γ are simply described by the ratio of reduced wave vectors $\zeta=k/k_{\max}$ or $\zeta=q/q_{\max}$. Some examples are given:

along Σ: $k_{\max}=\overline{\Gamma KX}\gtrapprox 2\pi\sqrt{2}/a,{}^{1}$)
along $\Gamma\xrightarrow{\sigma}X$: $k_{\max}=\overline{\Gamma X}=(g/\sqrt{2})/\sqrt{(1+\cos\alpha')}\gtrapprox 2\pi/a,{}^{1}$)
along $\Gamma\xrightarrow{\sigma}L$: $k_{\max}=\overline{\Gamma L}=g/2\gtrapprox\pi\sqrt{3}/a,{}^{1}$)
along Λ: $k_{\max}=\overline{\Gamma T}=(\sqrt{3}\,g/2)\sqrt{(1-\cos\alpha')/(1+\cos\alpha')}$ $\lessapprox\pi\sqrt{3}/a^{1}$).

Figure A.7: **rhombohedral**

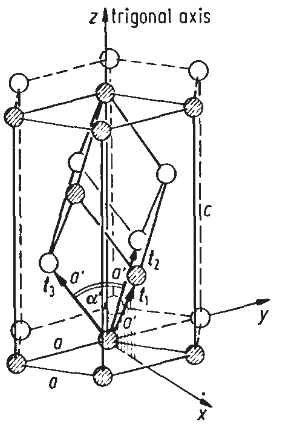

Fig. 23. The rhombohedral structure of Hg can be described by a distorted face centred cubic lattice (the face centred cube is not shown explicitely for clarity of the figure, so compare the rhombohedron (heavy lines) with Fig. 6). The conventional (Bravais) unit cell is a triatomic hexagonal cell (hatched circles and light lines), characterized by the lattice parameters a and c; The primitive unit cell is the rhombohedron (heavy lines) of the distorted face centred cube mentioned above. The basis vectors $\boldsymbol{t}_i$ (i = 1, 2, 3, bold arrows) are characterized by the lattice parameters a' and α' (length of and angle between the $\boldsymbol{t}_i$; note: $\alpha' = 70°32'$ instead of $\alpha' = 60°$ for fcc).

$\boldsymbol{t}_1 = (a' \sin\theta,\ 0,\ a'\cos\theta)$,
$\boldsymbol{t}_2 = (-(1/2)\,a'\sin\theta,\ (1/2)\sqrt{3}\,a'\sin\theta,\ a'\cos\theta)$,
$\boldsymbol{t}_3 = (-(1/2)\,a'\sin\theta,\ -(1/2)\sqrt{3}\,a'\sin\theta,\ a'\cos\theta)$.

(Components are given in the Cartesian system x, y, z; θ is the angle between the $\boldsymbol{t}_i$ and the z-axis with $\cos\theta = (1/\sqrt{3}) \cdot \sqrt{(1+2\cos\alpha')}$).

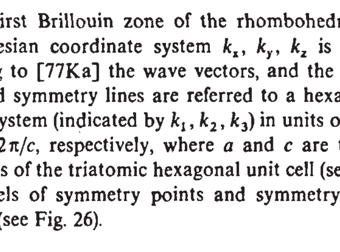

Fig. 25. First Brillouin zone of the rhombohedral lattice. The Cartesian coordinate system k_x, k_y, k_z is indicated. According to [77Ka] the wave vectors, and the symmetry points and symmetry lines are referred to a hexagonal coordinate system (indicated by k_1, k_2, k_3) in units of $4\pi/\sqrt{3}\,a$, $4\pi/\sqrt{3}\,a$, $2\pi/c$, respectively, where a and c are the lattice parameters of the triatomic hexagonal unit cell (see Fig. 23). Some labels of symmetry points and symmetry lines are indicated (see Fig. 26).

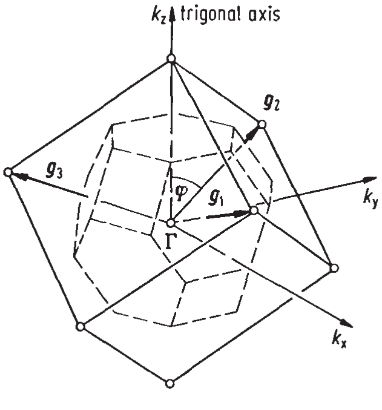

Fig. 24. Reciprocal (rhombohedral, nearly bcc) unit cell (solid lines), basis vectors $\boldsymbol{g}_j$ (j = 1, 2, 3, bold arrows) and first Brillouin zone (dashed lines, rather similar to that one of a fcc lattice, but stretched parallel to the trigonal axis k_z) of the rhombohedral lattice. k_x, k_y, k_z indicate a Cartesian coordinate system in reciprocal space parallel to the x, y, z system in real space (see Fig. 23).

$\boldsymbol{g}_1 = (g\sin\varphi,\ 0,\ g\cos\varphi)$,*)
$\boldsymbol{g}_2 = (-(1/2)\,g\sin\varphi,\ (1/2)\sqrt{3}\,g\sin\varphi,\ g\cos\varphi)$,
$\boldsymbol{g}_3 = (-(1/2)\,g\sin\varphi,\ -(1/2)\sqrt{3}\,g\sin\varphi,\ g\cos\varphi)$.

(Components are given in the Cartesian system k_x, k_y, k_z. g is the length of the $\boldsymbol{g}_j$ and φ is the angle between them and the k_z axis: $\cot\varphi = (1/2)\tan\theta$, $g = 2\pi/(a'\cos(\theta-\varphi))$).*)

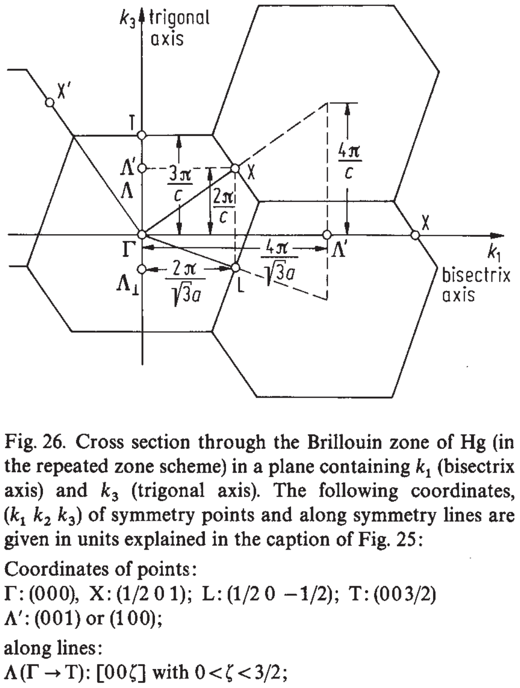

Fig. 26. Cross section through the Brillouin zone of Hg (in the repeated zone scheme) in a plane containing k_1 (bisectrix axis) and k_3 (trigonal axis). The following coordinates, (k_1 k_2 k_3) of symmetry points and along symmetry lines are given in units explained in the caption of Fig. 25:

Coordinates of points:
Γ: (000), X: (1/2 0 1); L: (1/2 0 −1/2); T: (0 0 3/2)
Λ': (001) or (100);

along lines:
$\Lambda(\Gamma \to T)$: $[00\zeta]$ with $0<\zeta<3/2$;
$\Gamma \to X$: $[\zeta 0 2\zeta]$ with $0<\zeta<1/2$;
$\Gamma \to L$: $[\zeta 0 -\zeta]$ with $0<\zeta<1/2$;
$\Gamma \to \Lambda' \to X$: $[\zeta 00]$ with $0<\zeta<3/2$;
$\Gamma \to X'$: $[-\zeta 0 4\zeta]$ with $0<\zeta<1/2$;

Distances (within the first zone):
$\overline{\Gamma L} = (\pi/ac)\sqrt{(3a^2+4c^2)/3}$; $\overline{\Gamma T} = 3\pi/c$
$\overline{\Gamma X} = (2\pi/ac)\sqrt{(3a^2+c^2)/3}$;

(For simplicity the zone scheme is drawn for the ideal fcc lattice).

Figure A.8: **rhombohedral**

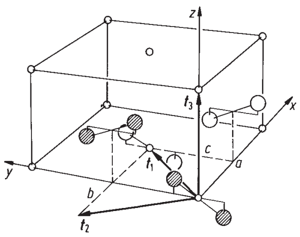

Fig. 27. The structure of Ga can be described by a base centred orthorhombic lattice with a basis of four atoms. The conventional (Bravais) unit cell is shown with full lines and the basis atoms are characterized by hatched circles. Small circles are the lattice points generated by the basic translations $\boldsymbol{t}_i$ (i=1, 2, 3, bold arrows), each of them representing the four basis atoms (not all drawn for clarity of the figure). In the Cartesian system x, y, z the components of the basis vectors $\boldsymbol{t}_i$ are given by:

$\boldsymbol{t}_1=(a/2,\ b/2,\ 0)$,
$\boldsymbol{t}_2=(-a/2,\ b/2,\ 0)$,
$\boldsymbol{t}_3=(0,\ 0,\ c)$.

(a, b, c being the orthorhombic lattice parameters: $a \approx c < b$) (This notation is different from that of [62Sl] where the permutation x → y; y → z; z → x is applied) [69Wa].

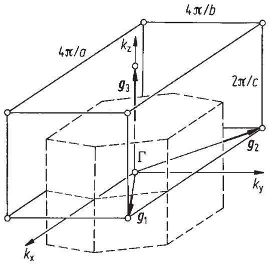

Fig. 28. Reciprocal lattice (base centred orthorhombic, full lines), reciprocal basis vectors $\boldsymbol{g}_j$ (j=1, 2, 3, bold arrows) and first Brillouin zone (dashed lines) of the base centred orthorhombic lattice. k_x, k_y, k_z indicate the Cartesian coordinate system in reciprocal space parallel to the x, y, z system in real space (see Fig. 27). The components of any wave vector $\boldsymbol{k}$ or $\boldsymbol{q}$ are referred to this system, including the $\boldsymbol{g}_j$:

$\boldsymbol{g}_1=(2\pi/a,\ 2\pi/b,\ 0)$,*)
$\boldsymbol{g}_2=(-2\pi/a,\ 2\pi/b,\ 0)$,
$\boldsymbol{g}_3=(0,\ 0,\ 2\pi/c)$.

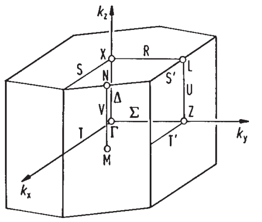

Fig. 29. First Brillouin zone of the base centred orthorhombic lattice (α-Ga, $a \approx c < b$). Symmetry points and symmetry lines are indicated [62Sl, 69Wa]. The following coordinates refer to the Cartesian system k_x, k_y, k_z [see Fig. 28] and are given in units of $2\pi/a$, $2\pi/b$, $2\pi/c$, respectively.

Coordinates of points:
Γ: (000); X: (0 0 1/2); Z: (010); M=(1/2 1/2 0)

along lines:
Σ: [0ζ0] with $0<\zeta<1$; T, T': [ζ00] with $0<\zeta<1$;
Δ: [00ζ] with $0<\zeta<1/2$; S, S': [ζ 0 1/2] with $0<\zeta<1$;

(The coordinates are those in the drawn BZ or in a neighbouring repeated zone, as commonly used in the literature).

Distances:
$\overline{\Gamma Z}=2\pi/b$; $\overline{\Gamma X}=\pi/c$; length of $T=(\pi/a)((a^2+b^2)/b^2)$.

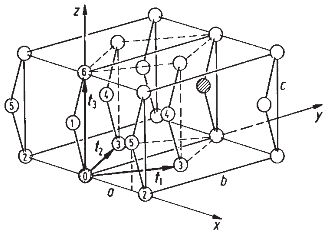

Fig. 30. Base centred orthorhombic structure of α-U. The orthorhombic (Bravais) unit cell is shown with bold lines: the basis consists of two atoms, one at (000) and another one at (0 4b/5 c/2) (hatched circles). The dashed lines outline the primitive unit cell containing the same two atoms. Its basis vectors $\boldsymbol{t}_i$ (i=1, 2, 3, bold arrows) are:

$\boldsymbol{t}_1=(a/2,\ b/2,\ 0)$,
$\boldsymbol{t}_2=(-a/2,\ b/2,\ 0)$,
$\boldsymbol{t}_3=(0,\ 0,\ c)$.

(Components are referred to the Cartesian system x, y, z. a, b, c are the orthorhombic lattic parameters: $a<c<b$). Some of the positions of the first to sixth neighbours of the "0"-atom are indicated [79Cr].

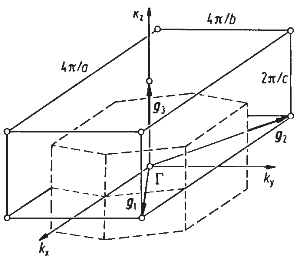

Fig. 31. Reciprocal lattice (base centred orthorhombic, full lines), reciprocal basis vectors $\boldsymbol{g}_j$ (j=1, 2, 3, bold arrows) and first Brillouin zone (dashed lines) of the base centred orthorhombic lattice. k_x, k_y, k_z indicate the Cartesian coordinate system in reciprocal space parallel to the x, y, z system in real space (see Fig. 30). The components of any wave vector $\boldsymbol{k}$ or $\boldsymbol{q}$ are referred to this system, including the $\boldsymbol{g}_j$:

$\boldsymbol{g}_1=(2\pi/a,\ 2\pi/b,\ 0)$,*)
$\boldsymbol{g}_2=(-2\pi/a,\ 2\pi/b,\ 0)$,
$\boldsymbol{g}_3=(0,\ 0,\ 2\pi/c)$.

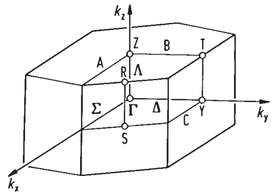

Fig. 32. First Brillouin zone of the base centred orthorhombic lattice (α-U, $a<c<b$). Symmetry points and symmetry lines are indicated [79Cr]. The following coordinates refer to the Cartesian system k_x, k_y, k_z [see Fig. 31] and are given in units of $2\pi/a$, $2\pi/b$, $2\pi/c$, respectively.

Coordinates of points:
Γ=(000); Y=(010) and (100); Z=(0 0 1/2);
S=(1/2 1/2 0);

along lines:
Δ=[0ζ0] with $0<\zeta<1$; Σ, C: [ζ00] with $0<\zeta<1$
(for $\Gamma \xrightarrow{\Sigma, C} Y$); Λ: [00ζ] with $0<\zeta<1/2$.

(The coordinates are those of the drawn BZ or in a neighbouring repeated zone, as commonly used in the literature).

Distances:
$\overline{\Gamma Y}=2\pi/b$; $\overline{\Gamma Z}=\pi/c$; $\overline{\Gamma(\Sigma, C)\,Y}=2\pi/a$.
length of $\Sigma=(\pi/a)((a^2+b^2)/b^2)$.

Figure A.9: **base centered orthorhombic**

Appendix B

Sample Main.cc Program

```
/*
 *  File          : main.cc
 *  Created       : Mit  9.Aug. 2000
 *  Author        : Anton OEttl
 *  Short Desc.   : PBG Calculations for 3D Lincoln log
 */
#include <string> #include <vector> #include <list> #include
<algorithm> #include <stdio.h> #include <NL/Exceptions.hh>
#include <NL/Util/PLOG.hh> #include <PBG/Crystal/BCTetragon.hh>
#include <PBG/Shape/WoodPile.hh> #include <PBG/SRDielectric2.hh>
#include <PBG/PW_3D_Real.hh> #include <PBG/BandStructure.hh>
#include <PBG/OutputBands.hh>

using namespace std; using namespace NL::EXCEPTIONS; using
namespace PBG; using namespace PBG::CRYSTAL; using namespace
PBG::SHAPE; using namespace PBG::DIELECTRIC; using namespace
PBG::PLANE_WAVES;

//#define OUTPUT_FIELD
#define OUTPUT_BANDS
//#define OUTPUT_DOS

int main(){
  plog.attach("log_file");

  typedef SRDielectric2<3>                    dielectric_t;
  typedef BandStructure<3,Real,dielectric_t::SYMMETRY>
                                              band_structure_t;
  typedef PW_3D_Real                          plane_waves_t;
  typedef plane_waves_t::kvector_t            kvector_t;
  typedef BCTetragon                          crystal_t;
  typedef crystal_t::position_t               position_t;
```

```
  typedef WoodPile                           shape_t;
  try {

//    Real const thick = 0.1;

    // The Crystal
    crystal_t     crystal(1.0,1.204);

    // Output band structures along the following paths
    vector<char *> path;
    path.push_back("G");path.push_back("K");
    path.push_back("T");path.push_back("H");
    path.push_back("G");path.push_back("O");path.push_back("L");
    path.push_back("K");path.push_back("W");path.push_back("X");
    // Make sure the symmetry points are valid for this crystal
    for(unsigned int i = 0 ; i < path.size()  ; i++){
      crystal.get_symm_point(path[i]);
    }

    // The Shape
    shape_t       shape(1.0,0.301);

    // The dielectric
    Real eb = 1;
    Real e1 = 3.25*3.25;

    dielectric_t  dielectric(&crystal,&shape,eb,e1);

    // Visualization
#if 0
     Real min[3] = {-2,-2,0};
     Real max[3] = {2,2,1.8};
     int const N[3] = {100,100,13};

     char file[12] = "crystal.ptv";
     dielectric.plot_mtv(file,min,max,N);
     //exit(0);
#endif
    // Planewaves
    int n[3] = {2,2,2};
    plane_waves_t pw(crystal,n);
    plog << pw.get_size() << " plane waves\n";
    cerr << pw.get_size() << " plane waves\n";

    int const FFT_M[3]    = {256,256,256};
```

```
    int const FFT_EPCO[3] = {1,1,1};

    // Set up the band structure engine
    band_structure_t band_structure(dielectric,pw,FFT_M,FFT_EPCO);

#ifdef OUTPUT_BANDS
    {
      int const Nk    = 29;
      int const bands = 20;

      OutputBands<band_structure_t> out_bands(band_structure,bands);
      out_bands.output_path(path,Nk);
    }
#endif // #ifdef OUTPUT_BANDS


  }catch(Exception &E){
    cerr << E.what();
  }catch(std::exception &E){
    cerr << E.what();
  }catch(...){
    cerr << "strange exception \n";
  }
};
```

Appendix C

Failed Design of an Optical Diode

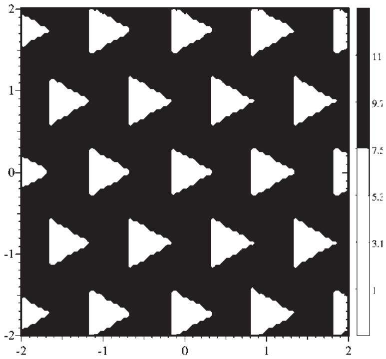

Figure C.1: **Crystal Structure**

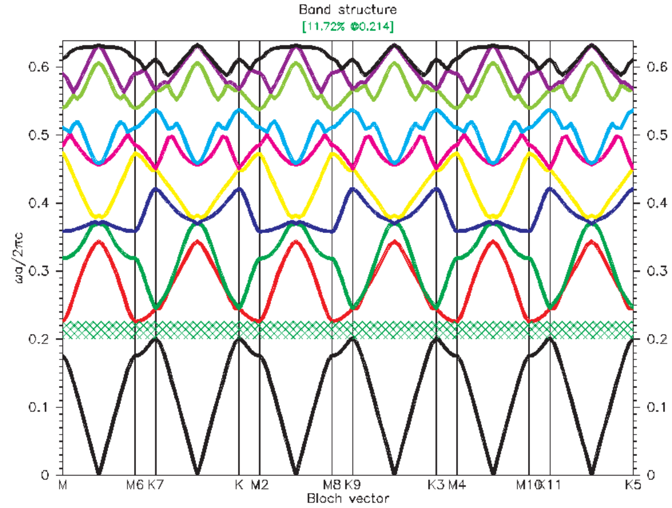

Figure C.2: **Band Structure**

Here are the people without who this work would not have been possible.

- In particular I wish to thank Prof. Hanspeter Helm for his great support throughout my thesis. It has been a pleasure working in his group.
- I am very grateful to Prof. Sajeev John and Ovidiu Toader for introducing me to the field of photonic crystals and having patience with in the beginning.
- Prof. Jürgen Schneider I want to thank for offering me a 'Hiwi' position and for granting me to work with his computer. Thanks to Carsten Winnewisser for establishing the connections I was later profiting from.
- Peter Uhd Jepsen and the THz-crew with Markus Walther, Bernd Fischer and Michael Schall I thank for always being extremely helpful regarding the experiments. Special thanks go out to Peter Uhd Jepsen for his great effort finishing our proposal (in vein) for the DFG-Schwerpunkt and highly interesting discussions.
- I would like to thank Prof. Walter Richtering and Matthias Soddemann for the good and fruitful collaboration.
- Invaluable support on the computers and operating systems I received by Dipl. Ing. Ulrich Person. Thank you very much !
- Thanks also to the technical staff: Achim Holzer, Isabella Siegel, Eric Meisl and the secretary Marion Furtwängler-Fritz.
- Thanks to Jessica Mondia, Steve Leonard and Hong Wee Tan at the U of T.
- Special thanks to all my fellow students for their help and support throughout those years at the university and for having a great time with them !

... and of course the most special thanks go out to **my parents !!**

Hiermit versichere ich, daß ich die vorliegende Arbeit selbständig, und ausschließlich unter Verwendung der angegebenen Quellen und Hilfsmittel, verfaßt habe.

Freiburg im Breisgau, 2. März 2001

Anton W. Öttl